



Universität Hamburg

DER FORSCHUNG | DER LEHRE | DER BILDUNG

Dissertation

Zur Erlangung des Doktorgrades an der Facultät für Mathematik,
Informatik un Naturwissenschaften
im Fachbereich Physik

Self-assembly of gold nanoparticles into supercrystals, hybrid systems, and binary superstructures

vorgelegt von

Juan Jesús Barrios Capuchino

Hamburg

December 2024

This work was conducted between January 2021 and December 2024 in the group of Prof. Dr. Wolfgang Parak at the Center for Hybrid Nanostructures, Department of Physics, Faculty of Mathematics, Informatics and Natural Sciences, University of Hamburg, Germany

Gutachter der Dissertation:
(Supervisor)

Prof. Dr. Wolfgang J. Parak
Dr. Florian Schulz

Zusammensetzung der Prüfungskommission:
(Examination Board)

Prof. Dr. Wolfgang J. Parak
Dr. Florian Schulz
Prof. Dr. Patrick Huber
Prof. Dr. Nils Huse
Prof. Dr. Daniela Pfannkuche

Vorsitzende/r der Prüfungskommission:
(Head of Examination Board)

Datum der Disputation:
(Date of Disputation)

10.02.2025

Vorsitzender Fach-Promotionsausschuss PHYSIK:
(Chairman of the Doctoral Committee Physics)

Prof. Dr. Markus Drescher

Leiter des Fachbereichs:
(Chairman of the Faculty Physics)

Prof. Dr. Markus Drescher

Dekan der MIN Fakultät:
(Dean of the MIN-Faculty)

Prof. Dr.-Ing Norbert Ritter

This dissertation has been approved by:

Supervisor: Prof. Dr. Wolfgang Parak

Contents

Abstract	I
Zusammenfassung	III
List of Publications	V
List of Figures	VII
List of Tables	XI
List of Schemes	XII
List of Abbreviations	XIII
1 Introduction	1
1.1 Nanoscience and Nanotechnology	1
1.2 Nanofabrication	2
1.3 Gold Nanoparticles	3
1.4 Surface Plasmon Resonance (SPR)	4
1.5 Synthesis of gold nanoparticles	5
1.5.1 Turkevich method	5
1.5.2 Seed-mediated growth method	6
1.6 Surface stabilization of nanoparticles	7
1.7 Self-assembly of nanoparticles	8
1.7.1 Evaporation-induced self-assembly	9
1.7.2 Air-liquid interfacial self-assembly	10
1.7.3 Interactions involved in the self-assembly of NPs	11
1.7.4 Applications of self-assembled supercrystals	12
1.8 Outline of this Thesis	14
1.9 Thesis Overview	14
2 Self-assembly of Au NPs into long-range supercrystals	17
2.1 Introduction	17
2.1.1 Self-assembly of 2D and 3D plasmonic supercrystals	17
2.1.2 Importance of homogeneous self-assembly	18
2.1.3 Applications of Au NP supercrystals	18
2.2 Methods	20

2.3	<i>Results and Discussion</i>	25
2.3.1	Optimization parameters for the synthesis of high-quality and high concentration of Au NPs.....	25
2.3.2	Surface Functionalization of Au NPs	26
2.3.3	Self-assembly of long-range Au NP supercrystals	29
2.4	<i>Growth Modes of Au NP supercrystals</i>	33
2.5	<i>Phase transition in 3D supercrystals</i>	39
2.6	<i>Conclusion</i>	43
3	Incorporation of highly ordered PSSH-functionalized Au NPs into 2D and 3D arrays within and on the pores of porous silicon membranes.....	44
3.1	<i>Introduction</i>	44
3.1.1	Porous Silicon.....	44
3.1.2	Porous silicon as a host material.....	46
3.1.3	Surface-enhanced Raman spectroscopy (SERS)	46
3.1.4	Plasmonic gold nanoparticles	47
3.2	<i>Methods</i>	48
3.3	<i>Results and Discussion</i>	52
3.3.1	Morphology of the self-assembled Au NPs within the pores of porous silicon membranes.....	55
3.3.2	Arrangement of Au NPs within the pores of porous silicon membranes	58
3.3.3	Surface coating effect	60
3.3.4	Preliminary results of the impact of the temperature on the self-assembly behavior of Au NPs in the pores of porous silicon membranes.....	62
3.3.5	Surface-enhanced Raman spectroscopy	64
3.3.6	Conclusion	66
4	Self-assembly of 3D binary space-tessellating superstructures.....	67
4.1	<i>Introduction</i>	67
4.1.1	Self-assembly of Binary Superstructures	67
4.1.2	Space-filling polyhedron	68
4.1.3	Forces involved in the self-assembly of 3D binary superstructures.....	69
4.2	<i>Methods</i>	71
4.3	<i>Results and Discussion</i>	75
4.3.1	Self-assembly of 2D binary supercrystals by using evaporation-based self-assembly 76	
4.3.2	Self-assembly of 2D and 3D binary superstructures by using air-liquid interfacial method	78
4.3.3	Influence of Surface Ligand	82
4.3.4	Structural analysis of the 3D binary superstructure.....	83

4.4	<i>Conclusion</i>	85
4.5	<i>Appendix</i>	86
5	Conclusions and Future Directions.....	89
	List of Hazardous Substances	92
	References.....	93
	Acknowledgments.....	105
	Declaration on oath.....	107

This page is intentionally left blank

Abstract

This thesis is oriented towards the fabrication of long-range self-assembled nanoparticles (NPs) into supercrystals or superstructures and their transfer to substrates that preserve their structure and properties. The self-assembly of nanoparticles represents one of the most important discoveries of the last few years since it can lead to new controlled collective properties. Control over the size, shape, surface chemistry, and other factors is crucial for developing new technological applications. Gold nanoparticles (Au NPs) represent one example of the most used materials for self-assembly supercrystals. New advances in colloidal chemistry have enabled the manipulation of synthesis parameters to generate Au NPs with different shapes and sizes. In this context, designing, optimizing, and fabricating new supercrystals or hybrid systems with enhanced plasmonic properties could influence various research areas including fundamental studies, plasmonics, catalysis, and sensing. The work described in this thesis can be separated into three parts.

In the first part of this thesis, the optimization parameters for synthesizing high concentrations and high-quality spherical gold nanoparticles with sizes ranging from 25 nm to 120 nm were investigated. Their self-assembly into long-range AuNP supercrystals was studied in detail by using transmission electron microscopy (TEM) and scanning electron microscopy (SEM). It was shown that the quality and length of the supercrystals are highly influenced by the size and concentration of the Au NPs used as building blocks. An extensive SEM analysis revealed the coexistence of two different growth modes: layered growth, and island growth modes. Surprisingly, by modifying the polymer coating of large particles resulted in a phase transition from hexagonal-close packed to cubic-close packed structure. These results contribute to understanding the self-assembly of Au NPs and open the way for new kinds of fabricating collective plasmonic platforms with future applications in catalysis, photonics, and surface-enhanced Raman spectroscopy.

In the second part, the self-assembly of the Au NPs using porous silicon membranes as a host for the self-assembly of 2D and 3D arrays within their pores was investigated. Optimization conditions to control the self-assembly of Au NPs into the pores of porous silicon membranes are explored. Various parameters are key in this process. Especially, particle size and surface chemistry, as well

as centrifugation speed and time. Since the two different configurations achieved in this work are homogeneous and reproducible, they could represent a good choice for using them as surface-enhanced Raman (SERS) substrates. Particularly, the SERS spectra obtained from the self-assembled Au NPs arrays display a good homogeneity. This work provides guidelines for the generation of long-range hybrid systems with high quality and tunability, offering an approach for the development of porous silicon hybrid materials with unique characteristics and future applications in catalysis or as SERS active substrates.

In the last chapter, the self-assembly of complementary polyhedral nanoparticles (gold nanotetrahedra, and gold nanooctahedra) into 3D binary tessellating superstructures was investigated. The self-assembly was controlled by the polymer ligand length and depended on the concentration of polyhedral NPs. The shape, morphology, and uniformity of the 3D binary superstructures were studied in detail by using scanning electron microscopy (SEM). These results suggest that metallic polyhedral NPs have the potential to serve as fundamental units for a wide range of materials that exhibit intense light-matter interaction and open a new way for creating metamaterials with unprecedented optical properties.

As a whole, this thesis presents significant advancement in both the synthesis and self-assembly of Au NP supercrystals, the generation of hybrid systems composed of Au NPs and pSi membranes, and the self-assembly of 3D binary superstructures. The presented result could have important implications in different fields, such as sensing, light-matter coupling, SERS substrates, catalysis, or fundamental studies.

Keywords: self-assembly, superstructures, supercrystals, gold nanoparticles, electron microscopy

Zusammenfassung

Diese Arbeit befasst sich mit der Herstellung von selbstorganisierten Nanopartikeln (NPs) mit großer Reichweite zu Superkristallen oder Überstrukturen und deren Übertragung auf Substrate, die ihre Struktur und Eigenschaften bewahren. Die Selbstorganisation von Nanopartikeln ist eine der wichtigsten Entdeckungen der letzten Jahre, da sie zu neuen kontrollierten kollektiven Eigenschaften führen kann. Die Kontrolle über Größe, Form, Oberflächenchemie und andere Faktoren ist entscheidend für die Entwicklung neuer technologischer Anwendungen. Goldnanopartikel (Au NPs) sind ein Beispiel für die am häufigsten verwendeten Materialien für die Selbstorganisation von Superkristallen. Neue Fortschritte in der kolloidalen Chemie haben die Manipulation von Syntheseparametern ermöglicht, um Au-Nanopartikel mit unterschiedlichen Formen und Größen zu erzeugen. In diesem Zusammenhang könnte die Entwicklung, Optimierung und Herstellung neuer Superkristalle oder hybrider Systeme mit verbesserten plasmonischen Eigenschaften verschiedene Forschungsbereiche wie Grundlagenforschung, Plasmonik, Katalyse und Sensorik beeinflussen. Die in dieser Arbeit beschriebenen Arbeiten lassen sich in drei Teile gliedern.

Im ersten Teil dieser Arbeit wurden die Optimierungsparameter für die Synthese hoher Konzentrationen und hochwertiger sphärischer Goldnanopartikel mit Größen von 25 nm bis 120 nm untersucht. Ihre Selbstorganisation zu weitreichenden AuNP-Superkristallen wurde mit Hilfe der Transmissionselektronenmikroskopie (TEM) und der Rasterelektronenmikroskopie (SEM) im Detail untersucht. Es zeigte sich, dass die Qualität und Länge der Superkristalle stark von der Größe und Konzentration der als Bausteine verwendeten Au-NP beeinflusst werden. Eine umfassende REM-Analyse zeigte die Koexistenz von zwei verschiedenen Wachstumsmodi: Schichtwachstum und Inselwachstum. Überraschenderweise führte die Veränderung der Polymerbeschichtung großer Partikel zu einem Phasenübergang von einer hexagonal dicht gepackten zu einer kubisch dicht gepackten Struktur. Diese Ergebnisse tragen zum Verständnis der Selbstorganisation von Au-NPs bei und eröffnen den Weg für neue Arten der Herstellung kollektiver plasmonischer Plattformen mit zukünftigen Anwendungen in der Katalyse, Photonik und oberflächenverstärkten Raman-Spektroskopie.

Im zweiten Teil wurde die Selbstmontage von Au-NP unter Verwendung poröser Siliziummembranen als Wirt für die Selbstmontage von 2D- und 3D-Arrays in deren Poren untersucht. Es werden Optimierungsbedingungen zur Kontrolle der Selbstmontage von Au NPs in den Poren poröser Siliziummembranen erforscht. Verschiedene Parameter sind in diesem Prozess entscheidend. Insbesondere die Partikelgröße und die Oberflächenchemie sowie die Zentrifugationsgeschwindigkeit und -zeit. Da die beiden unterschiedlichen Konfigurationen, die in dieser Arbeit erreicht wurden, homogen und reproduzierbar sind, könnten sie eine gute Wahl für die Verwendung als oberflächenverstärkte Raman-Substrate (SERS) darstellen. Insbesondere die SERS-Spektren, die von den selbstorganisierten Au-NP-Arrays erhalten wurden, zeigen eine gute Homogenität. Diese Arbeit liefert Leitlinien für die Erzeugung von Langstrecken-Hybridsystemen mit hoher Qualität und Abstimmbarkeit und bietet einen Ansatz für die Entwicklung von porösen Silizium-Hybridmaterialien mit einzigartigen Eigenschaften und künftigen Anwendungen in der Katalyse oder als SERS-aktive Substrate.

Im letzten Kapitel wurde die Selbstmontage von komplementären polyedrischen Nanopartikeln (Goldnanotetraeder und Goldnanooktaeder) zu binären 3D-Mosaiküberstrukturen untersucht. Die Selbstorganisation wurde durch die Länge des Polymerliganden gesteuert und hing von der Konzentration der polyedrischen NPs ab. Die Form, Morphologie und Gleichmäßigkeit der binären 3D-Überstrukturen wurden mit Hilfe der Rasterelektronenmikroskopie (REM) im Detail untersucht. Diese Ergebnisse deuten darauf hin, dass metallische polyedrische NPs das Potenzial haben, als Grundbausteine für eine breite Palette von Materialien zu dienen, die eine intensive Licht-Materie-Wechselwirkung aufweisen, und einen neuen Weg zur Schaffung von Metamaterialien mit noch nie dagewesenen optischen Eigenschaften eröffnen.

Insgesamt stellt diese Arbeit einen bedeutenden Fortschritt sowohl in der Synthese als auch in der Selbstmontage von Au-NP-Superkristallen, der Erzeugung von Hybridsystemen aus Au-NP und pSi-Membranen und der Selbstmontage von binären 3D-Überstrukturen dar. Die vorgestellten Ergebnisse könnten wichtige Auswirkungen auf verschiedene Bereiche haben, wie z. B. Sensorik, Licht-Materie-Kopplung, SERS-Substrate, Katalyse oder Grundlagenforschung.

Stichworte: Selbstorganisation, Überstrukturen, Superkristalle, Goldnanopartikel, Elektronenmikroskopie

List of Publications

1. Anisotropic Thermal Transport in Tunable Self-Assembled Nanocrystal Supercrystals.
Matia Feldman, Charles Vernier, Rahul Nag, **Juan Barrios-Capuchino**, Sébastien Royer, Hervé Cruguel, Emmanuelle Lacaze, Emmanuel Lhuillier, Danièle Fournier, Florian Schulz, Cyrille Hamon, Hervé Portalés, Jame K. Utterback. *ACS NANO*, **2024**, Under Review
2. Towards Interfacing the Brain: How Nanotechnology Can Contribute.
Abdullah A. A. Ahmed, Nuria Alegret, Bethany Almeida, Ramón Alvarez-Puebla, Anne M. Andrews, Laura Ballerini, **Juan Barrios-Capuchino**, Charline Becker, Robert H. Blick, Shahin Bonakdar, Indranath Chackraborty, Xiadong Chen, Jinwoo Cheon, Gerwin Chilla, Andre Luiz Coelho Conceicao, James Delehanty, Martin Dulle, Alexander L. Efros, Matthias Epple, Mark Fedyk, Neus Feliu, Miao Feng, Rafael Fernández-Chacón, Irene Fernandez-Cuesta, Niels Fertig, Stephan Förster, Jose A. Garrido, Michael George, Andreas H. Guse, Norbert Hampp, Jann Harberts, Jili Han, Hauke R. Heekeren, Ulrich, G. Hofmann, Malte Holzapfel, Hessam Hosseinkazemi, Yalan Huang, Patrick Huber, Taeghwan Hyeon, Sven Ingebrandt, Marcello Ienca, Armin Iske, Yanan Kang, Gregor Kasieczka, Dae-Hyeong, Kostas Kostarelos, Jae-Hyun Lee, Kai-Wei Lin, Sijin Liu, Xin Liu, Yang Liu, Christian Lohr, Volker Mailänder, Laura Maffongelli, Saad Megahed, Alf Mews, Marina Mutas, Leroy Nack, Thomas G. Oertmer. Andreas Offenhäuser, Martin Oheim, Ben Otange, Ferdinand Otto, Enrico Patrono, Bo Peng, Alessandra Pichiotti, Filippo Pierini, Monika Pötter-Nerger, Maria Pozzi, Arnd Pralle, Maurizio Prato, Bing Qi, Pedro Ramos-Caber, Ute Resch Gendger, Norbort Ritter, Marten Rittner, Sathi Roy, Francesca Santoro, Nicolas W. Schuck, Florian Schulz, Erkin Seker, Marvin Skiba, Martin Sosniok, Holger Stephan, Ruixia Wang, Ting Wang, K. David Wegner, Paul S. Weiss, Ming Xu, Chenxi Yang, Seyed Shahrooz Zargarian, Yuan Zeng, Yaofeng Zhao, Dingcheng Zhu, Robert Zierold, Wolfgang J. Parak, , *ACS NANO* **2024**, Accepted
3. Plasmonic Polymorphs by Combining Shape Anisotropy and Soft Interactions in Bipyramid Thin Films.
Jules Marcone, Sabrina Jürgensen, **Juan Barrios-Capuchino**, Xiaoyian Li, Andrea Köppen, Felix Lehmkuhler, Wolfgang J. Parak, Mathieu Kociak, Marianne Impéror-Clerc, Stephanie Reich, Cyrille Hamon, and Florian Schulz. *Advanced Materials*, **2024**, Under Review.
4. Engineered self-assembly of plasmonic gold nanoparticles into 2D and 3D arrays within the pores of porous silicon membranes.
Juan Barrios-Capuchino, Patrick Huber, Alexander Petrov, Wolfgang J. Parak, and Florian Schulz. *Manuscript*, 2024
5. Deep strong light-matter coupling in self-assembled 3D binary space-tessellating superstructures.

Juan Barrios-Capuchino, Gabriela-García, Rahul Nag, Wolfgang J. Parak, Stephanie Reich, Cyrille Jamon, and Florian Schulz. *Manuscript*, 2024

Master Thesis Supervised

1. Zahra Arabi, Master in Physics, Optimization parameters for the self-assembly of binary AuNP supercrystals. In progress.
2. Samira Beiki, Master in Physics, Self-assembly of long-range nanocube supercrystals. In progress.

Internships

1. Indiana Bloomington University, Chemistry Department, Indiana, USA. Synthesis and functionalization of gold nanotetrahedral nanoparticles. Under the supervision of Dr. Xingchen Ye. December 2023-February 2024 (8 weeks).

Workshops and international schools

1. Drug Delivery Systems, 24-26th October 2022 (UUh- Hamburg, Germany)
2. Minerva Center for Bio-Hybrid Complex Systems, School and Conference, Hebrew University Jerusalem, “Bioinspired Complex Systems from Basic Science to Practical Applications” Neve Ilan (Jerusalem), Israel, 2022
3. DNA Mittel Deutschland, 1 November 2022, Leipzig, Germany

List of Figures

Figure 1. Schematic illustration of nanomaterials ranging from a scale of 1 to 100 nm ¹	1
Figure 2. Schematic illustration of the top-down and bottom-up nanofabrication methods. The top-down approach uses physical (photons, electrons, ions, etc.) or chemical (acid, bases, etc.) methods for lithography, etching, and deposition. The bottom-up approach involves cheating nanoscale structures by arranging atoms, molecules, and nanostructures through self-assembly or directed assembly ⁴	2
Figure 3. Uv Vis absorption spectra and photo of the typical absorption shift of gold nanoparticles with different particle size ¹³	3
Figure 4. Schematic illustration of surface plasmon resonance in plasmonic gold nanoparticles. The synchronized oscillation of the surface electrons is induced by the electromagnetic field of the incident light, resulting in a charge separation ²⁰	4
Figure 5. Schematic illustration of the AuNPs synthesis using the Turkevich Method ³¹	5
Figure 6. Schematics illustration of the successive growth procedure used for the preparation of AuNPs with controlled diameters increasingly tunes from 5 to 150 nm ³²	6
Figure 7. Gold nanoparticles of different shapes. a) rods ³⁴ , b) triangles ³⁵ , c) nanostars ³⁶ , d) tetrahedrons ³⁷ , and e) octahedrons ³⁸	7
Figure 8. Schematic illustration of the different experimental methods used for self-assembly of supercrystals.	9
Figure 9. Schematic illustration of the formation of gold nanorod arrays via evaporation-induced self-assembly ⁴⁸	10
Figure 10. a) Schematic illustration of the interfacial self-assembly of binary supercrystals and the substrate transfer process. b) and c) images of the resulting binary assemblies with different crystal structures ⁵⁰	11
Figure 11. Schematic illustration of some of the main driving forces of assembled supercrystals including van der Waals, electrostatic, entropic, magnetic, and molecular surface ⁵⁹	12
Figure 12. Self-assembly of nanoparticles into 2D and 3D supercrystals.	13
Figure 2.1. Transmission electron microscopy (TEM) micrographs of Au NPs with core diameters of (a) 40 nm and (b) 70 nm were used as seeds to synthesize Au NPs with diameters of 100 nm, showing bad (c) and good (d) particle quality.	26
Figure 2.2. (a-g) Transmission electron microscopy (TEM) images of self-assembled Au NPs@PSSH monolayers some of which were used as building blocks for the generation of supercrystals. Au NPs with diameters of (a) 24.8 nm ± 0.43 nm, (b) 29.2 nm ± 0.43 nm, (c) 36.8 nm ± 0.6 nm, (d) 44.4 nm ± 0.73 nm, (e) 50.3 nm ± 0.3 nm, (f) 60.3 nm ± 0.5 nm, (g) 60.3 nm ± 0.5 nm, (h) 80 nm ± 2 nm, (i) 106 ± 1.6 nm and (j) 130.2 nm ± 3.6 nm previously functionalized with 2kPSSH, 5kPSSH, 5kPSSH, 5kPSSH,	

12kPSSH, 12kPSSH, 12kPSSH, 12kPSSH, 12kPSSH, and 12kPSSH, respectively. (k) Normalized absorbance spectra of the corresponding Au NPs after being functionalized with PSSH and re-dispersed in toluene..... 28

Figure 2.3. Schematic illustration of the Au NPs@PSSH supercrystals growth. The photograph shows a typical Au NP solution on the surface of DEG into a Teflon well, followed by supercrystals forming after toluene evaporation..... 29

Figure 2.4. Scanning electron microscopy (SEM) micrographs of Au NP supercrystals which were assembled using different diameters of Au NPs. High-magnification SEM images (left) of supercrystals self-assembled from Au NPs (28 nm)@5kPSSH, Au NPs (40 nm)@5kPSSH, Au NPs (70 nm)@12kPSSH, Au NPs (80 nm)@12kPSSH, Au NPs (28 nm)@12kPSSH, Au NPs (100 nm)@12kPSSH, and Au NPs (130 nm)@12kPSSH. Low-magnification SEM images (right) of the corresponding supercrystals..... 32

Figure 2.5. SEM images of AuNP supercrystals self-assembled from Au NPs (40nm)@12kPSSH at different concentrations. The left images (a) and (b) show low-magnification SEM images of the self-assembled supercrystals at low (a) and high (b) concentrations. The right images (b) and (d) show high-magnification SEM images of the outlined square in the images (a) and (c), respectively. Image (e) shows high-magnification SEM images of the outlined square in the image (d). 35

Figure 2.6. SEM images of AuNP supercrystals self-assembled from AuNPs (40 nm)@12kPSSH at different concentrations. The left images (a and b) show low-magnification SEM images of the self-assembled supercrystals at low (a) and high (c) concentrations. The right images (b) and (d, f) show high-magnification SEM images of the outlined square in the images (a) and (b, e), respectively 36

Figure 2.7. SEM images of AuNP supercrystals self-assembled from Au NPs (70 nm)@12kPSSH at different concentrations. The left images (a-e) show low-magnification SEM images of the self-assembled supercrystals at low (a) and high (c, e) concentrations. The right images (b) and (d, f) show high-magnification SEM images of the outlined square in the images (a) and (c, e), respectively. 37

Figure 2.8. SEM images of AuNP supercrystals self-assembled from Au NPs (135 nm)@12kPSSH at different concentrations. The left images (a and c) show low-magnification SEM images of the self-assembled supercrystals at low (a) and high (c) concentrations. The right images (b) and (d) show high-magnification SEM images of the outlined squares in the images (a) and (c), respectively..... 38

Figure 2.9. SEM images of AuNP supercrystals self-assembled from Au NPs@PSSH. The left images show high magnification SEM images of supercrystals self-assembled from Au NPs (80 nm)@12kPSSH (a), Au NPs (100 nm)@12kPSSH (c), Au NPs (105 nm)@12kPSSH (e), and Au NPs (130 nm)@12kPSSH (g). The right images (b), (d), (f), and (h) show high-magnification SEM images of the outlined square in the images (a), (d), (e), and (g), respectively, which exhibit the coexistence of cubic-closed packed and hexagonal-closed packed domains..... 41

Figure 2.10. SEM images of AuNP supercrystals self-assembled from Au NPs@PSSH. The top images show high-magnification SEM images of supercrystals self-assembled from Au NPs (80 nm)@5kPSSH (a) and Au NPs (80 nm)@12kPSSH (b). The bottom middle images (c) and (d) show high-magnification SEM images of the outlined squares in the images (a) and (b), respectively. (e) and (f) images show FFT

patterns corresponding to cubic-closed packed and hexagonal-closed packed domains of the selected areas in figures (c) and (d), respectively. 42

Figure 3.1. Photograph of various pSi samples prepared at different etching conditions ⁹⁵. 45

Figure 3.1. Transmission electron microscopy (TEM) images of self-assembled Au NPs@PSSH monolayers which were used as starting materials. Au NPs of different core diameters (50 and 70 nm) were coated with PSSH of different ligands (2k and 5kPSSH). Normalized absorbance spectra of Au NPs (50 nm and 70 nm) functionalize with 5KPSSH (dark and blue) and with 12KPSSH (red and yellow) in toluene. 54

Figure 3.2. Scanning electron microscopy (SEM) image of pSi membrane which were used as starting materials. The photographs show the psi membranes before and after being tailored to a 2.3 x 2.3 mm² pSi membrane. 54

Figure 3.3. Scanning electron microscopy (SEM) images of porous silicon membranes after interaction with PSSH-functionalized Au NPs. Top view of porous silicon membranes after interacting with a) Au NPs (50 nm)@5kPSSH and b) Au NPs (70nm)@12kPSSH under several centrifugation parameters: 1,000 g for 30 min, 1,000 g for 30 min, and 1,000 g for 30 min. 57

Figure 3.4. Scanning electron microscopy (SEM) images of porous silicon membranes after interaction with PSSH-functionalized Au NPs. Top view of porous silicon membranes after interacting with a) Au NPs (50 nm)@5kPSSH and b) Au NPs (70nm)@12kPSSH under several centrifugation parameters: 1,000 g for 30 min, 1,000 g for 30 min, and 1,000 g for 30 min. 57

Figure 3.5. Cross-sectional SEM images of the porous membrane after interacting with Au NPs (50nm)@5kPSSH (a, c, and e) and (b, d, and f) Au NPs (70nm)@12kPSSH under several centrifugation parameters: 1,000 g for 30 min, 1,000 g for 30 min and 1,000 g for 30 min. 59

Figure 3.6. Scanning electron microscopy (SEM) images of porous silicon membranes after interaction with PSSH-functionalized AuNPs. Top view of porous silicon membranes after interacting with (a, c, and e) Au NPs (50 nm)@5kPSSH and (b, d, and f) Au NPs (70nm)@12kPSSH under several centrifugation parameters:1,000 g for 30 min, 1,000 g for 30 min and 1,000 g for 30 min. 61

Figure 3.7. TOP view SEM images of the self-assembly of Au NPs (50 nm)@5kPSSH and Au NPs (70 nm)@12kPSSH in the pores of pSi membranes under 100 °C. 63

Figure 3.8. SERS spectra of the polystyrene ligand molecules in the two hybrid systems. Reference spectra of 5kPSSH and 12kPSSH powder (a), microscope images of the pSi-AuNPs@5kPSSH (b) and pSi-AuNPs@12kPSSH (c) hybrid configurations, and Raman spectra of the pSi-AuNPs@5kPSSH (b) and pSi-AuNPs@12kPSSH. 65

Figure 4.1. Schematic illustration of the tetrahedral-octahedral honeycomb (TOH) structure. 69

Figure 4.2. Synthesis and characterization of gold nanotetrahedra (Au NTd) and gold nanooctahedra (Au NOct) NPs. (a) Schematic illustration of the ligand polymer exchange of AuNTd and AuNOct NPs, (b) absorbance spectra of Au NTd and Au NOct functionalized with polystyrene (PSSH, 5k). The inset shows

a photograph of Au NTd (left) and Au NOct (right) solutions functionalized with 5kPSSH and dispersed in toluene. TEM images of the (c) AuNTd50@5kPSSH and (d) AuNOct50@5kPSSH NPs, 76

Figure 4.3. Self-assembly of binary superstructures using the evaporation-based self-assembly method. a) High-magnification scanning electron microscopy (SEM) images of self-assembled complementary PSSH-functionalized Au NOct and Au NTd NPs. (b and c) Low-magnification SEM images of monolayers with small domains of the binary TOH structure. The insets show a model of the binary honeycomb structure. 77

Figure 4.4. Schematic illustration of the self-assembly of binary 2D and 3D superstructures in an air-liquid subphase using DEG. Photographs of the mixed binary solution (left image) and the formed superstructures gold film after toluene evaporation (right image). 79

Figure 4.5. Self-assembly of 2D and 3D binary superstructures self-assembled from Au NTd (50 nm)@5kPSSH and Au NOct (50 nm)@5kPSSH with a number ratio of Td : Oct (2 : 1) by using the air-liquid subphase self-assembly method. (a) Low-magnification TEM image of 2D binary superstructures and (b) high magnification TEM image of the orange outlined area. Low-magnification SEM images of the 3D binary superstructures using (c) low and (c) high concentrations of polyhedral NPs. (e and f) High-resolution SEM images of the corresponding outlined squares displaying the characteristic prims-shaped superstructure. 80

Figure 4.6. Scanning transmission electron microscopy (STEM) images of binary monolayers and multilayers. (a and c) Low-magnification STEM images of binary (a) monolayers and (c) multilayers are self-assembled from Au NTd (50 nm)@5kPSSH and Au NOct (50 nm)@5kPSSH NPs. (b and d) High-magnification STEM images of the corresponding outlined squares showing the binary TOH crystal structure. 81

Figure 4.7. Electron microscopy images of binary polyhedral NPs. (a and c) STEM and SEM images of the binary supercrystals self-assembled from Au NTd (50 nm)@12kPSSH and Au NOct (50 nm)@12kPSSH at (a) low and (c) high concentration, respectively. (c and d) High-magnification STEM and SEM images of the corresponding outlined squares showing the binary TOH crystal structure. 83

Figure 4.8. SEM images of binary polyhedral NPs. (a and c) Low-magnification SEM images of the binary supercrystals, self-assembled from Au NTd (50 nm)@12kPSSH and Au NOct (50 nm)@12kPSSH NPs at (a) low and (c) high concentration, respectively. (c and d) High-magnification SEM images of the corresponding outlined squares showing the binary TOH crystal structure. 83

Figure 4.9. 3D binary superstructures self-assembled from Au NTd and Au NOct NPs with TOH crystal structure. (a-c) High-resolution SEM images of the top view (a), side view (b), and edge view (c) of the binary 3D TOH superstructure obtained by the self-assembly of Au NTd (50 nm)@5kPSSH and Au NOct (50 nm)@5kPSSH at high concentration. The insets show schematic models of the 3D superstructures at different angles made from Au NTd (blue) and Au NOct (violet). 84

Figure A1. Low magnification SEM images of large areas with randomly self-assembled 3D binary superstructures, which are self-assembled from AuNTd@5kPSSH and AuNOct@5kPSSH at low and high concentrations. The inset shows a statistical histogram of corresponding superstructure sizes. 88

List of Tables

Table 2.1 Parameters of Au NPs@CTAC seeds used for Au NPs@CTAC syntheses.	21
Table 2.2 Au NP samples used for the formation of supercrystals and interparticle distance (gap).....	22
Table 2.3 Au NP concentrations used for the formation of supercrystals with monolayers up to several layers.....	34
Table 3.1 Parameters of Au NPs@CTAC seeds used for the synthesis of Au NPs@CTAC with diameters of 50 nm and 70 nm.	49
Table 3.2 Au NP samples used for the self-assembly experiments on the pores of porous silicon membranes.	50
Table 3.3. Optimized parameters used for the self-assembly of Au NPs@PSSH on porous silicon membranes: Dimensionality of the array, immersion time t_{immers} , NP concentrations c_{NP} , and centrifugation parameters (speed a_{cent} and time t_{cent}). All samples were prepared at RT.	64
Table 4.1 Molar concentration of polyhedral Au NPs used for the self-assembly of binary superstructures	72
Table A1 Molar concentration of polyhedral NPs used for the self-assembly of 2D and 3D binary superstructures	88
Table A2 List of chemical and GHS classifications.....	92

List of Schemes

- Scheme 2.1.** Schematic illustration of the process for the synthesis of Au NPs with diameters in the range of 25-130 nm with high quality and high concentrations. 26
- Scheme 3.1.** An idealized schematic of the self-assembly of highly ordered Au NPs@PSSH into 2D and 3D arrays within and on the surface of the pores of pSi membranes. 52
- Scheme 4.1.** Schematic illustration of the setup used for the self-assembly of binary superstructures of complementary PSSH-functionalized polyhedral NPs using the evaporation-based method..... 76

List of Abbreviations

1D	One-dimensional
2D	Two-dimensional
3D	Three-dimensional
Au NPs	Gold nanoparticles
AuNOct	Gold nanooctahedral nanoparticle
AuNTd	Gold nanotetrahedral nanoparticle
AA	Ascorbic acid
CTAB	Cetyltrimethylammonium bromide
CTAC	Cetyltrimethylammonium chloride
DEG	Diethylene glycol
EM	Electron microscopy
FFT	Fast Fourier transform
HAuCl ₄	Tetrachloroauric acid
LSPR	Localized surface plasmon resonance
NaBH ₄	Sodium borohydride
NPs	Nanoparticles
pSi	Porous Silicon
PSSH	Polystyrene
SERS	Surface enhanced Raman spectroscopy
SEM	Scanning electron microscopy
TEM	Transmission electron microscopy
THF	Tetrahydrofuran

This page is intentionally left blank

Chapter I

1 Introduction

In this introductory chapter, the concepts needed to better comprehend the work are explained. The chapter begins with a description of nanotechnology and the various methods of nanofabrication. It then delves into the properties and synthesis of gold nanoparticles. Finally, the chapter concludes with an exploration of the methods and forces involved in the formation of supercrystals.

1.1 Nanoscience and Nanotechnology

Nanoscience is the study of structures and molecules on the scales of nanometers, with at least one dimension sized from 1 to 100 nm¹. A brief summary of the many nanomaterials that are often employed is provided in **Figure 1**, along with a comparison of their sizes to biomolecules and microorganisms that are comparable in size to nanoparticles (NPs). The transfer to technological applications of these nanostructures can be called nanotechnology and today, is one of the most promising technologies of the 21st century. The National Nanotechnology Initiative (INN) in the United States describes Nanotechnology as a field of science, engineering, and technology that operates on the nanoscale (1 to 100 nm), allowing for innovative applications across various disciplines such as chemistry, physics, biology, medicine, engineering, and electronics².

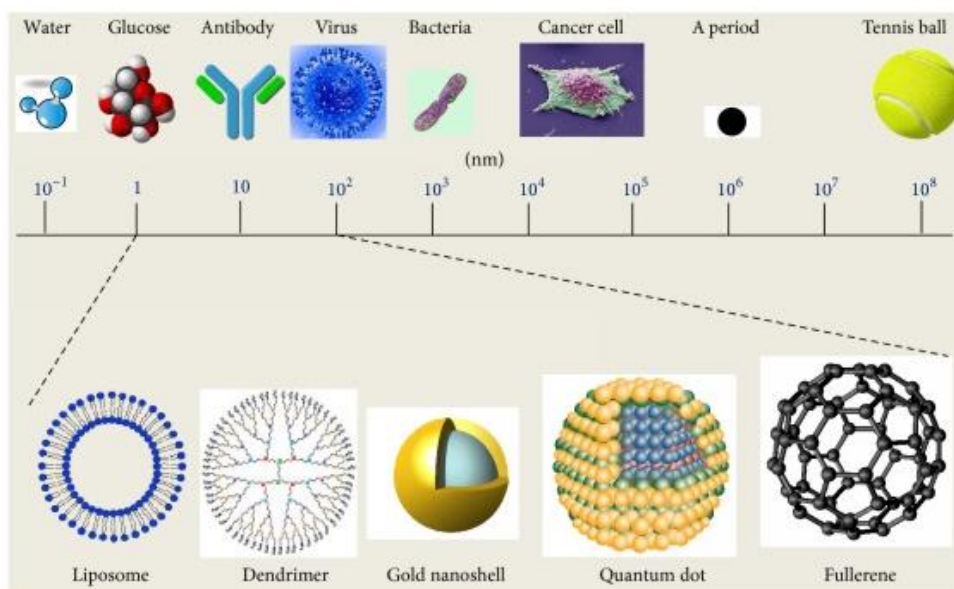


Figure 1. Schematic illustration of nanomaterials ranging from a scale of 1 to 100 nm¹.

1.2 Nanofabrication

Primarily, two strategies, top-down and bottom-up, are employed for fabricating nanostructures^{3, 4}. **Figure 2** depicts a schematic illustration of the top-down and bottom-up nanofabrication methods.

The top-down approach uses physical or chemical means to reduce a primary material to nanoscale sizes⁵. It has been widely used by the semiconductor industry to manufacture integrated circuits for consumer electronics. Some Examples of this approach are lithographic techniques, laser-beam processing, film deposition, and mechanical techniques^{6, 7}. The second approach relies on the desired structure built up through physical and chemical processes from the bottom approach, for instance, atom by atom, molecule by molecule, or cluster⁸. This approach includes chemical synthesis, self-assembly, and directed assembly^{9, 10}.

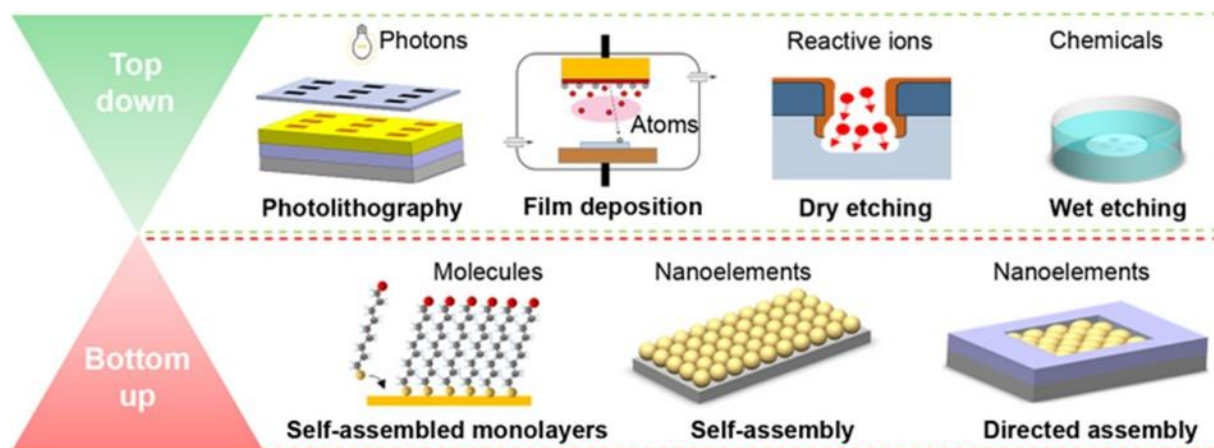


Figure 2. Schematic illustration of the top-down and bottom-up nanofabrication methods. The top-down approach uses physical (photons, electrons, ions, etc.) or chemical (acid, bases, etc.) methods for lithography, etching, and deposition. The bottom-up approach involves creating nanoscale structures by arranging atoms, molecules, and nanostructures through self-assembly or directed assembly⁴.

Among these methods for fabricating nanostructures, the self-assembly of NPs is a very versatile way to design and develop new materials with unique and tunable properties by exploiting a wide variety of combinations of particle size, shape, and composition. This point will be discussed in further sections.

1.3 Gold Nanoparticles

Among all the different NPs used in nanotechnology, gold nanoparticles (Au NPs) represent one of the most studied nanomaterials due to their unique optical, chemical, and physical properties that differ from the bulk material ^{11, 12, 13}. More recently, their unique optoelectronic properties have been utilized in various fields such as photonics, catalysis, sensing, and SERS ^{14, 15, 16, 17}. These properties depend on the size and shape of the nanoparticle ^{18, 19}. Due to these size-dependent properties, extensive research has been conducted into developing methods to control the size and shape of Au NPs ^{20, 21}.

Au NPs in aqueous solution in the visible range, between 510 nm and 550 nm, typically exhibit a single absorption peak (Figure 1). As the particle size increases (3 to 120 nm), the absorption peak shifts to longer wavelengths (red-shift), and the width of the absorption spectra is proportional to the size distribution range ^{22, 23, 11}, as seen in **Figure 3**.

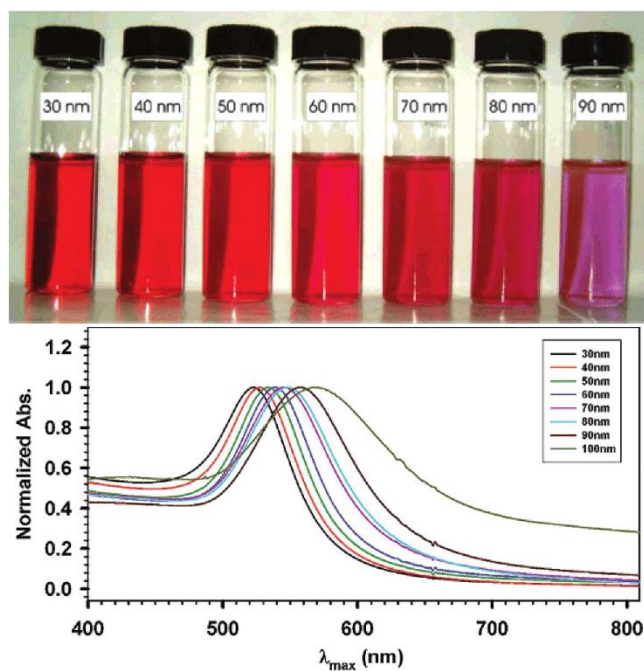


Figure 3. UV-Vis absorption spectra and photo of the typical absorption shift of gold nanoparticles with different particle size ¹¹.

1.4 Surface Plasmon Resonance (SPR)

As mentioned in the previous section, Au NPs display large electromagnetic fields at their surface when excited with light at the appropriate wavelength. Briefly, when Au NPs are exposed to a particular incident light characterized by an electric field with a wavelength much larger than the NP dimension ($\lambda(\omega) \gg r$), the oscillating electromagnetic field of the light causes the free electrons (conduction electrons) to collectively oscillate in a coherent manner²⁴. This results in a charge separation with respect to the ionic lattice, creating a dipole oscillation aligned with the electric field of the light²⁵. The maximum amplitude of this oscillation occurs at a specific frequency known as surface plasmon resonance (SPR)^{12, 26}, or localized plasmon resonance (LSPR)^{27, 19}. A schematic illustration of this process is shown in **Figure 4**.

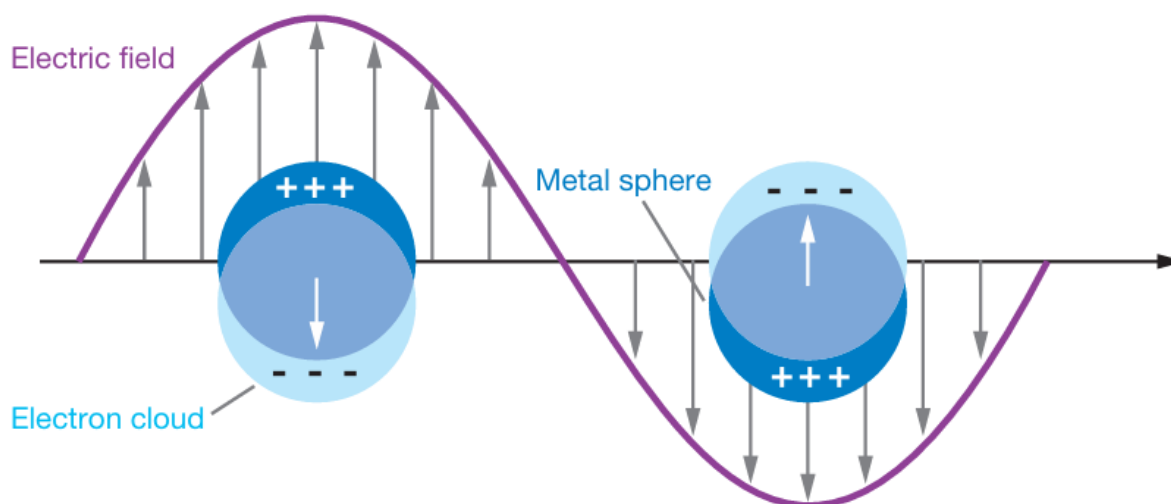


Figure 4. Schematic illustration of surface plasmon resonance in plasmonic gold nanoparticles. The synchronized oscillation of the surface electrons is induced by the electromagnetic field of the incident light, resulting in a charge separation²⁸.

The SPR band intensity and wavelength are highly sensitive to material²⁹, NP size³⁰, aggregation state³¹, and shape changes³², and the presence of plasmonic NPs³³ as well as the dielectric of the surrounding media^{34, 35}, and as a result, they can be tuned for applications at desired wavelengths through particle synthesis^{36, 25}.

1.5 Synthesis of gold nanoparticles

As previously discussed, Au NPs have attracted enormous research interest owing to their remarkable properties and potential applications. Thus, developing synthetic protocols to synthesize Au NPs with precise control over their size and shape has become very important, and there are numerous methods currently accessible for this purpose. In this regard, two methods commonly employed for producing Au NPs, particularly suitable for fabricating devices and nanostructures, are the Turkevich method and the seed-mediated growth.

1.5.1 Turkevich method

The first method, the Turkevich Method, and its recent modifications is one of the most well-known and widely preferred techniques for the synthesis of citrate-stabilized Au NPs. The process is simple and consistently generates roughly spherical Au NPs ranging from 5 to 150 nm in size that are safe and effectively stabilized by citrate ions²⁰. The process involves the reduction of gold salt, commonly HAuCl_4 with citrate as a reducing agent in an aqueous solution. The citrate stabilizer can be replaced easily with ligands like thiols, which have a stronger attraction to gold, enabling the functionalization of the Au NPs³⁷, showing its versatility. However, the synthesis of Au NPs with truly spherical shapes and precisely controlled sizes has been met with limited success. A schematic illustration of this process is shown in **Figure 5**.

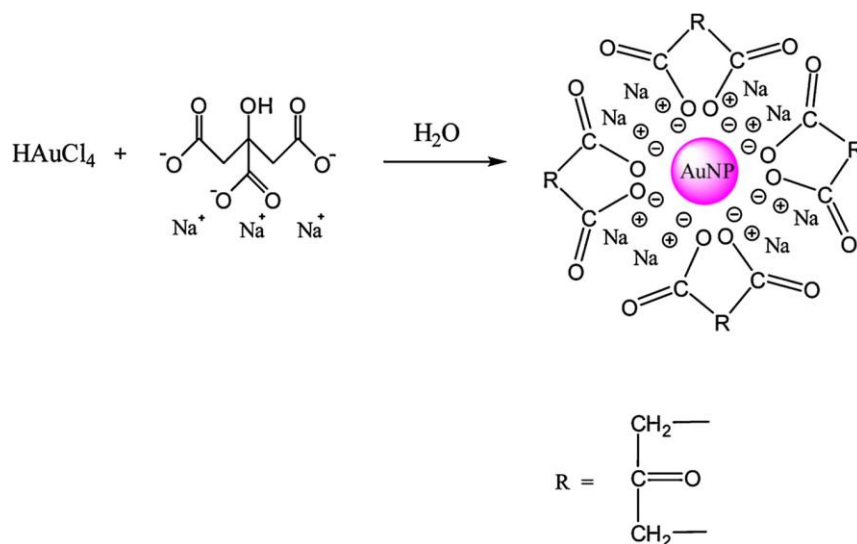


Figure 5. Schematic illustration of the AuNPs synthesis using the Turkevich Method³⁸.

1.5.2 Seed-mediated growth method

The second method, seed-mediated growth, is an easy and efficient method to synthesize monodisperse Au NPs with diameters ranging from 5 to 150 nm³⁹. This method involves the growth of small clusters followed by their further growth into larger particles in a second and third step. This approach allows the precise synthesizing of single-crystal Au NPs with excellent uniformity in terms of size and shape, which are requirements for different applications such as photonic crystals and biomedical research^{40,41}. In this process, HAuCl₄, CTAC, and AA act as Au precursor, stabilizing agent, and reductant, respectively. By using CTAB-clusters during the first growth, Au NPs with diameters of 5-16 nm can be produced. Repeating this process using larger particles as seeds results in the generation of larger NPs with sizes ranging from 15 to 150 nm. A schematic illustration of this process is shown in **Figure 6**.

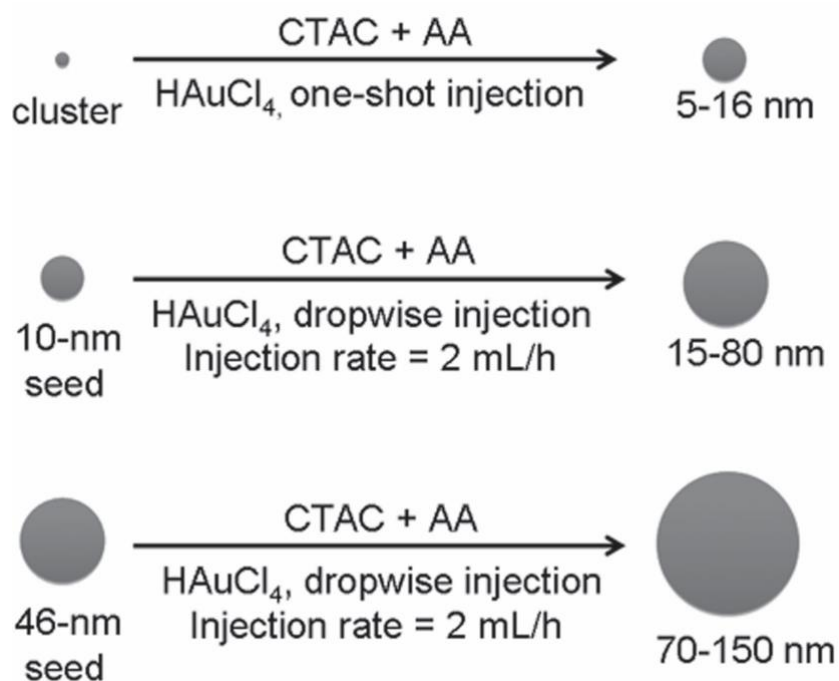


Figure 6. Schematics illustration of the successive growth procedure used for the preparation of AuNPs with controlled diameters increasingly tunes from 5 to 150 nm⁴⁰.

As can be observed, the separation of the processes of crystallization and growth of NPs in the seed-mediated method allows for better control over the size and shape of the NPs compared to the in-situ synthesis of Au NPs. In particular, the seed-mediated method enabled the creation of

Au NPs with various shapes such as rods ⁴², triangles ¹⁷, nanostars ⁴³, tetrahedrons ⁴⁴, and octahedrons ⁴⁵, as shown in **Figure 7**. In these processes, the chemicals (reducing agent and capping agents) interact with specific crystalline facets of the growing seeds to promote symmetry breaking in NPs growth ^{46, 47, 48}.

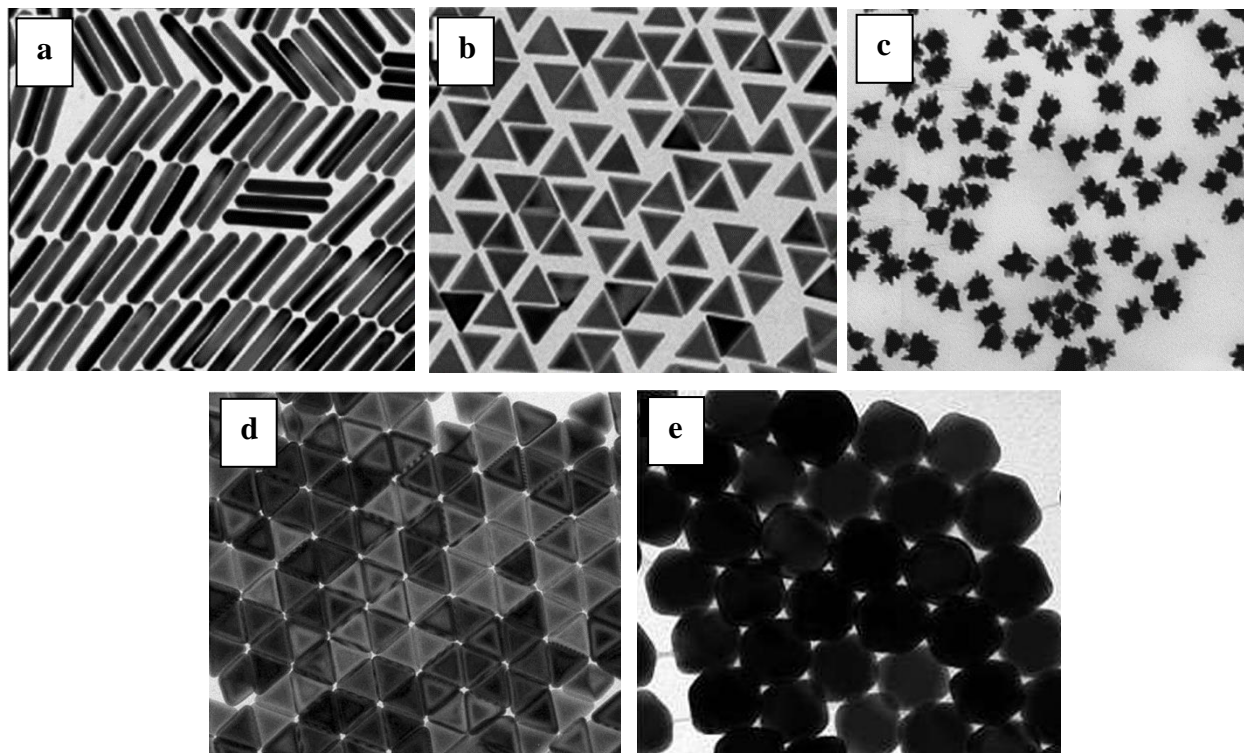


Figure 7. Gold nanoparticles of different shapes. a) rods ⁴², b) triangles ¹⁷, c) nanostars ⁴³, d) tetrahedrons ⁴⁴, and e) octahedrons ⁴⁵.

1.6 Surface stabilization of nanoparticles

After synthesizing and purifying the NPs to an acceptable degree, it is often necessary to modify their surface to stabilize them, since several factors can influence their stability in solutions, which could lead to their aggregation. Surface functionalization of NPs involves the use of covalent and non-covalent bonds (hydrogen bonds, electrostatic or van der Waals interactions) to attach various organic and inorganic molecules to the surface of the NPs to stabilize them ⁴⁹. These ligands are selected depending on the NP's core and the desired application ⁵⁰. Some common ligands to stabilize the NPs are surfactants (i.e., CTAC, CTAB) ³⁹, polymers ³⁸ and DNA ⁵¹.

In summary, surface functionalization can serve to achieve different objectives such as a) deactivate extremely reactive NPs, b) stabilize and prevent the aggregation of NPs in a medium (i.e., like a solvent) and c) modify the surface for applications such as molecular recognition, or promote the self-assembly of NPs into complex structures.

1.7 Self-assembly of nanoparticles

Self-assembly is a process in which an unordered system with existing parts creates an organized pattern through specific interactions among its components without external guidance. Self-assembly mechanisms can be found in both nature and technology. They involve numerous types of interaction and components ranging in size from molecules or molecules (i.e., crystals) to the planetary (i.e., weather systems) scale⁵². The self-assembly word is being applied more across various fields, each with its particular focus and approach. Among these, self-assembly is one of the most effective methods for building functional nanostructures with unique properties, thus it is becoming important in nanotechnology⁵². For instance, a long-range interaction with a suitable magnitude must be dominant to form a self-assembled ordered nanostructure rather than a random assembly. The strength of this interaction is highly influenced by the size and shape of the NPs and typically occurs at the atomic scale^{53,54}.

Due to the advancements in colloidal chemistry methods to synthesize well-controlled size⁵⁵, geometry⁵⁶, composition⁵⁷, and surface modifications⁵⁸, several self-assembly strategies have been proposed to develop ordered superlattices, also named supercrystals, with distinctive spatial and unique properties⁵⁹. **Figure 8** shows a schematic illustration of different experimental methods used for the self-assembly of supercrystals. Among these approaches, the two most commonly used methods for the self-assembly of NPs into 2D and 3D supercrystals are the evaporation-based self-assembly and the air-liquid subphase method. These methods will be discussed in the next sections.

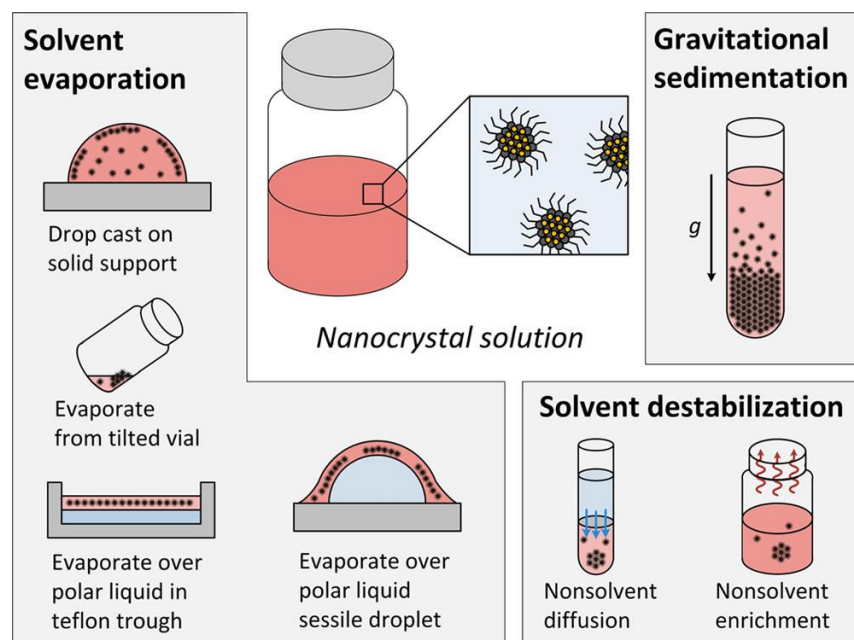


Figure 8. Schematic illustration of the different experimental methods used for self-assembly of supercrystals.

1.7.1 Evaporation-induced self-assembly

One of the most common methods for self-assembly supercrystals is evaporation-induced self-assembly. This method usually results in the formation of superlattices thin films, occurring when the solvent evaporates and self-assembly begins when the concentration threshold is reached. Several new methods were created to produce supercrystals with specific sizes and structures, utilizing evaporation-driven processes in drying droplets and thin films ⁶⁰. In short, this approach consists of the drop-casting of a small volume of the desired NPs solution, usually a concentrated solution, onto a solid surface (i.e., silicon substrate, glass, or TEM grids) and allowing it to dry for a few minutes. As the NP concentrations increased to a certain point, the supercrystals started forming ⁶¹. A schematic illustration of this process is shown in **Figure 9**. An additional change to this method involves the transferring of the mixture into a small glass vial. This improves the process by facilitating the tilling of the substrate and controlling the movement of the meniscus. Thus, generating long-range superlattices ⁶². This method has been used for the construction of supercrystals with multiple NPs. For instance, using this method has led to the formation of binary supercrystals ^{63, 64}.

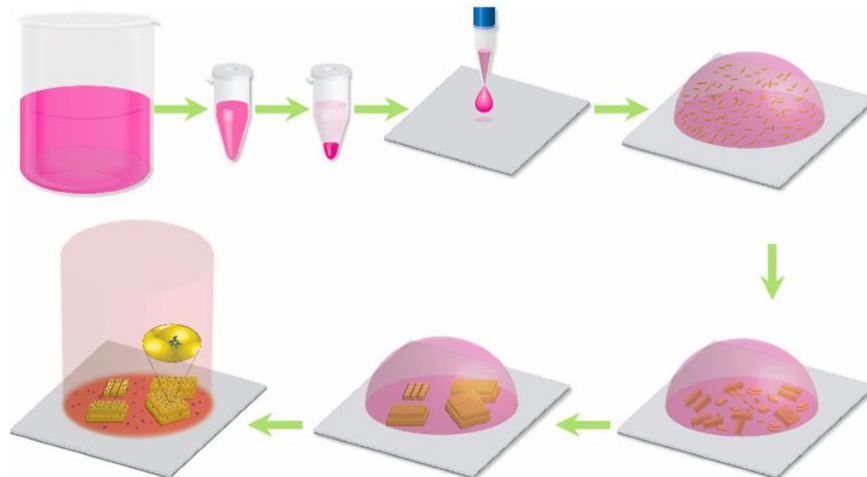


Figure 9. Schematic illustration of the formation of gold nanorod arrays via evaporation-induced self-assembly ⁶¹.

1.7.2 Air-liquid interfacial self-assembly

Another common self-assembly method is known as liquid-air (or liquid-liquid) interface self-assembly. This involves the generation of supercrystals at the air-liquid subphase, for example, by using a chemically inert liquid surface with a low evaporation rate as diethylene glycol (DEG). This technique involves depositing nanoparticles (NPs) that are dissolved in an organic, non-polar solvent onto a polar subphase, DEG. Since the subphase is immiscible and denser than the NPs solvent, the NPs solution remains on top without mixing with the subphase, leading to the formation of supercrystals ⁶⁵. After spreading the NPs solution onto the liquid surface, usually, a glass slide is placed on top to reduce the evaporation rate of the liquid ⁶⁶. The thin self-assembled supercrystals on the surface of DEG can be easily collected from the liquid surface and transferred to a desired substrate ⁶⁵. The thickness, structure, and self-assembly behavior of the superstructure can be controlled by modifying the solvent and NP concentration⁶⁷. Several interesting crystal structures have been developed using this method ^{68, 69, 70}. A schematic illustration of this process is shown in **Figure 10**.

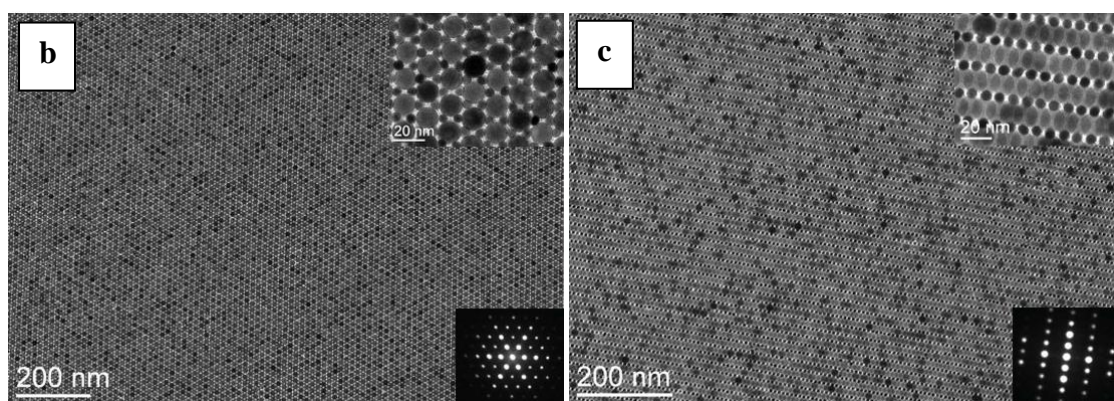
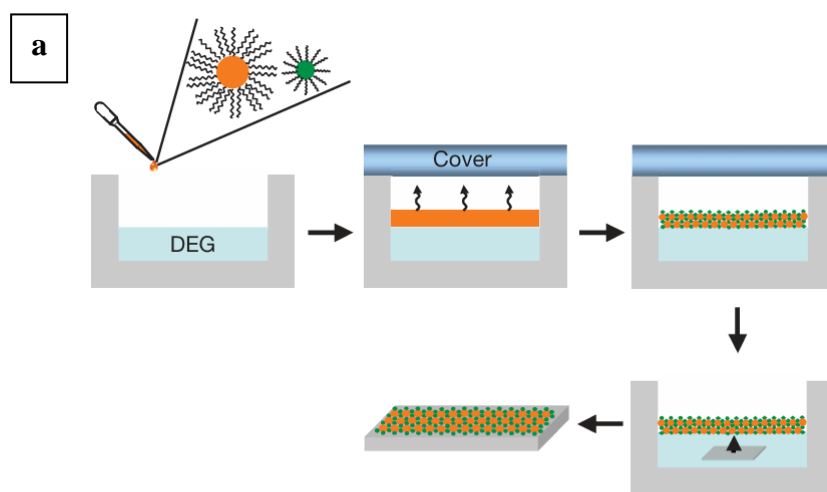


Figure 10. a) Schematic illustration of the air-liquid subphase method for self-assembling binary supercrystals and the substrate transfer process. b) and c) images of the resulting binary assemblies with different crystal structures ⁶⁵.

1.7.3 Interactions involved in the self-assembly of NPs

At the nanoscale, the self-assembly of NPs is controlled by dominant forces such as NPs interaction ⁷¹, size and shape of the NPs ^{72, 73}, the organic ligands on the surface of the NPs ⁷⁴, Van der Waals ⁷⁵, electrostatic interactions ⁷⁶, hydrophobic interactions ⁷⁷, and dipole-dipole interactions between the core diameters of the NPs ⁷⁸, as well as interactions with a substrate or interface ⁷⁹, and solvent quality ^{80, 81}. A schematic illustration of some of these interactions is presented in **Figure 11**, In summary, if the appropriate conditions are correctly encoded, the self-assembly of NPs should

process by itself towards the most stable ordered structure. Thus, by carefully designing the colloidal system, it is possible to induce the self-assembly of NPs into long-ordered supercrystals.

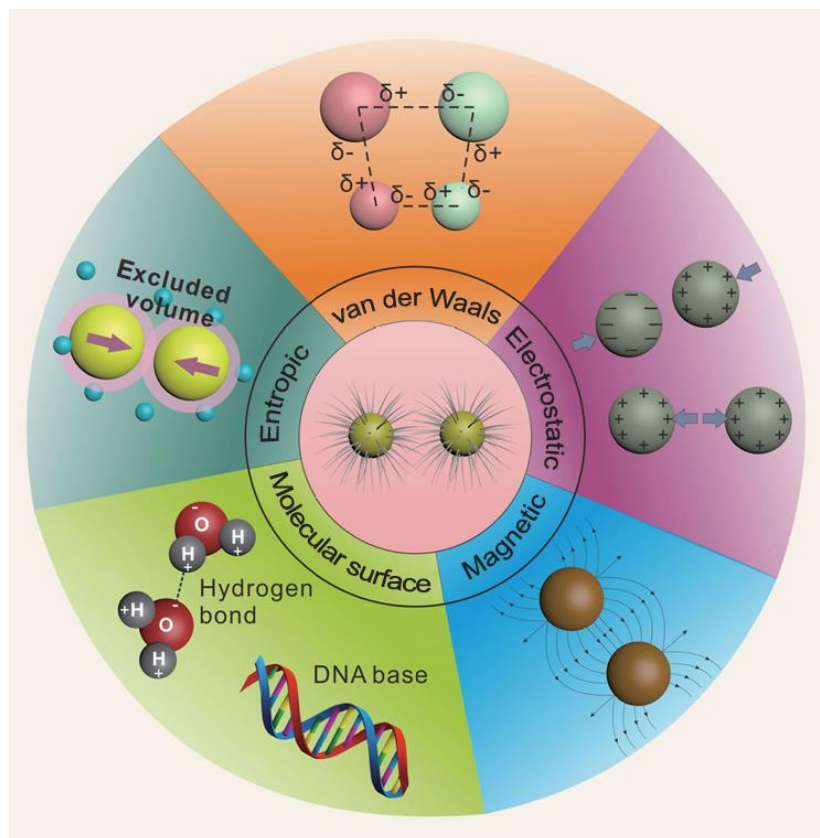


Figure 11. Schematic illustration of some of the main driving forces of assembled supercrystals including van der Waals, electrostatic, entropic, magnetic, and molecular surface ⁷⁶.

1.7.4 Applications of self-assembled supercrystals

One motivation for designing and studying the self-assembly of supercrystals lies in their ability to exhibit unique properties such as electrical, optical, and mechanical properties ^{82, 83, 84, 82, 85, 86, 87}, which are not found in individual NPs. Thus, the self-assembly of NPs into two-dimensional (2D) and three-dimensional (3D) supercrystals has been extensively studied in recent years due to the emergence of those new properties. The self-assembly of these supercrystals has numerous fascinating applications in diverse fields such as plasmonics ^{88, 89, 90}, photonics ⁹¹, phononics devices ⁹², as well as in catalysis ^{93, 94}. A comprehensive discussion with several examples of the

applications of the supercrystals can be found in the reviews of Borah et al ⁹⁵ and Xu et al ⁷⁹. A schematic illustration of the different self-assembly methods, classification, and applications of supercrystals is provided in **Figure 12**.

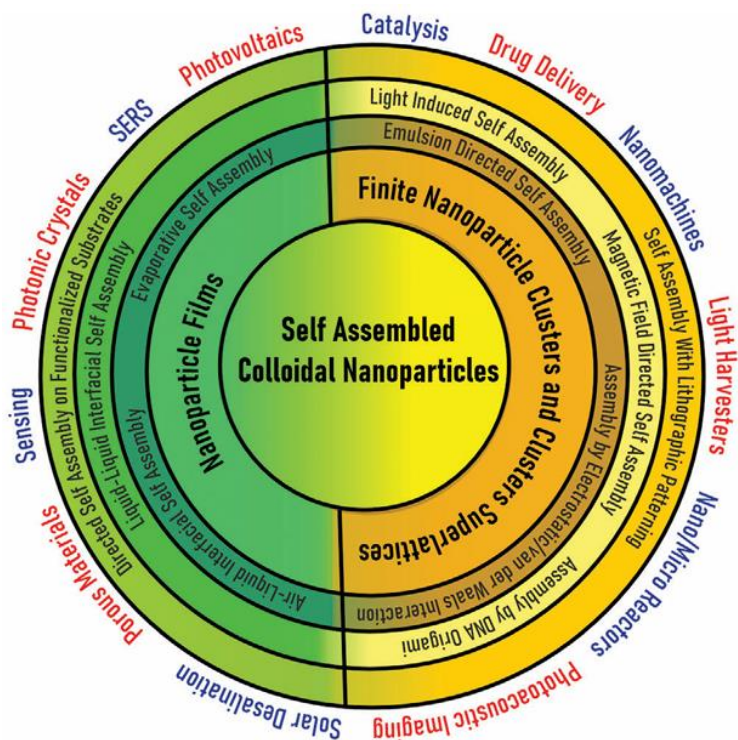


Figure 12. Applications of the self-assembly of nanoparticles into 2D and 3D supercrystals.

1.8 Outline of this Thesis

The self-assembly of plasmonic Au NPs is one of the most fascinating ways to produce supercrystals and hybrid materials with unique collective plasmonic properties. The understanding of the process that involves the creation of these structures. The goal of this thesis was to gain a deeper understanding of the self-assembly of long-range supercrystals and how various initial parameters, such as the particle concentration, size, and polymer ligand coating affected the structural feature of the resulting supercrystals.

In addition, to improve the technological transfer of supercrystals made of Au NPs, the scientific community must develop optimized methods that allow better control of the resulting supercrystals. Developing optimized methods that allow fine control over the supercrystals, for example, the use of a porous matrix could lead to keeping the properties of the supercrystals, high periodicity and uniformity, which are highly desired for the technological transfer of these materials. This thesis has the following primary aims:

1. Synthesize long-range self-assembled supercrystals self-assembled from Au NPs with diameters in the range of 25 nm-130 nm.
2. Engineer the self-assembly of highly ordered Au NPs into porous silicon membranes and the result SERS functionality of the hybrid system.
3. Synthesis of self-assembled 3D binary superstructures.

Combined these aims will contribute to building the necessary knowledge for reaching long-range superstructures, hybrid nanostructures, and binary superstructures which could lead to a new set of materials with outstanding plasmonic collective properties.

1.9 Thesis Overview

The structure of this thesis is as follows:

In Chapter II, we present the synthesis of Au NPs with different sizes. The initial process consisted of optimizing the necessary parameters for achieving high uniformity and high quality of spherical Au NPs. Particles with sizes ranging from 25 nm up to 130 nm and their self-assembly into long-range supercrystals are systematically investigated using transmission electron microscopy (TEM) and scanning electron microscopy (SEM). The impact of the particle

concentration on the final supercrystals was also investigated. We finally moved into the different growing modes that are present in the supercrystals composed of Au NPs with diameters above 70 nm. Interestingly, two different crystal phases, cubic-close packed and hexagonal-close packed, were observed on supercrystals self-assembled from Au NPs with diameters larger than 70 nm.

In Chapter III, we present porous silicon membranes that allow the use of its internal porous matrix as a support for the self-assembly of Au NPs. In this part, the self-assembly of Au NPs functionalized with PSSH within the pores of porous silicon membranes was investigated by modifying diverse parameters such as particle size, surface chemistry as well as centrifugation speed and time. High-resolution SEM methodology was used to unveil the arrangement of the Au NPs within the pores of the porous silicon membranes. Large micrometer areas with 2D and 3D arrays of AuNPs were successfully generated.

In Chapter IV, the self-assembly of 3D binary superstructures was investigated by combining two different complementary polyhedral NPs. Evaporation at air-liquid interfacial self-assembly allows for the fabrication of superstructures of large quality. SEM and TEM data provided the mechanism growth of these binary superstructures in a TOH honeycomb structure. In addition, optical characterization unveiled the generation of ultra-strong coupling inside the supercrystals, resulting in the generation of plasmon-polaritons. This could open a wide range of applications such as plasmonic, mechanical, or SERS.

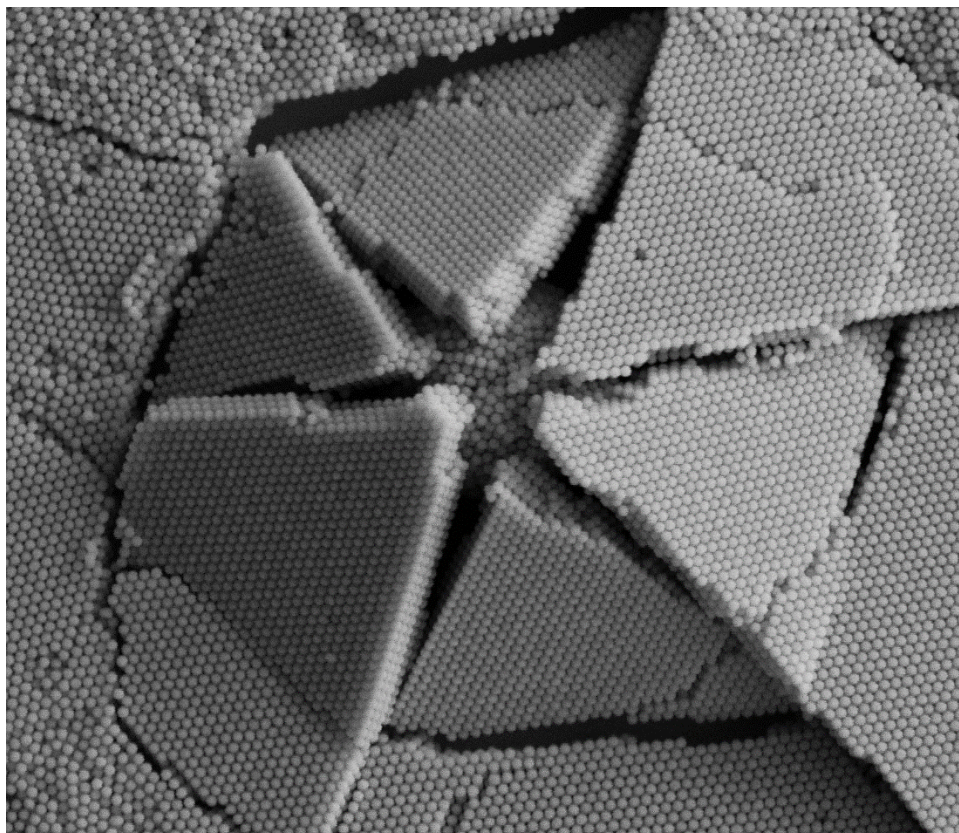
In Chapter V, a summary of the significant findings and achievements of this thesis work are discussed. Also, it includes future potential directions related to results discussed in Chapter I-III, for example, the self-assembly of long-range Au NP supercrystals, the fabrication of hybrid materials, and the generation of 3D binary superstructures.

As a whole, this thesis has provided significant advancements in the synthesis of high concentrations of Au NPs with high quality and their self-assembly into long-range supercrystals, the easy and robust method to apply the self-assembly of Au NPs within and on the pores of porous silicon membranes as well as advancing the knowledge on the successful generation of 3D binary systems with complex superstructures. The general concept may thus be expanded to understand the growth mechanism of these superstructures. This however remains a challenge for the future.

This page is intentionally left blank

CHAPTER II

2 Self-assembly of Au NPs into long-range supercrystals



2.1 Introduction

2.1.1 Self-assembly of 2D and 3D plasmonic supercrystals

The self-assembly of plasmonic gold nanoparticles (Au NPs) into 2D and 3D supercrystals with microscopic structures represents a fascinating research field in material science⁹⁶, both for fundamental studies and for potential technological applications^{97, 98}. These supercrystals possess not only the individual properties of Au NPs but also collective properties, which originate from interparticle coupling^{99, 100}. For instance, the surface plasmon resonance (SPR) of the individual NPs would then couple and originate collective modes, producing photonic standing waves penetrating the supercrystals¹⁰¹. These properties can be tailored by modifying the particle size,

surface ligand coating, and the crystal structure of the supercrystals¹⁰². However, the self-assembly of Au NPs into microscopic and macroscopic supercrystals with well-ordered and high uniformity remains challenging.

2.1.2 Importance of homogeneous self-assembly

In order to take advantage of the collective plasmonic properties provided by the supercrystals, it is necessary to develop robust protocols that allow the fabrication of long-range and well-ordered supercrystals. To achieve well-defined supercrystals, Au NPs with low dispersity and high uniformity are necessary¹⁰³. In addition, particle concentration and ligand coating also play an important role^{104, 105}. Furthermore, thanks to the improvement in colloidal chemistry that has allowed the synthesis of high-quality NPs with controlled compositions, dimensions, and morphology, these protocols can be modified and improved to produce high-quality NPs that can serve as building blocks for generating Au NP supercrystals with well-ordered and long-range⁴⁰. In addition, the understanding of the mechanisms ruling nanoparticle self-assembly represents an important step toward the fabrication of novel materials with tailored optical, mechanical, plasmonic, or thermal properties⁹⁸.

2.1.3 Applications of Au NP supercrystals

Due to their periodic organization and high uniformity, supercrystals of Au NPs can exhibit interesting collective plasmonic properties that have a wide range of important applications. For instance, by easily manipulating the supercrystals by modifying the particle size and surface coating, as well as adjusting the number of Au NP layers, it is possible to manipulate light¹⁰⁶. For instance, these periodic arrangements have shown the activation of well-defined plasmon-polariton modes with a regime in a deep-strong light-matter coupling¹⁰⁷. In this same context, Mueller et al¹⁰⁸, have shown that Au NP supercrystals can confine the light into well-defined and periodic hot spots, which can be utilized for plasmon-enhanced spectroscopies such as surface-enhanced Raman scattering (SERS) and surface-enhanced infrared spectroscopy. Another very promising direction is plasmonic photocatalysis. For instance, Herran et al⁹⁴, have shown that incorporating catalytic platinum NPs inside of the gaps of the supercrystals leads to a boosted

catalytic activity of platinum NPs. These examples show the importance of generating protocols for achieving long-range and well-defined supercrystals.

The ordered self-assembly of Au NP supercrystals should result in new collective plasmonic and optical properties. This includes tunable crystal symmetry and geometry. Therefore, it is important to synthesize supercrystals with precise control over the number of layers, and long-range, and micrometer sizes. This is crucial for understanding the self-assembly of Au NPs and for potential future technological applications

In summary, this chapter will cover the optimized parameters for synthesizing high concentrations and high-quality Au NPs with diameters sizes in the range of 25-135nm. The parameters for self-assembly long-range Au NP supercrystals were also investigated. The supercrystals were prepared by induced self-assembly in an air-liquid subphase using DEG. The SEM and TEM characterization techniques revealed the successful generation of long-range supercrystals with high quality and uniformity through extended micrometer areas. The impact of the concentration of Au NPs in the supercrystals formation was also investigated. Interestingly, different growth modes were found. Highlighting the importance of the NPs concentration on the formation of the AuNP supercrystals.

Finally, the coexistence of cubic close-packed and hexagonal close-packed constituting the supercrystals was observed when Au NPs with larger core diameters, 70 nm, 80 nm, 105 nm, and 135 nm, and functionalized with 12kPSSH were used. When particles with diameters of 80 nm were coated with 5kPSHH, larger domains that involved cubic-closed packed domains were found, suggesting that the polymer ligands play a key role in controlling the phase transition. Due to the high quality and high order of supercrystals made of Au NPs with different sizes achieved in this thesis, these materials could be excellent candidates for developing plasmonic, active SERS substrates and catalytic materials.

2.2 Methods

Materials

Tetrachloroauric (III) acid ($\geq 99.99\%$ trace metal basis), trisodium citrate dihydrate ($\geq 99.99\%$), ascorbic acid (AA, $\geq 99.99\%$), sodium borohydride (NaBH_4 , $\geq 98\%$), cetyltrimethylammonium bromide (CTAB, $\geq 99.99\%$), and cetyltrimethylammonium chloride (CTAC, 98%) were ordered from Sigma-Aldrich. Thiolated polystyrenes (PSSH, PSSH_{2k}: M_n : 2800 g mol⁻¹, PSSH_{5k}: M_n : 5300 g mol⁻¹, M_w = 5800 g mol⁻¹; PSSH_{12k}: M_n =5800 g mol⁻¹, M_w =12,400 g mol⁻¹) were purchased from Polymer Source (Canada). Toluene ($\geq 99.95\%$), tetrahydrofuran ($\geq 99.5\%$), and ethanol (denat., 96%), were from VWR (USA). DEG (reagent grade) was from Merck (Germany). The respective purities are given in the brackets. Ultrapure water (10.2 M Ω cm, Millipore) was used for all experiments. All reagents were used without any additional treatment. All the glassware used in the experiments was cleaned with fresh aqua regia and rinsed several times with MQ.

Synthesis of Au NPs of different diameters

Gold nanoparticles (Au NPs) with core diameters ranging from 20 to 110 nm were synthesized according to the seeded growth protocol presented by Zheng et al.⁴⁰ with minor modifications, for instance, scaled up by a factor of 10 to achieve high AuNP concentrations. Briefly, for the preparation of the initial CTAB-stabilized seeds, sodium borohydride (NaBH_4 , 600 μL , 10 mM) was quickly added into a 10-mL mixture of CTAB (5 mL, 200 mM) and tetrachloroauric (III) acid (HAuCl_4 , 5 mL, 0.5 mM) under rapid stirring (900 rpm). The final mixture remained undisturbed at 30°C for 3 h using an oil bath.

For the first growth step, aqueous solutions of AA (1.5 mL, 100 mM) and CTAC (2.0 mL, 200 mM) were mixed with 50 μL of the initial CTAB-seeds at 900 rpm, followed by one shot injection of HAuCl_4 (2 mL, 0.5 mM). The newly synthesized AuNPs were stirred at 900 rpm for 15 min. The AuNPs were collected by centrifugation (21,000 g, 30 min). These Au NPs were dispersed in CTAC (1 mL, 20 mM), used as seeds, and adjusted to ≈ 21 nM for growing larger AuNPs. The concentration of the particles was calculated based on the absorbance at 450 nm as described by Haiss et al.²².

For the second growth to synthesize Au NPs with diameters in a range of 40-70 nm, an aqueous solution of AA (1.3 mL, 10 mM) and CTAC (20 mL, 100 mM) was mixed with 150 μ L of the previous AuNPs seeds at 600 rpm and treated with ultrasound for 1 min, afterward, followed by a dropwise injection of HAuCl₄ (20 mL, 0.5 mM). The Au NPs were washed two times via centrifugation (9,000 g, 30 min) and re-dispersed in 20 mM of CTAC for the next growing step. The AuNP seeds can be stored at 4 °C for a long-time duration.

For the third growth step to synthesize Au NPs with diameters in a range of 60-90 nm, an aqueous solution of AA (1.3 mL, 10 mM) and CTAC (20 mL, 100 mM) was mixed with 300 μ L of the previous Au NPs at 600 rpm and treated with ultrasound for 10 min, afterward, followed by a dropwise injection of HAuCl₄ (20 mL, 0.5 mM). The Au NPs were washed twice via centrifugation (5,000 g, 30 min) and re-dispersed in 1 mL MQ.

For the fourth growth step to synthesize Au NPs with diameters in the range of 100- 120 nm, an aqueous solution of AA (1.3 mL, 10 mM) and CTAC (20 mL, 100 mM) was mixed with 300 μ L of the previous Au NPs at 600 rpm and treated with ultrasound for 10 min, afterward, followed by a dropwise injection of HAuCl₄ (20 mL, 0.5 mM). The Au NPs were washed as described above twice via centrifugation (5,000 g, 30 min) and re-dispersed in 1 mL MQ.

The Au NPs@CTAC batches were stored at 4°C for an extended period of time.

The optimized parameters for synthesizing Au NPs with diameters in the range of 25-135 nm and with high uniformity are summarized in Table 1.

Table 2.1 Parameters of Au NPs@CTAC seeds used for Au NPs@CTAC syntheses.				
Sample	V_{seeds} (l)	d_{seeds} (nm)	c_{seeds} (nM)	
Au NPs (25 nm)@CTAC	1.5 mL	11.5 nm	~21	
Au NPs (30 nm)@CTAC	1.0 mL	11.5 nm	~21	
Au NPs (40 nm)@CTAC	300 μ L	11.5 nm	~21	
Au NPs (50 nm)@CTAC	120 μ L	11.5 nm	~21	
Au NPs (70 nm)@CTAC	250 μ L	40 nm	~3.73	
Au NPs (80 nm)@CTAC	250 μ L	40 nm	~3.73	
Au NPs (100 nm)@CTAC	300 μ L	70 nm	~0.62	

Au NPs (110 nm)@CTAC	300 μ L	70 nm	~0.62
Au NPs (120 nm)@CTAC	300 μ L	70 nm	~0.62
Au NPs (135 nm)@CTAC	300 μ L	70 nm	~0.62

Surface ligand exchange of Au NPs

A direct ligand exchange on the Au NPs was performed based on the protocol presented by Schulz et al.¹⁰³. Briefly, the previously synthesized NPs were centrifuged and concentrated to a volume of ~100 μ L and then added into a vigorously stirred (600 rpm) round flask that contained a solution of PSSH-ligands in THF (6 ml, 1 mM). The reaction was left overnight. Next, the THF solution of Au NPs@PSSH was dried under a rotary evaporator, and the film residue was filled with 1 mL of toluene and purified 3 times (7,000 g, 15 min). To eliminate excess PSSH ligands and concentrate the particles for the next supercrystals production, the solution underwent two rounds of centrifugation. Any remaining CTAC can negatively impact ordered film formation and should be eliminated by repeatedly washing the toluene phase with water if needed. For this process, equal parts of water and ethanol are combined with the Au NPs@PSSH in toluene to create a 1:1:1 mixture. Following thorough mixing and phase separation, the toluene layer containing Au NPs@PSSH is extracted, and the procedure is repeated. In cases where phase separation is problematic, sodium chloride can be introduced. Finally, the resulting Au NPs@PSSH were concentrated (7,000 g, 15 min) in 0.5 mL of toluene for the self-assembly of supercrystals. The concentrations of Au NPs used for further self-assembly experiments are described in Table 2.

Table 2.2 Au NP samples used for the formation of supercrystals and interparticle distance (gap).

Sample	AuNP diameter (nm)	Polymer ligand	Particle Concentration (nM)	Gap (TEM) (nm)
Au NPs (25 nm)@2kPSSH	28	2kPSSH	~22.47	~1.9
Au NPs (28 nm)@5kPSSH	35	5kPSSH	~13.5	~1.9
Au NPs (40 nm)@5kPSSH	40	12kPSSH	~7	~1.9
Au NPs (50 nm)@12kPSSH	50	12kPSSH	~2.2	~1.9

Au NPs (60 nm)@12kPSSH	60	12kPSSH	~0.42	~3.5
Au NPs (70 nm)@12kPSSH	70	12kPSSH	~0.42	~3.5
Au NPs (80 nm)@12kPSSH	80	12kPSSH	~0.61	~3.5
Au NPs (100 nm)@12kPSSH	100	12kPSSH	~0.336	~1
Au NPs (120 nm)@12kPSSH	120	12kPSSH	~0.141	~1
Au NPs (135 nm)@12kPSSH	120	12kPSSH	~0.08	~1-3

Self-assembly of AuNP supercrystals

The method developed by Dong et al. was used for the self-assembly of long-range supercrystals⁶⁵. In almost all the experiments 100 μ L of the Au NPs@PSSH were mixed with 100 μ L of toluene and dispersed carefully pipetted onto 600 of DEG in a Teflon well (inner diameter 1.0 cm, max. vol = 2.0 mL). The well was covered with a circular glass slide to decrease the evaporation rate of toluene. The normal waiting time for the supercrystals formation was 48 hours after the toluene was completely evaporated and a golden film appeared. The sample was carefully transferred to silicon substrates or carbon-coated TEM grids for morphology characterization.

Uv-Vis absorption spectroscopy

Absorbance measurements were carried out using a Cary Eclipse 60 Spectrometer at room temperature. The absorbance of MQ water in the same cuvette used for the Au NPs@CTAC was measured as a reference in all the experiments before functionalization. Quartz cuvettes (Hellma QS, Hellma, Germany) were used to measure the absorbance of Au NPs after functionalization with PSSH and dispersed in toluene. The Au NPs and Au NPs@PSSH concentrations were estimated with the absorbance at 450 nm as described by Haiss et al²².

Morphological characterization

Scanning electron microscopy (SEM) images were obtained using a Zeiss Sigma operated at an accelerating voltage of 10 kV. To characterize the morphology and the self-assembly arrangement of the AuNP supercrystals, the previously collected samples on silicon and carbon-coated TEM grid were directly deposited on a carbon tape and attached to an SEM holder clip, respectively.

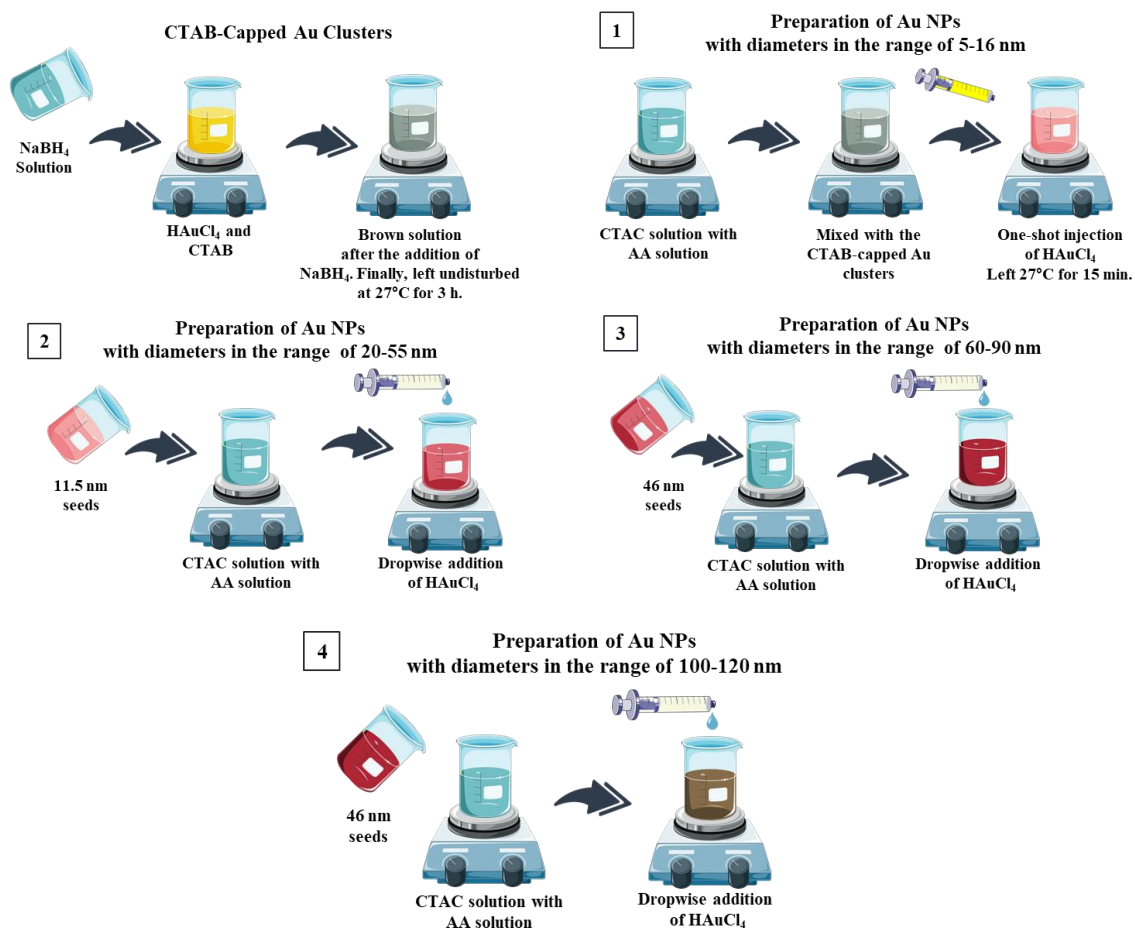
High-resolution micrographs were obtained using the InLens detector. The typical working distance used was in the range of 2.5-5 mm.

Transmission electron microscopy (TEM) micrographs of Au NPs@PSSH were performed on a JEOL JEM-1011 microscope with an operating voltage of 100kV. The TEM samples were prepared by dropping 10 μ L of NPs solution onto a carbon-coated TEM grid. The NP diameters d were calculated by using the software Image J 1.53e from the TEM image.

2.3 Results and Discussion

2.3.1 Optimization parameters for the synthesis of high-quality and high concentration of Au NPs

Gold nanoparticles (Au NPs) were synthesized based on the seed-mediated growth protocol presented by Zheng et al.⁴⁰ as the working basis for synthesizing long-range supercrystals and then scaled up 10 times to obtain higher concentrations of Au NPs. **Scheme 2.1** depicts a schematic illustration of the four steps needed in the synthesis of Au NPs with diameters in the range of 25-125 nm, with minor modifications to the original procedure. For instance, 11.5 nm Au NPs were produced by utilizing CTAB-capped particles as the initial seeds. Next, the newly synthesized particles were used as seeds to produce particles in the range of 40-46 nm. Then, Au NPs with diameters of 46 nm were used as seeds to create Au NPs with diameters in the range of 60-70 nm. Finally, to obtain Au NPs with diameters in the range of 100-135 nm, Au NPs with diameters of 70 nm were used as seeds.



Scheme 2.1. Schematic illustration of the process for the synthesis of Au NPs with diameters in the range of 25-130 nm with high quality and high concentrations.

Incorporating this last step is crucial for synthesizing high-quality Au NPs with diameters larger than 70 nm. For example, using Au NPs with diameters of 40 nm to directly grow 100 nm particles resulted in low-quality particles, as shown in **Figures 2.1a and 2.1c**. However, adding a third growing step that involves utilizing the 40 nm particles as seeds to produce particles with diameters in the range of 65-70 nm (**Figure 2.1b**) and then using these new particles as seeds leads to an improved quality of Au NPs with diameters of 100 nm (**Figure 2.1d**).

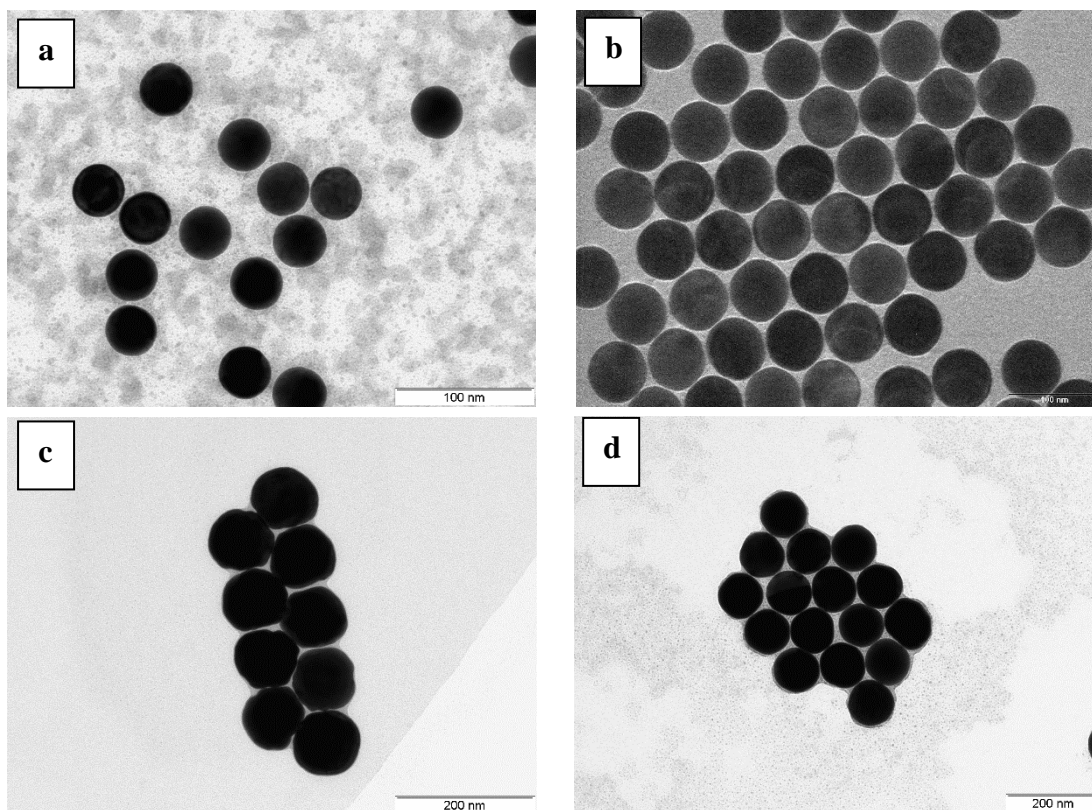
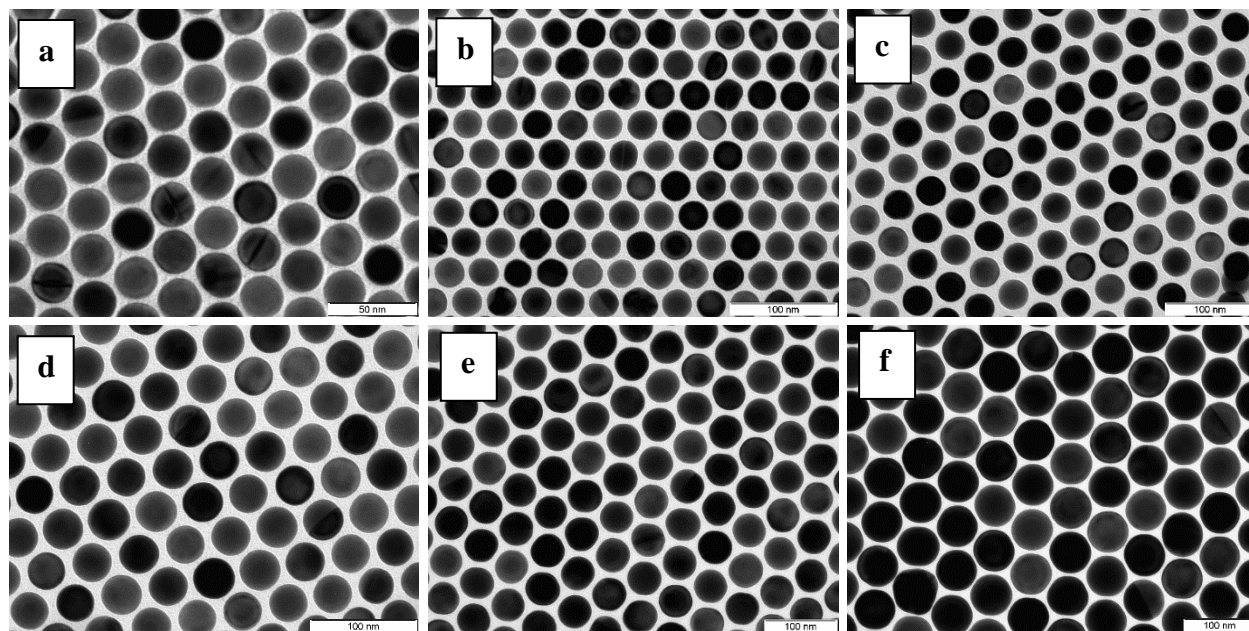


Figure 2.1. Transmission electron microscopy (TEM) micrographs of Au NPs with core diameters of (a) 40 nm and (b) 70 nm were used as seeds to synthesize Au NPs with diameters of 100 nm, showing bad (c) and good (d) particle quality.

2.3.2 Surface Functionalization of Au NPs

The Au NPs were functionalized with polystyrene thiol (PSSH) ligands and dispersed in toluene to stabilize and promote the self-assembly of large Au NP supercrystals. According to previous

results in our group¹⁰⁶, it was clear in some cases that there was a correlation between Au NP size and the length of the polymer coating, which resulted in better stability for the generation of supercrystals. Therefore, we have selected specific polymer ligand lengths for each particle size; for example, 2kPSSH for particles with diameters up to 35 nm, 5kPSSH for particles with diameters up to 45 nm, and 12kPSSH for Au NPs with diameters up to 135 nm. Transmission electron microscopy (TEM) images depict the 2D supercrystals made of PSSH-functionalized Au NPs with diameters in the range of 25-130 nm that are assembled into a hexagonally close-packed monolayer (**Figure 2.2**). The gap sizes between NPs were calculated based on the TEM micrographs (**Table 2**). The 2D supercrystals formed here are continuous. This means that the interstitial tetrahedral void spaces in the hexagonal lattices are filled with polymer. This can suggest that the PSSH ligands can be considered to act as soft ligands rather than hard shells¹⁰⁹. It is important to note that the gaps between the Au NPs with diameters above 70 nm are smaller than 2 nm. Sometimes, it was observed that the particles with a diameter above 100 nm appeared to be touching each other (**Figures 2.2i and 2.2j**). Thus, the gaps of larger particles need to be carefully determined. The absorbance spectra of the Au NPs after being functionalized with PSSH and re-dispersed in toluene are shown in **Figure 2.2i**. It can be clearly seen that there is red-shifting of the plasmon with increasing the diameter of the Au NPs.



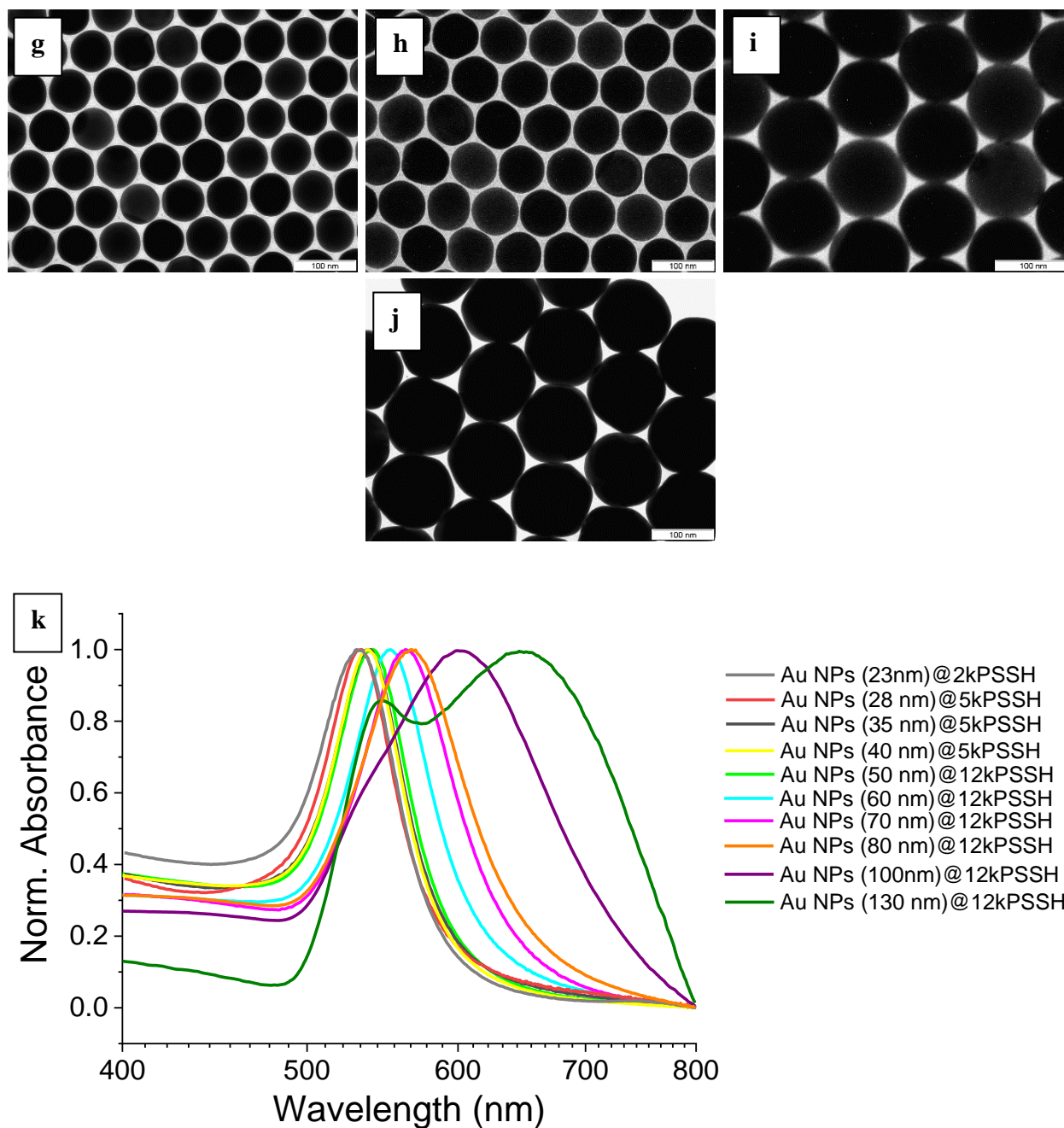


Figure 2.2. (a-g) Transmission electron microscopy (TEM) images of self-assembled Au NPs@PSSH monolayers some of which were used as building blocks for the generation of supercrystals. Au NPs with diameters of (a) $24.8 \text{ nm} \pm 0.43 \text{ nm}$, (b) $29.2 \text{ nm} \pm 0.43 \text{ nm}$, (c) $36.8 \text{ nm} \pm 0.6 \text{ nm}$, (d) $44.4 \text{ nm} \pm 0.73 \text{ nm}$, (e) $50.3 \text{ nm} \pm 0.3 \text{ nm}$, (f) $60.3 \text{ nm} \pm 0.5 \text{ nm}$, (g) $60.3 \text{ nm} \pm 0.5 \text{ nm}$, (h) $80 \text{ nm} \pm 2 \text{ nm}$, (i) $106 \pm 1.6 \text{ nm}$ and (j) $130.2 \text{ nm} \pm 3.6 \text{ nm}$ previously functionalized with 2kPSSH, 5kPSSH, 5kPSSH, 5kPSSH, 12kPSSH, 12kPSSH, 12kPSSH, 12kPSSH, and 12kPSSH, respectively. (k) Normalized absorbance spectra of the corresponding Au NPs after being functionalized with PSSH and re-dispersed in toluene.

2.3.3 Self-assembly of long-range Au NP supercrystals

The formation of Au NP supercrystals was performed in a liquid subphase using diethylene glycol (DEG) ^{103, 107}, as seen in **Figure 2.3**. Briefly, a concentrated solution of Au NPs dispersed in toluene is carefully pipetted onto the surface of DEG. As the toluene slowly evaporates, the concentration of Au NPs increases and starts to form the supercrystals. The process took approximately 24 hours until the toluene was completely evaporated. Once the solvent is evaporated, a gold film appears on the surface of DEG (Photograph, **Figure 2.3**). Ultimately, the film can be easily transferred to the desired substrate of choice (silicon substrate, glass slides, or a carbon-coated TEM grid). This method has been used for the generation of different 2D and 3D supercrystals ^{110, 111}. Au NPs with different core diameters were selected in this thesis, along with specific ligand coatings tailored to each size, in order to investigate the formation of long-range supercrystals. Specifically, Au NPs with core diameters of 28 nm, 40 nm, and 50 nm were functionalized with 2kPSSH, 5kPSSH, and 5KPSSH, respectively, while sizes of 50 nm, 70 nm, 80 nm, 100 nm, and 130 nm were coated with 12kPSSH.

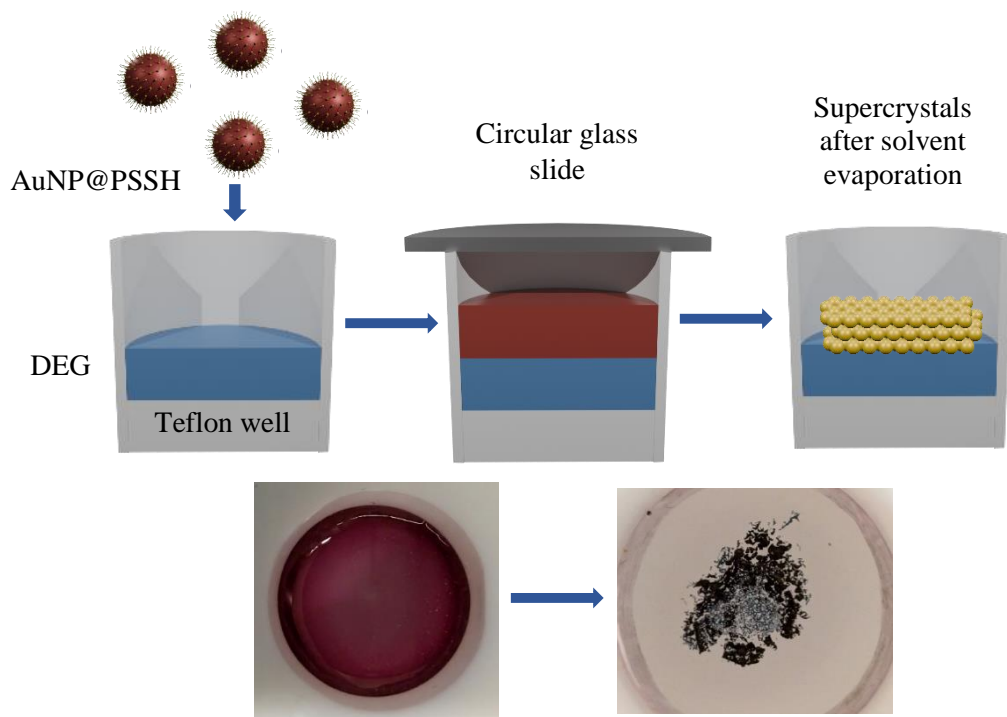
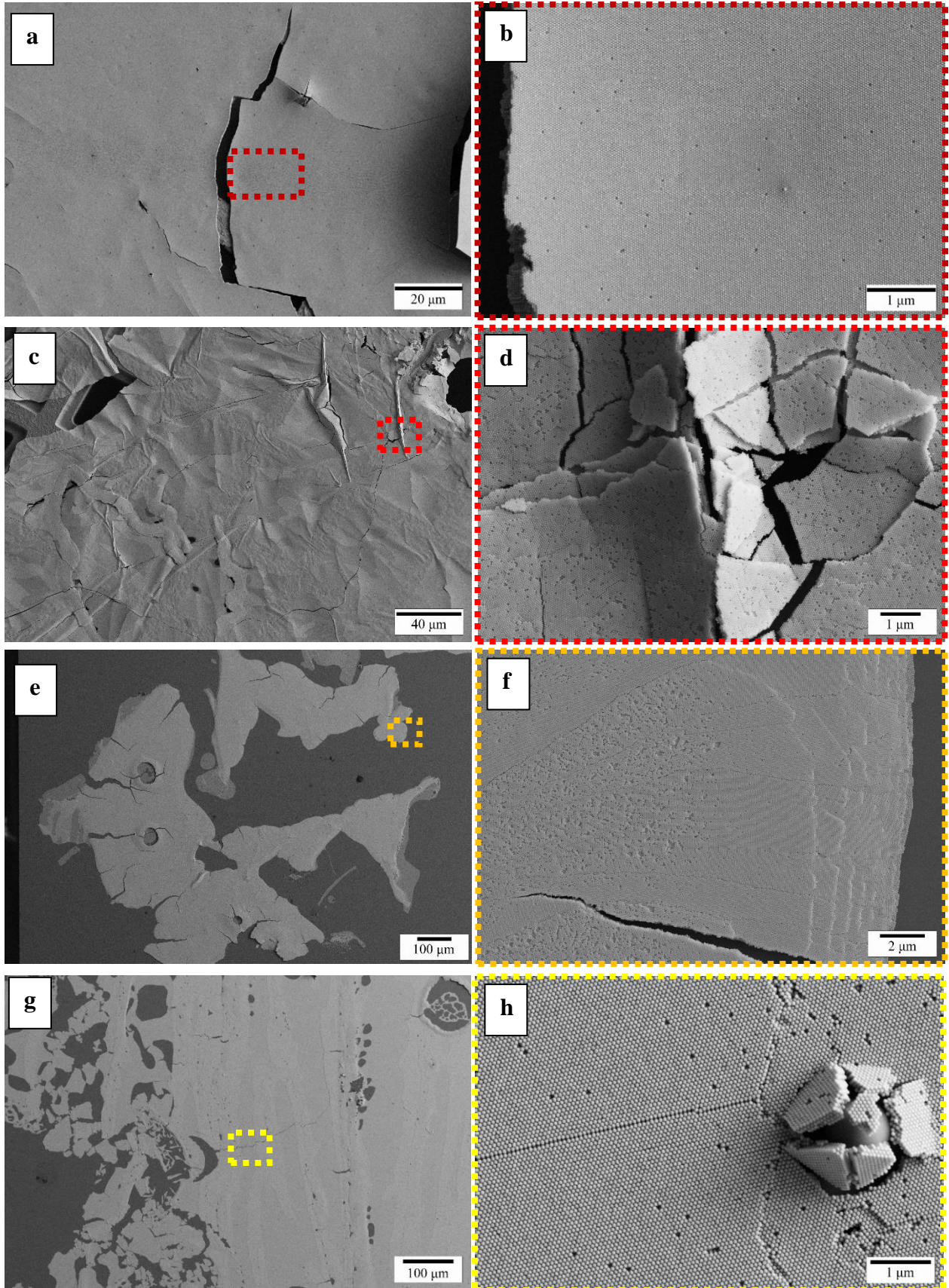


Figure 2.3. Schematic illustration of the Au NPs@PSSH supercrystals growth. The photograph shows a typical Au NP solution on the surface of DEG into a Teflon well, followed by supercrystals forming after toluene evaporation.

High-resolution scanning electron microscopy (SEM) micrographs were carefully analyzed to characterize the morphology and length of the self-assembled supercrystals. An overview of the different supercrystals self-assembled from Au NPs (28 nm)@5kPSSH, Au NPs (40 nm)@5kPSSH, Au NPs (50 nm)@12kPSSH, Au NPs (70 nm)@12kPSSH, Au NPs (80 nm)@12kPSSH, Au NPs (100 nm)@12kPSSH, Au NPs (130 nm)@12kPSSH is shown in **Figure 2.4**. Supercrystals self-assembled from Au NPs with diameters smaller than 70 nm exhibit well-ordered and long-range structures, showing excellent uniformity and homogeneity, as shown in **Figures 2.4a, 2.4b, and 2.4c**. High-magnification SEM images show that the supercrystals vary in the number of layers from a few layers to more than 10 layers, measuring several micrometers in size, and showing minimal local defects (**Figures 2.4b, 2.4d, and 2.4f**). On the other hand, the self-assembly of Au NPs with diameters larger than 70 nm leads to the formation of long-range supercrystals with high uniformity across several hundred micrometers, as shown in **Figures 2.4g-m**. Furthermore, high-magnification SEM shows supercrystals with high quality and uniformity self-assembled from Au NPs (70 nm)@12kPSSH and Au NPs (80 nm)@12kPSSH. However, supercrystals self-assembled from 100 nm and 130 nm presented more crystal defects (**Figures 2.4l and 2.4m**). However, they can still form large supercrystals that are several micrometers in length. The Au NP concentrations used for self-assembly of the supercrystals are summarized in **Table 2.1**.

As mentioned in the Introduction, creating supercrystals with specific characteristics, such as crystal quality and thickness control, is essential for future technological applications. The quality of supercrystals is crucial for the development and control of new collective properties. Until now, the majority of Au NP supercrystals discussed in the literature have focused on 2D supercrystals consisting of NPs with diameters smaller than 30 nm, and only a few with diameters of 80 nm¹⁰⁶. This is because it is difficult to synthesize high-quality supercrystals with larger NPs that also have a long-range order. For example, supercrystals made of particles larger than 80 nm can offer stronger light-matter coupling^{112, 107}. Thus, these results can significantly contribute to the design of large supercrystals with high uniformity and long-range order. Another important parameter to consider in the design of supercrystals is the impact of particle concentration on the formation of supercrystals¹⁰⁴. This will be discussed in the next section.



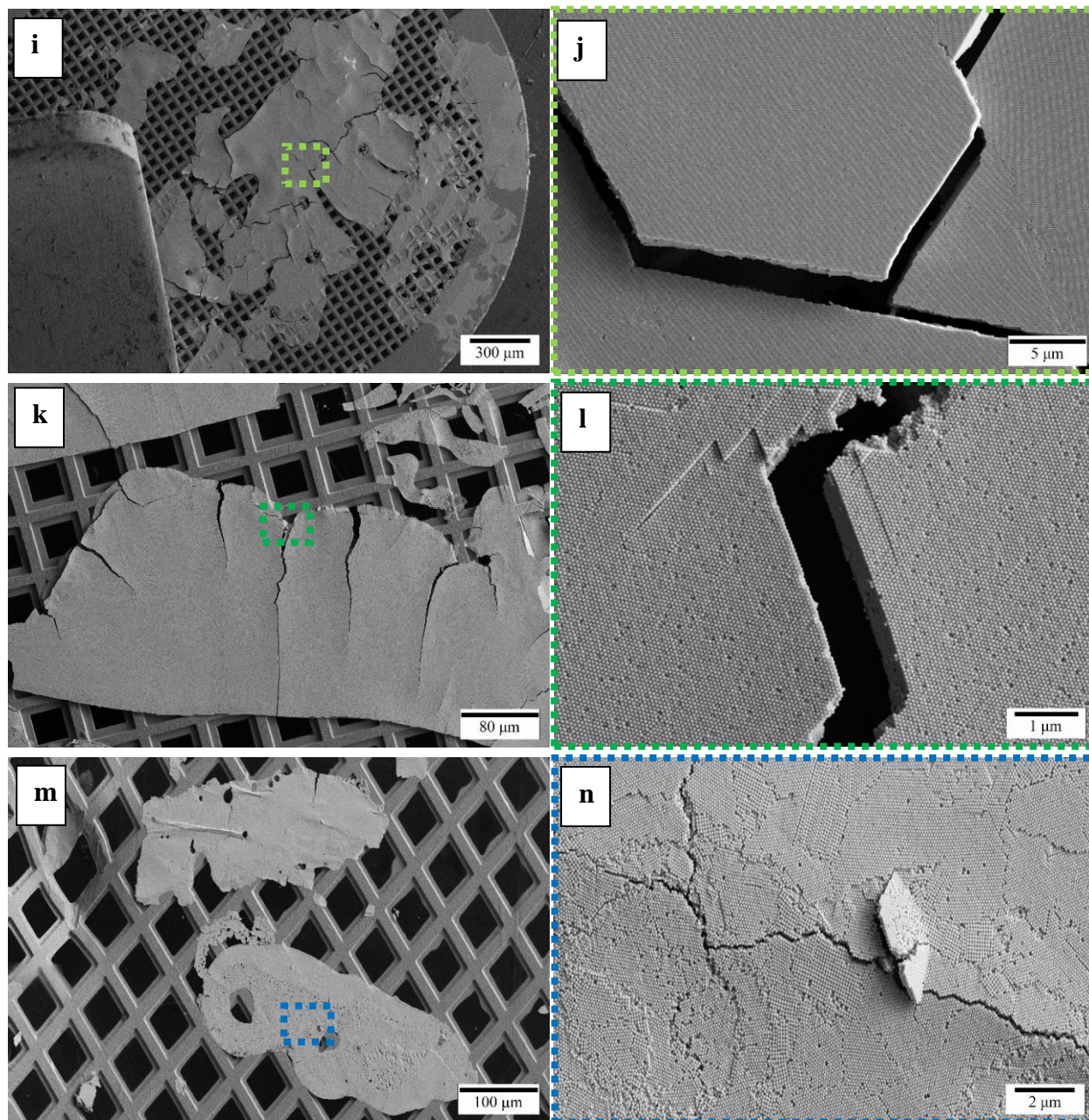


Figure 2.4. Scanning electron microscopy (SEM) micrographs of Au NP supercrystals which were assembled using different diameters of Au NPs. High-magnification SEM images (left) of supercrystals self-assembled from Au NPs (28 nm)@5kPSSH, Au NPs (40 nm)@5kPSSH, Au NPs (70 nm)@12kPSSH, Au NPs (80 nm)@12kPSSH, Au NPs (28 nm)@12kPSSH, Au NPs (100 nm)@12kPSSH, and Au NPs (130 nm)@12kPSSH. Low-magnification SEM images (right) of the corresponding supercrystals.

2.4 Growth Modes of Au NP supercrystals

The concentration of Au NPs used as building blocks is another crucial factor in the self-assembly of supercrystals^{103, 104}. Thus, to investigate this impact, PSSH-functionalized Au NPs with varying core diameters and two different concentrations were selected for self-assembling supercrystals. Au NPs with core diameters of 28 nm, 40 nm, 80 nm, and 130 nm were functionalized with 12kPSSH, 5kPSSH, 12kPSSH, and 12kPSSH, respectively, and used as building blocks for the formation of supercrystals. The concentrations of Au NP used for the formation of supercrystals self-assembled from Au NPs@PSSH are provided in **Table 2.3**.

For Au NPs (28 nm)@12kPSSH at low concentrations, the major product was the formation of well-ordered, long-range supercrystals with monolayers, bilayers, and multiple layers with minimal defects (**Figure 2.5a**), spanning several micrometers (**Figure 2.5b**). In contrast, high concentrations of Au NPs resulted in two different crystal growth modes: long-range layers and single crystalline island growths coexisting (**Figures 2.5c and 2.5e**). The excellent uniformity and crystallinity of these modes are shown in **Figure 2.5e**.

A similar behavior was observed when self-assembling supercrystals with Au NPs (40 nm)@5kPSSH. Low concentration produced long-range supercrystals with few defects and with more than 10 layers, as shown in low-magnification (**Figure 2.6a**) and high-magnification SEM (**Figure 2.6b**) micrographs. These supercrystals display good uniformity and crystallinity over a hundred micrometers. Conversely, when using high concentrations of Au NPs, low-magnification SEM images show extended and uniform supercrystals (**Figure 2.6c**). A closer examination corroborated the long-range uniform and almost defect-free supercrystal (**Figure 2.6d**). Interestingly, a second growth mode, island growth, was also observed (**Figure 2.6e**). A closer examination of the high-magnification SEM image unveiled the generation of micrometer-sized crystalline islands with high uniformity and almost free of defects (**Figure 2.6f**).

For larger Au NPs, low-magnification (**Figure 2.7a**) and high-magnification (**Figure 2.7b**) SEM images show that Au NPs (70 nm)@12kPSSH at low concentration formed long-range, well-ordered supercrystals. Interestingly, a high concentration of Au NPs resulted in long-range and well-ordered supercrystals (**Figure 2.7c**), with layers up to 26 (**Figure 2.7d**). These supercrystals display excellent uniformity and homogeneity across several micrometers. Interestingly, it was

also observed that large areas with polycrystalline island growth modes were also generated (**Figures 2.7e and 2.7f**), contrasting with the single-crystalline islands found in samples with smaller Au NPs diameters.

Finally, long-range supercrystals formed through the self-assembly of Au NPs (130 nm)@12kPSSH were observed at low concentrations (**Figure 2.8a**). The supercrystals extended for several hundred micrometers. High-magnification SEM images show that these Au NPs (130 nm)@12kPSSH yielded large crystalline layers with up to 3 layers (**Figure 2.8b**). On the other hand, high concentrations of Au NPs (130 nm)@12kPSSH resulted in long-range supercrystals measuring hundreds of micrometers (**Figure 2.8c**). An increase in the number of layers up to 8 layers with high crystallinity is shown in **Figure 2.8d**. In these experiments, the island growth mode was not observed. This could be attributed to the fact that there is less material compared to using small particles, as well as the dominant forces in the system, including van-der-Waals (vdW), slower diffusion, and gravitational forces^{113, 114}.

In summary, this behavior is interesting, since in principle, increasing the concentration of the Au NPs should lead to thicker homogeneous supercrystals. In this context, Mishra et al.¹¹⁵, have shown the formation of different growth modes, layered and islands modes, in superlattice thin films of NPs. Highlighting the importance of the solvent, evaporation time, and the interaction of the NPs with the substrate. More experiments should be done to fully understand and control the different growth modes of these supercrystals.

Table 2.3 Au NP concentrations used for the formation of supercrystals with monolayers up to several layers.

Sample	Au NP diameters (nm)	Polymer ligand	Low concentration (nM)	High concentration (nM)
Au NPs (28 nm)@5kPSSH	28	2kPSSH	~2.2	~4.4
Au NPs (40 nm)@12kPSSH	35	5kPSSH	~3.5	~7
Au NPs (70 nm)@5kPSSH	40	12kPSSH	~0.22	~0.44
Au NPs (135 nm)@12kPSSH	50	12kPSSH	~0.141	~0.282

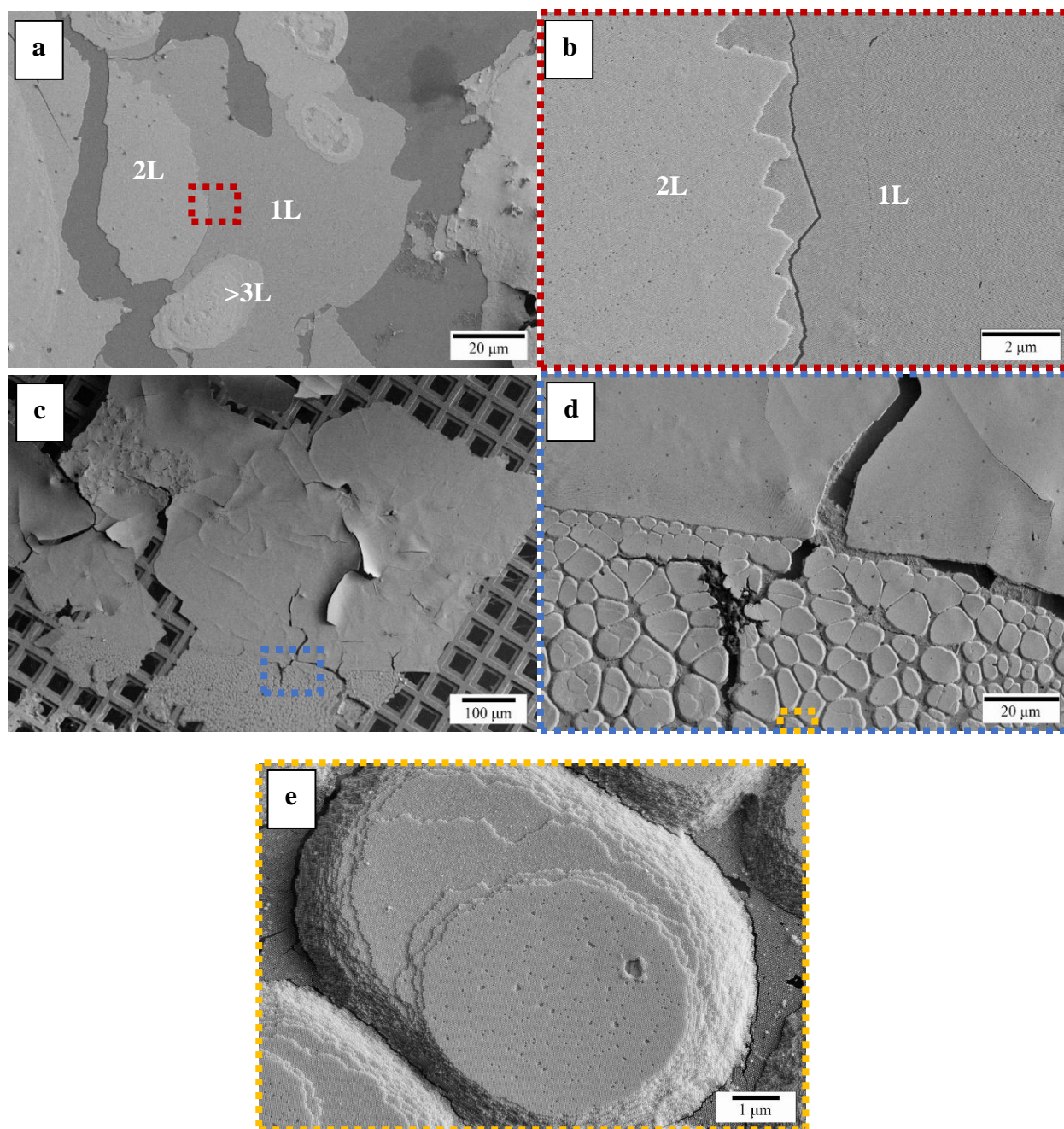


Figure 2.5. SEM images of AuNP supercrystals self-assembled from Au NPs (28nm)@12kPSSH at different concentrations. The left images (a) and (b) show low-magnification SEM images of the self-assembled supercrystals at low (a) and high (b) concentrations. The right images (b) and (d) show high-magnification SEM images of the outlined square in the images (a) and (c), respectively. Image (e) shows high-magnification SEM images of the outlined square in the image (d).

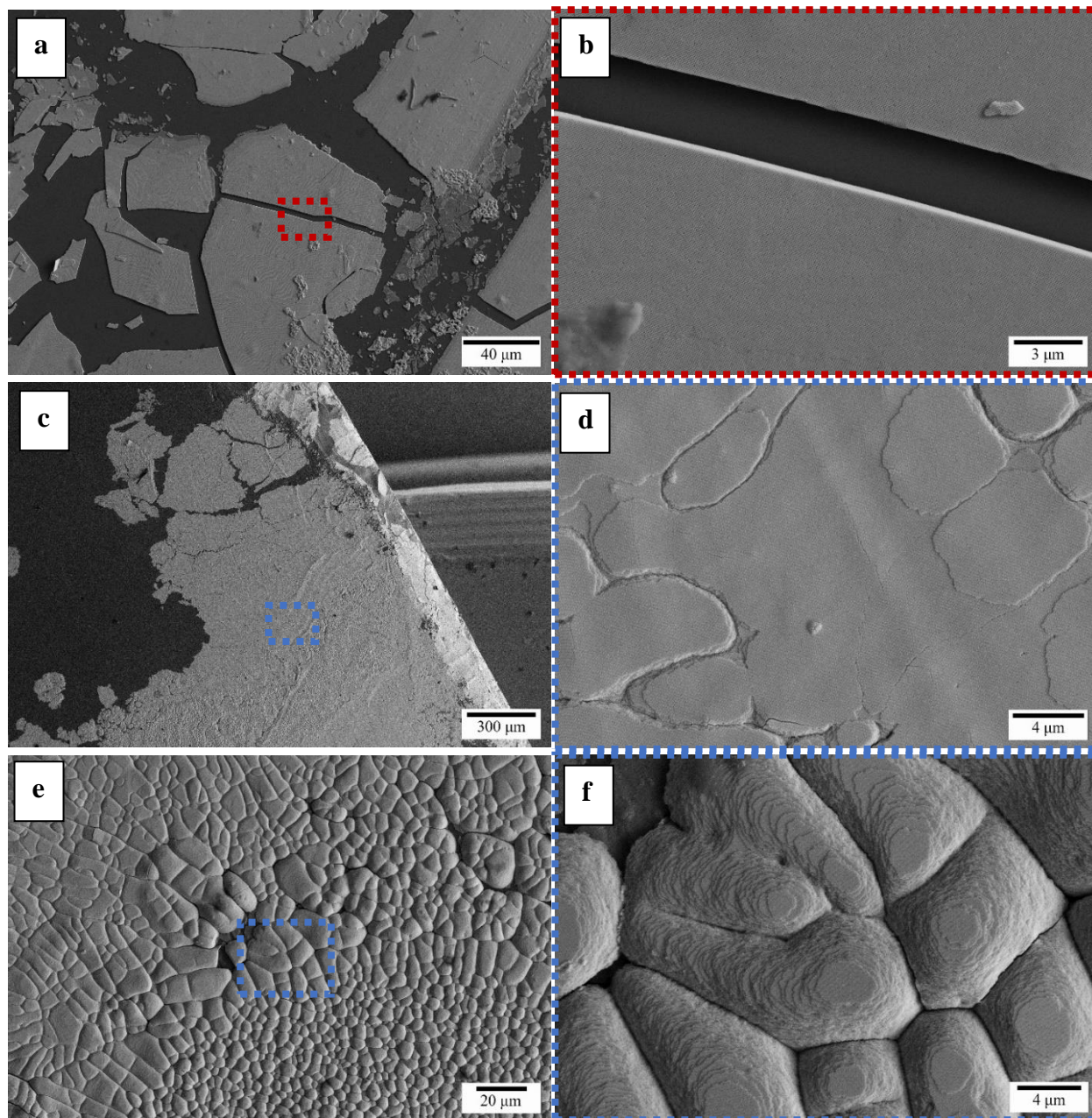


Figure 2.6. SEM images of AuNP supercrystals self-assembled from AuNPs (40 nm)@12kPSSH at different concentrations. The left images (a and c) show low-magnification SEM images of the self-assembled supercrystals at low (a) and high (c) concentrations. The right images (b and d, f) show high-magnification SEM images of the outlined square in the images (a) and (c, e), respectively

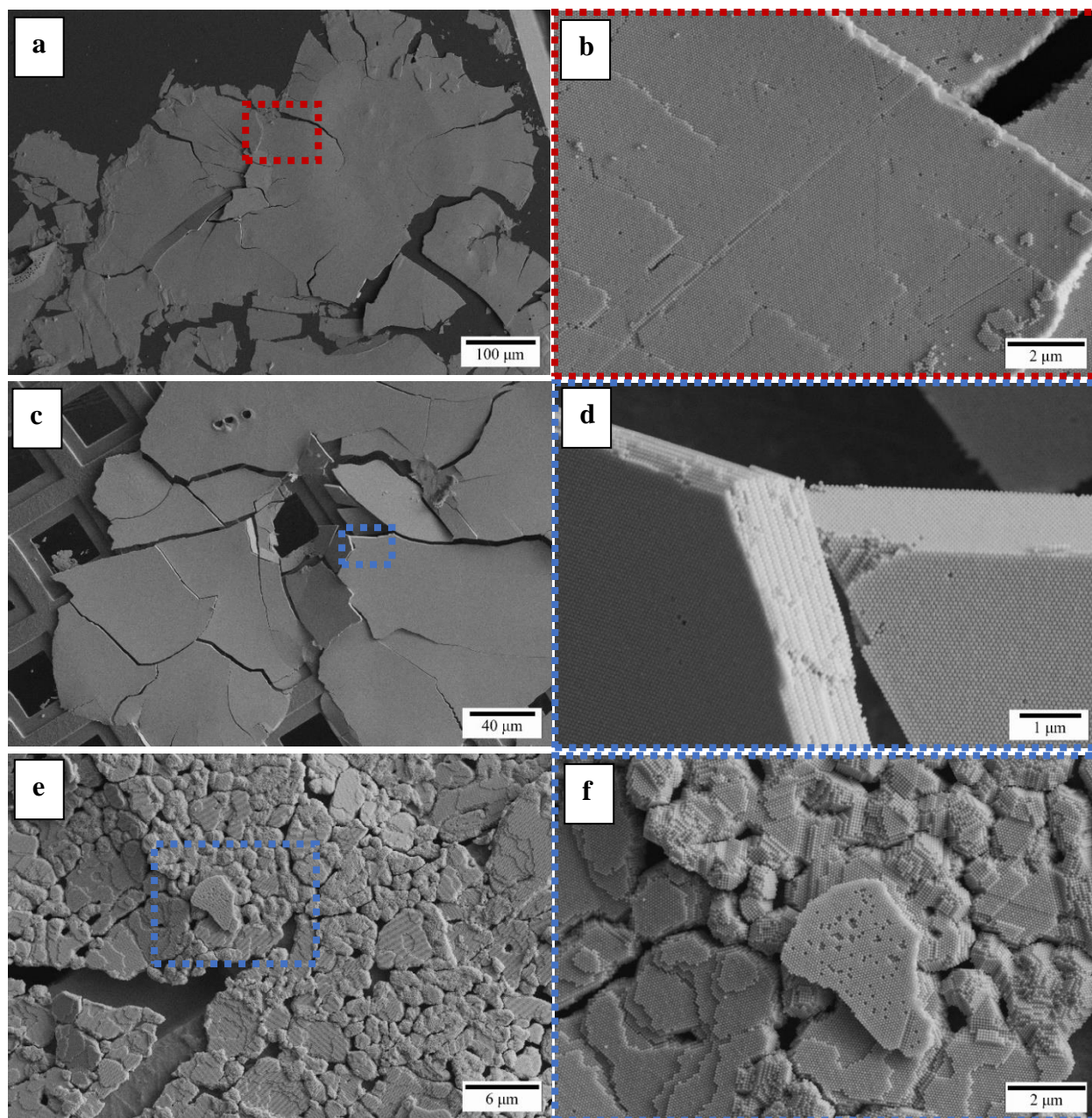


Figure 2.7. SEM images of AuNP supercrystals self-assembled from Au NPs (70 nm)@12kPSSH at different concentrations. The left images (a-e) show low-magnification SEM images of the self-assembled supercrystals at low (a) and high (c, e) concentrations. The right images (b) and (d, f) show high-magnification SEM images of the outlined square in the images (a) and (c, e), respectively.

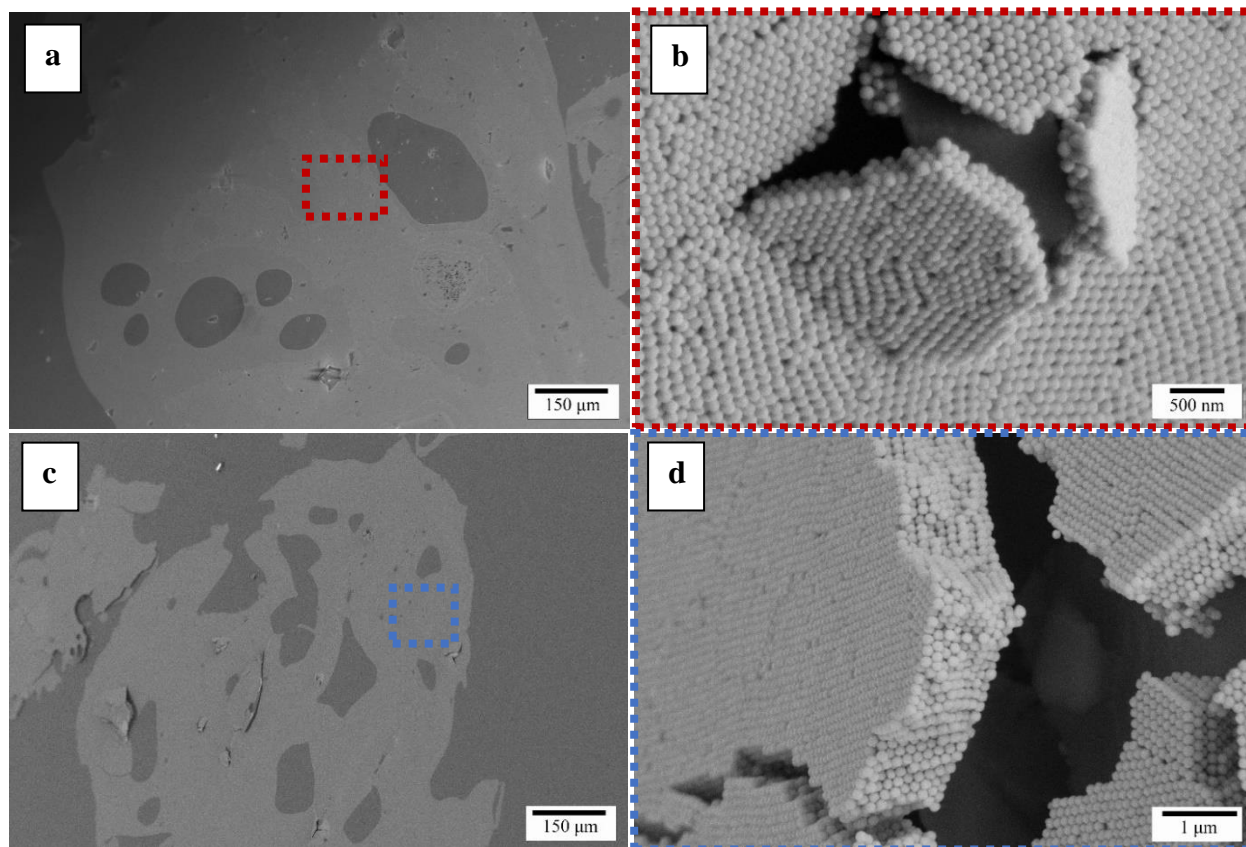


Figure 2.8. SEM images of AuNP supercrystals self-assembled from Au NPs (135 nm)@12kPSSH at different concentrations. The left images (a and c) show low-magnification SEM images of the self-assembled supercrystals at low (a) and high (c) concentrations. The right images (b) and (d) show high-magnification SEM images of the outlined squares in the images (a) and (c), respectively.

It will be necessary more experiments to understand the self-assembly of these growing modes, as they can be influenced by the evaporation rate of the solvent, temperature, and atmospheric pressure conditions. For example, using these new parameters with techniques such as small-angle X-ray scattering ¹¹⁶ or in situ liquid Transmission Electron Microscopy (TEM) ^{117, 118} could lead to a better understanding of these growth modes. Furthermore, gaining knowledge of the process that governs the self-assembly of Au NPs into supercrystals with well-defined and fine control over length and thicknesses is a crucially important step toward the fabrication of novel materials with specific optical properties ¹¹⁹.

2.5 Phase transition in 3D supercrystals

A closer examination of the SEM images of supercrystals composed of Au NPs with diameters larger than 70 nm revealed the coexistence of two distinct supercrystal domains: cubic closed-packed and hexagonal closed-packed domains (**Figure 2.9**). Low-magnification SEM images show long-range supercrystals with high uniformity and sizes of several hundreds of micrometers (**Figures 2.9a, 2.9c, 2.9e, and 2.9g**). On the other hand, high-magnification SEM images reveal the coexistence of cubic-close packed and hexagonal-close packed domains (**Figures 2.9b, 2.9d, 2.9f, and 2.9h**). The cubic crystal domains, with several micrometers in size, were surrounded by hexagonal domains in all experiments. Importantly, these experiments occurred when all large particles were coated with 12kPSSH. The differences in the crystal phases of the supercrystals composed of smaller NPs vs larger NPs could be attributed to the polymer ligand length used for Au NPs stabilization. As previously stated, Au NPs with diameters larger than 70 nm typically tend to be close to each other, and in some cases, the polymer coating made it not possible to measure the space between them, suggesting that these large polymers (12kPSSH) do not provide sufficient stabilization for large NPs. However, a thorough analysis of over 40 supercrystals composed of Au NPs with diameters under 70 nm revealed that two crystal domains were not present inside the supercrystals. These results provide compelling evidence for the significant contribution of polymer ligands to Au NP stabilization in the formation and determination of the crystal structure of supercrystals.

In this context, this phase transition behavior was observed in the self-assembly of PbS supercrystals by Bian et al., who found that by changing the solvent vapor conditions, the supercrystals could switch between the fcc, bcc, and bcc crystal domains ¹²⁰. The same group demonstrated that this phase can be also modulated by changing the ligand and the effective core size of the NPs ¹²¹. Highlighting, the important role of the balance between ligand-ligand interaction. Furthermore, previous experimental observations have shown a similar pattern. For instance, Daryl et al. ¹²², have shown that by manipulating the solvent quality and temperature, it was possible to alter the crystal phases in 3D supercrystals composed of polymer-grafted NPs, transitioning from FCC to BCC and vice versa. The main trigger for this phase transition was the collapse of the polymer ligands during these different parameters.

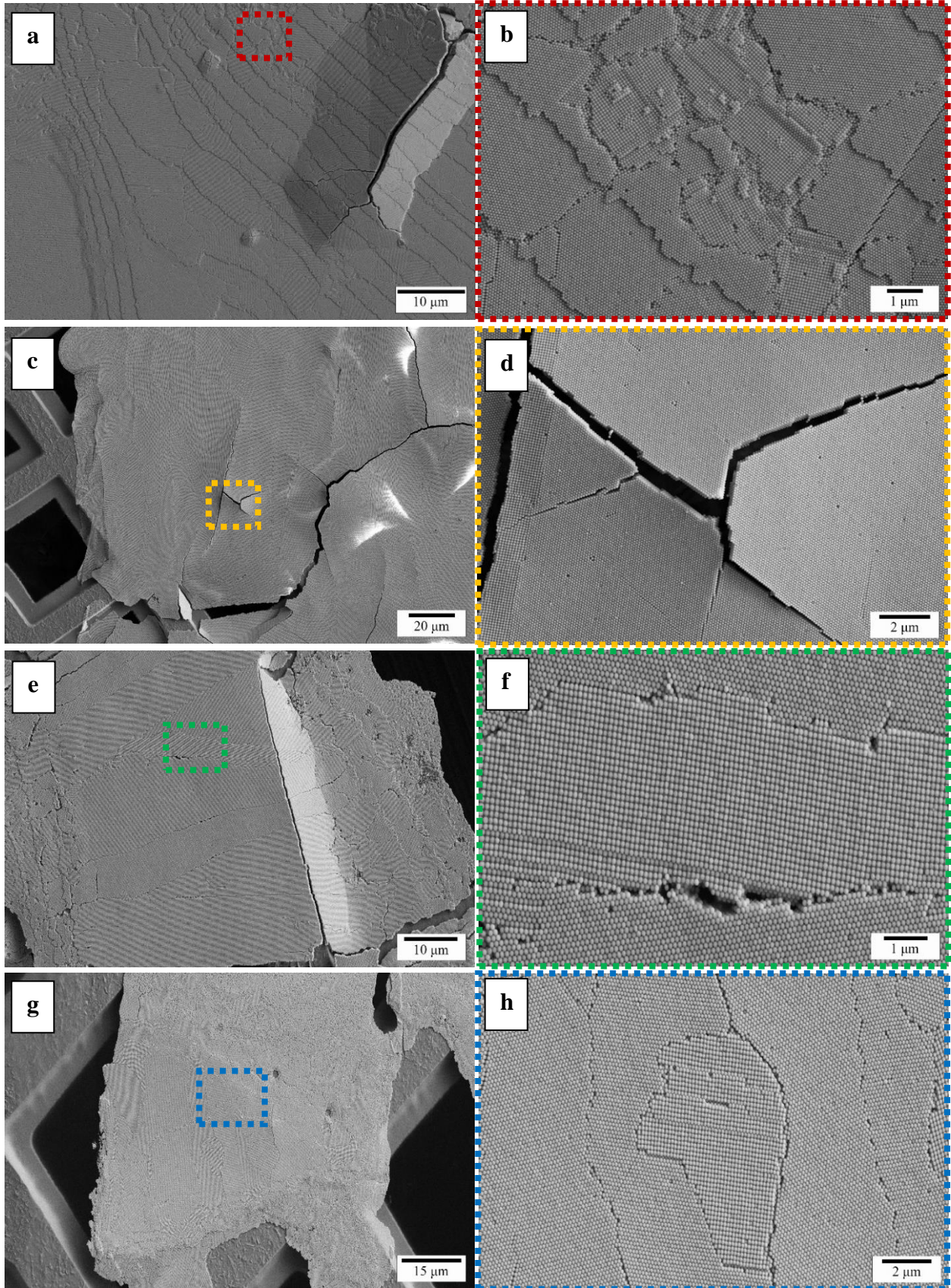


Figure 2.9. SEM images of AuNP supercrystals self-assembled from Au NPs@PSSH. The left images show high magnification SEM images of supercrystals self-assembled from Au NPs (80 nm)@12kPSSH (a), Au NPs (100 nm)@12kPSSH (c), Au NPs (105 nm)@12kPSSH (e), and Au NPs (130 nm)@12kPSSH (g). The right images (b), (d), (f), and (h) show high-magnification SEM images of the outlined square in the images (a), (d), (e), and (g), respectively, which exhibit the coexistence of cubic-closed packed and hexagonal-closed packed domains.

Taken together, these results, the SEM data suggest that phase transition is highly dependent on the polymer coating. Thus, the polymer ligands appear to be the primary cause of these phase changes in self-assembled supercrystals of larger Au NPs. To test this hypothesis, Au NPs with a diameter of 80 nm were selected and functionalized with 5kPSSH and 12kPSSH ligands and self-assembled into supercrystals. **Figure 2.10** depicts a comparison of two supercrystals self-assembled from AuNP80@5kPSSH and AuNP80@12kPSSH, analyzed by SEM. **Figures 2.10a and 2.10b** show high-magnification SEM images of long-range and highly uniform supercrystals, with several micrometers in size. **Figures 2.10c and 2.10d** show high-magnification SEM images of the corresponding **Figures 2.10a and 2.10b** outlined in squares. Two different crystal arrangements were observed: cubic-close packed for NPs coated with 5kPSSH, and hexagonal-close packed for NPs coated with 12kPSSH. The Fast Fourier Transform (FFT) of the corresponding images (**Figures 2.10e and 2.10f**) confirmed the quality and crystal domains of the supercrystals. These results strongly support the crucial role of the ligand coating in controlling these phase transitions. It is possible to suggest that the cubic-closed packed structure is initially favored owing to the presence of solvent molecules within the superlattices, which fill the voids between the neighboring NPs. However, further experiments should be conducted to fully understand the phase transition process in these supercrystals.

The fact that the phase transition only occurs with particles larger than 70 nm suggests that the large polymer ligand (12kPSSH) did not completely stabilize the larger Au NPs, in contrast to the small particles, thus modifying the thermodynamics that control the lattice stability and cause two distinct crystal phases in the supercrystals. It is important to highlight that these findings can be utilized to tune the internal structure of supercrystals, as demonstrated in the last experiments. A precise control over the spatial arrangement of these crystal phases can lead to the tunability of

their optical properties. In addition, a higher degree of symmetry and micrometer size could lead to the emergence of additional coupling modes^{104, 107}.

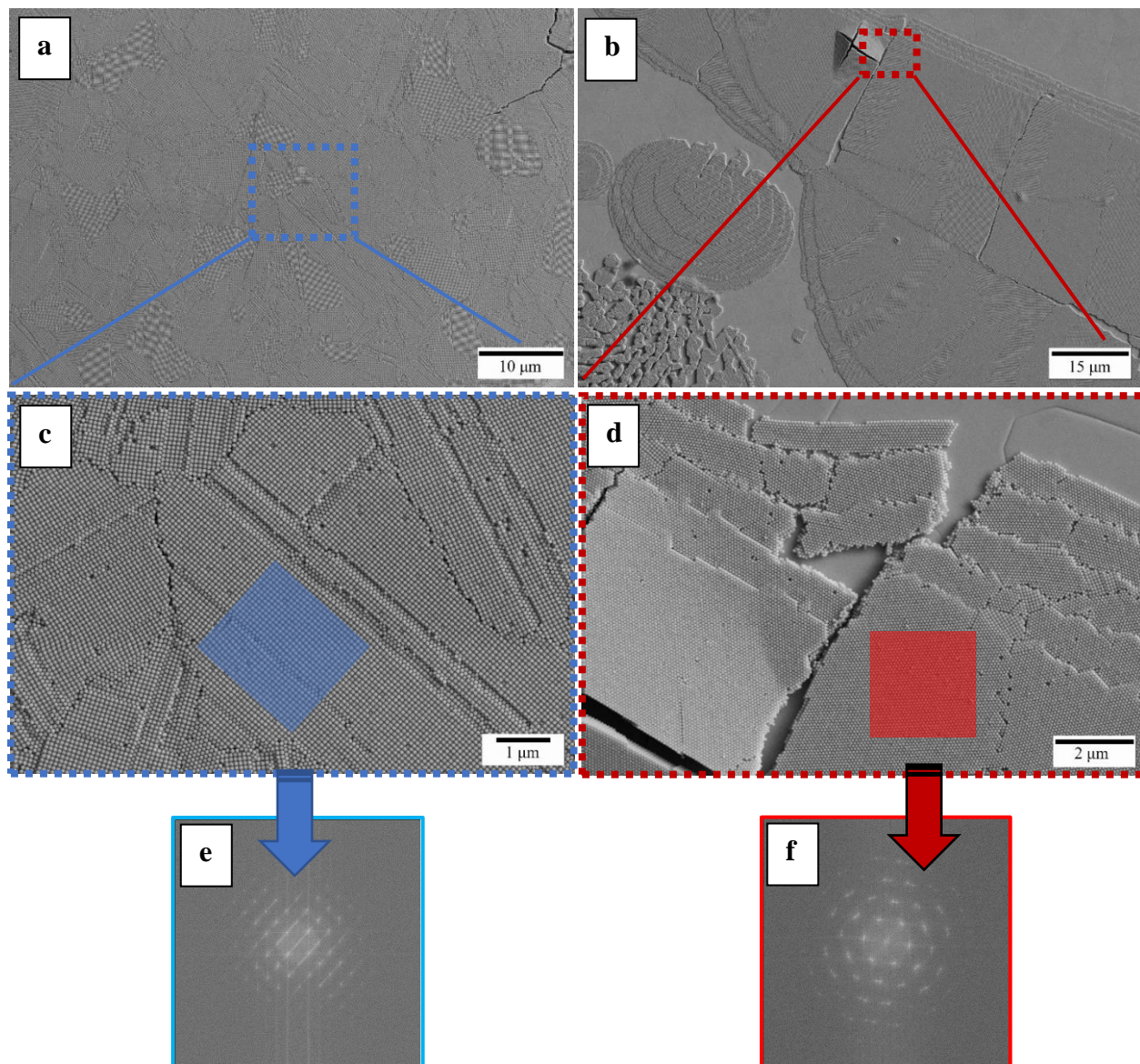


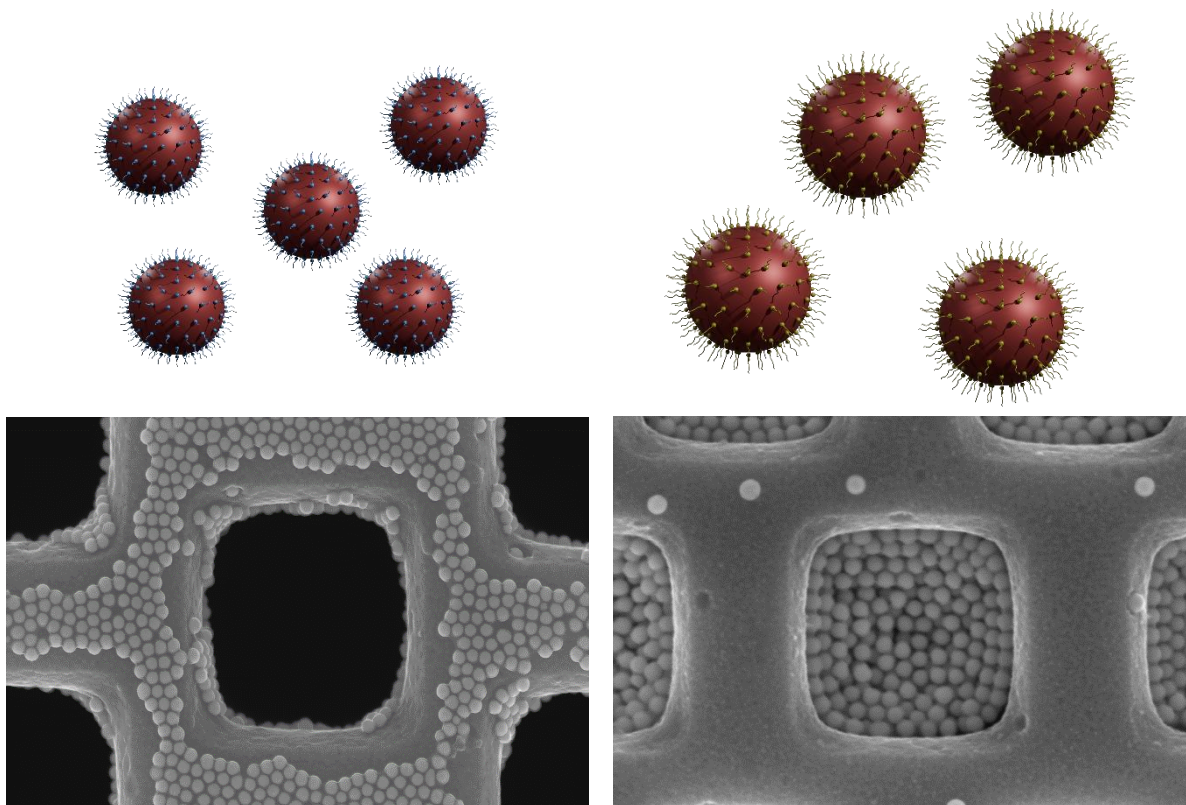
Figure 2.10. SEM images of AuNP supercrystals self-assembled from Au NPs@PSSH. The top images show high-magnification SEM images of supercrystals self-assembled from Au NPs (80 nm)@5kPSSH (a) and Au NPs (80 nm)@12kPSSH (b). The bottom middle images (c) and (d) show high-magnification SEM images of the outlined squares in the images (a) and (b), respectively. (e) and (f) images show FFT patterns corresponding to cubic-closed packed and hexagonal-closed packed domains of the selected areas in figures (c) and (d), respectively.

2.6 Conclusion

In conclusion, we successfully synthesized high-quality Au NPs with diameters in the range 25-130 nm, and with high concentrations. These particles were used as building blocks for the synthesis of long-range 2D and 3D supercrystals with extended micrometer-scale areas. The self-assembly of these supercrystals was optimized by screening different parameters, such as surface chemistry, particle size, and concentration. In particular, the concentration of Au NPs plays an important role in the thickness of supercrystals. Furthermore, at high concentrations of Au NPs with diameters smaller than 70 nm, the coexistence of two growth modes was observed in the supercrystals: layered growth and island growth. Finally, the coexistence of cubic and hexagonal lattices in supercrystals consisting of Au NPs with core diameters larger than 70 nm is especially significant in this Thesis. In this regard, it was observed that the ligand coating played an important role in this phase transition. For example, using Au NPs (80 nm) functionalized with 12kPSSH resulted in hexagonal close-packed supercrystals, while modifying the ligand coating to a short ligand (5kPSSH) resulted in a change in the crystal lattice to a cubic close-packed structure. The unique adjustability of the present Au NPs supercrystals, good uniformity and homogeneity along several micrometers as well as their simple transfer to various substrates make these supercrystals a promising option for a variety of applications, such as photonics, catalysis, and surface-enhanced Raman spectroscopy.

CHAPTER III

3 Incorporation of highly ordered PSSH-functionalized Au NPs into 2D and 3D arrays within and on the pores of porous silicon membranes



3.1 Introduction

3.1.1 Porous Silicon

Since its first demonstration of room-temperature visible photoluminescence three decades ago, porous silicon (pSi) has received significant attention in the research community¹²³. These emitting properties have shown tunability by changing the pore size and morphology of the pore¹²⁴.

pSi can be easily synthesized by electrochemical etching. Briefly, a voltage is applied between the anode and the cathode. The silicon wafer acts as the anode and is placed in contact with an electrolyte consisting of a solution of hydrofluoric acid (HF). The cathode, which is immersed in

the electrolyte, typically consists of a platinum wire with a spiral or circular shape. By modifying the concentration of the electrolyte and voltage, it is possible to control the pore size, porosity, and pore thickness^{124, 125, 126}. Figure 1 shows an example of different pSi samples prepared at different etching conditions.

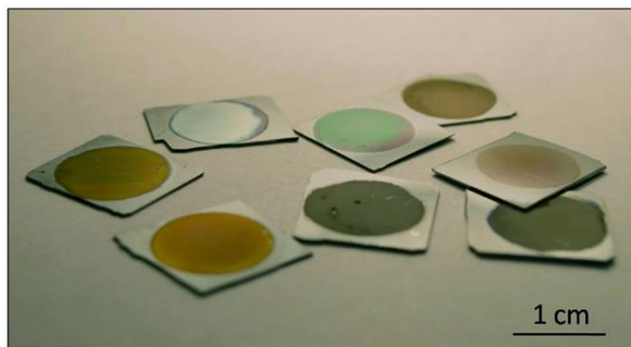


Figure 3.1. Photograph of various pSi samples prepared at different etching conditions¹²⁷.

An alternative way to create porous silicon (pSi) is through the photo-electrochemical etching method. This method is significant for industrial purposes as it allows for the large-scale production of pSi membranes by etching both N-type and P-type silicon in an HF solution. It follows a similar process to electrochemical etching but involves the use of illumination during the process^{128, 129}. This method enables the production of thin films of pSi with pores in the micron size range, controllable porosity, and different thicknesses^{130, 131, 132, 133}.

According to the International Union of Pure and Applied Chemistry (IUPAC) guidelines, depending on the pore size, pSi can be classified into three categories: microporous (2 nm), mesoporous (2 nm < d < 50 nm), and macroporous (d > 50 nm)^{134, 135}. This last one, macroporous silicon, is one of the most used ones due to the evenness of the pore walls and the consistent diameter along the entire pore depth^{136, 137}.

In general, due to its exceptional properties, such as high surface area, refractive index modulation, high resistance, and tunability, as well as its easy and versatile synthesis, pSi is a potential candidate for various applications¹³⁸. For instance, it can be utilized in biosensors for the detection of molecules in complex media¹³⁹, as well as gas sensors for the detection of hazardous chemicals¹⁴⁰. Additionally, pSi can be used as a host material for generating hybrid materials, a research area of active investigation in recent years.

3.1.2 Porous silicon as a host material

Thanks to its versatility regarding pore size and fine control over porosity and thickness, pSi can be used as a template to fill its pores with one or more guest materials, which could result in a drastic change in the physical properties. For instance, it can be filled with metals or conductive polymers. In this context, the generation of pSi-based hybrid systems that incorporate plasmonic NPs aims to develop new materials with more advanced features.

Thanks to the extremely large internal surface area of pSi and their easy tunability regarding the pores, pSi offers great opportunities to fabricate hybrid systems. For example, pSi-based hybrid platforms that incorporate metal NPs could serve as SERS substrates due to the enhancement of Raman scattering^{141, 142, 143}.

pSi hybrid systems could be fabricated using various procedures including physical, physicochemical, chemical, and electrochemical techniques. However, two main methods are typically widely applied: direct NPs growth through an electrochemical process and incorporating pre-synthesized NPs¹⁴⁴. However, new methods to incorporate NPs within the pores of pSi membranes are necessary, since the actual methods cannot control the precise arrangement of the NPs, leading to agglomerations or producing a high polydispersity of NPs^{145, 146, 141}.

3.1.3 Surface-enhanced Raman spectroscopy (SERS)

Surface-enhanced Raman scattering, commonly called SERS, is a typical and highly sensing technique that enhances Raman scattering, a form of inelastic scattering, by molecules absorbed on the surface of nanostructured materials (NMs). This SERS relies on the use of NMs with nanoscale dimensions that show surface plasmon resonance (SPR), such as gold and silver³⁶. NMs such as NPs, corrugated films, or ordered arrays can enhance the Raman signal through the enhanced local fields that appear from surface plasmon resonance (SPR)^{147, 148, 149}. The confined regions where the local field enhancement occurs are called Hot spots and normally these regions can be enhanced by the coupling of nanostructures with controllable interparticle gaps^{148, 149, 150, 151}.

To date, the SERS technique has become an attractive and powerful technique and has found its place in a diverse range of technological applications that include environmental monitoring¹⁵²,¹⁵³, disease diagnosis¹⁵⁴, food quality control¹⁵⁵, bioanalytical chemistry¹⁵⁶, biomedicine¹⁴⁷, and photonics, among others.

3.1.4 Plasmonic gold nanoparticles

Plasmonic NPs have unique optical and electric properties due to their size, shape, and organization. The self-assembly of plasmonic NPs has been intensively researched for many years due to the significant variation in their properties compared to individual NPs. In particular, gold nanoparticles (AuNPs) have been extensively researched for their use in the self-assembly of long-range 2D and 3D ordered arrays, owing to their enhanced electronic, optical, and physical properties. These self-assemblies represent regions with enormously enhanced electric fields, known by the term “hot spots”, and can cause a significant improvement in the optical signal. Thus, future efforts will be focused on designing and developing cost-effective and sustainable supports for the achieved 2D and 3D arrays of Au NPs while preserving their plasmonic properties.

In summary, designing hybrid materials by using pSi membranes as a host material could lead to a generation of well-defined “hot spots” due to the incorporation of highly ordered Au NPs, presenting a promising approach for the development of new hybrid materials with collective plasmonic properties.

This chapter will cover a simple method for creating 2 hybrid systems by using porous silicon membranes as a host material for the self-assembly of highly ordered Au NPs into 2D and 3D arrays within and on the surface of their pores. By modifying parameters such as particle size, surface chemistry, and centrifugation force and time, two hybrid configurations can be obtained. Due to the high control and highly ordered structure achieved in both configurations and large covered areas, this hybrid configuration could be used as a SERS substrate. In this context, both hybrid configurations were tested as a SERS substrate by measuring the PSSH molecules embedded in the system. Interestingly, a consistent SERS signal was detected while evaluating the PSSH molecules at various locations on the pores of the substrate in both hybrid systems. The use of these hybrid systems could open new ways to engineer the collective plasmonic properties of

the Au NPs inside its pores and transfer them to technological applications such as SERS-active substrates, microelectronic and catalytic devices, biosensors, and others.

Parts of this chapter are based on the ideas published or submitted in the manuscript:

1. Engineered the self-assembly of plasmonic gold nanoparticles into 2D and 3D arrays within the pores of porous silicon membranes.
Juan J. Barrios Capuchino, Patrick Huber, Alexander Petrov, Wolfgang J. Parak, and Florian Schulz. *Manuscript*, 2024

3.2 Methods

Materials

Macroporous silicon membranes doped with phosphorus (n-type) were purchased from Smart Membranes GmbH (Germany). The membranes have a pore diameter of 1 μm and a pore pitch of 1.5 μm . The membranes were 5 x 5 mm in size and 0.05 mm in thickness. Tetrachloroauric (III) acid ($\geq 99.99\%$ trace metal basis), trisodium citrate dihydrate ($\geq 99.99\%$), ascorbic acid (AA, $\geq 99.99\%$), sodium borohydride (NaBH_4 , $\geq 98\%$), cetyltrimethylammonium bromide (CTAB, $\geq 99.99\%$), and cetyltrimethylammonium chloride (CTAC, 25 wt% in water) were ordered from Sigma-Aldrich. Toluene ($\geq 99.95\%$), tetrahydrofuran ($\geq 99.5\%$), and ethanol (denat., 96%), were from VWR (USA). The respective purities are given in brackets. Thiolated polystyrenes (PSSH, PSSH_{2k}: M_n : 2800 g mol⁻¹, PSSH_{5k}: M_n : 5300 g mol⁻¹, M_w = 5800 g mol⁻¹; PSSH_{12k}: M_n =5800 g mol⁻¹, M_w =12,400 g mol⁻¹) were purchased from Polymer Source (Canada). Ultrapure water (10.2 M Ω cm), Millipore) was used for all experiments. All reagents were used without any additional treatment. All the glassware used in the experiments was cleaned with fresh aqua regia and rinsed several times with MQ.

Synthesis of Au NPs of different sizes

Gold nanoparticles (Au NPs) with diameters of 50 nm and 70 nm were synthesized according to the seeded growth protocol presented by Zheng et al. with minor modifications and scaled up by a factor of 10 to achieve high AuNP concentrations. Briefly, for the preparation of the initial CTAB-stabilized seeds, sodium borohydride (NaBH_4 , 600 μL , 10 mM) was quickly added into a 10-mL

mixture of CTAB (5 mL, 200 mM) and Tetrachloroauric (III) acid (HAuCl₄, 5 mL, 0.5 mM) under rapid stirring (900 rpm). The final mixture remained undisturbed at 30°C for 3 h.

For the first growth step, aqueous solutions of AA (1.5 mL, 100 mM) and CTAC (2.0 mL, 200 mM) were mixed with 50 µL of the initial CTAB-seeds at 900 rpm, followed by one shot injection of HAuCl₄ (2 mL, 0.5 mM). The newly synthesized Au NPs were stirred at 900 rpm for 15 min. The AuNPs were collected by centrifugation (21,000 g, 30 min). These Au NPs were dispersed in CTAC (1 mL, 20 mM), used as seeds, and adjusted to ≈21 nM for growing larger Au NPs.

For the second growth to synthesize Au NPs@50nm, an aqueous solution of AA (1.3 mL, 10 mM) and CTAC (20 mL, 100 mM) was mixed with 120 µL of the previous AuNPs seeds at 600 rpm and treated with ultrasound for 1 min, afterward, followed by a dropwise injection of HAuCl₄ (20 mL, 0.5 mM). The Au NPs were washed two times via centrifugation (9,000 g, 30 min). The first washing step was with water and in the second washing step the particles were re-dispersed in 20 mM of CTAC for the next growing step.

For the third growth step to synthesize Au NPs@70nm, an aqueous solution of AA (1.3 mL, 10 mM) and CTAC (20 mL, 100 mM) was mixed with 300 µL of the previous AuNPs at 600 rpm and treated with ultrasound for 10 min, afterward, followed by a dropwise injection of HAuCl₄ (20 mL, 0.5 mM). The AuNPs were washed twice via centrifugation (5,000 g, 30 min) and re-dispersed in 1 mL of MQ.

Table 3.1 Parameters of Au NPs@CTAC seeds used for the synthesis of Au NPs@CTAC with diameters of 50 nm and 70 nm.

Sample	V _{seeds} (mL)	d _{seeds} (nm)	c _{seeds} (nM)
Au NPs (40 nm)@CTAC	0.3	11.5 nm	21 nM
Au NPs (50 nm)@CTAC	0.12	11.5 nm	21 nM

Surface ligand exchange of Au NPs

The direct ligand exchange of the Au NPs was performed based on the protocol presented by Dong et al.⁶⁵ and adapted from Schulz et al.¹⁰³. Briefly, the previously synthesized Au NPs were

centrifuged and concentrated in ~100 μ L and then added into a vigorously stirred (600 rpm) round flask that contained a solution of PSSH-ligands in THF (6ml, 1 mM). The reaction was left overnight. Then, the THF solution of Au NPs@PSSH was dried under a rotary evaporator, the film residue was filled with 1 mL of toluene and purified 3 times (7,000 g, 15 min) with a mixture of water and ethanol to remove excess PSSH and CTAC, and three more times with toluene. Finally, the Au NPs@PSSH were concentrated in 0.5 mL of toluene for further self-assembly experiments.

Table 3.2 Au NP samples used for the self-assembly experiments on the pores of porous silicon membranes.

Sample	Au NP diameter (nm)	Ligand	c(Au NP) (nM)
Au NPs (50 nm)@5kPSSH	50	11.5 nm	21 nM
Au NPs (50 nm)@12kPSSH	50	11.5 nm	21 nM
Au NPs (70 nm)@5kPSSH	70	11.5 nm	21 nM
Au NPs (70 nm)@12kPSSH	70	11.5 nm	21 nM

Standard procedure for the self-assembly of AuNPs within the pores of porous silicon membranes

The self-assembly of Au NPs within the pores of macroporous silicon membranes was performed by immersing the membranes in 20 μ L of a colloidal solution that contained the previous spherical Au NPs@PSSH with two different particle sizes ($d_c=50$ nm and 70nm) and PSSH length chains (PSSH5k and PSSH12k, respectively). Centrifugal force was applied to facilitate the incorporation of the AuNPs, providing an external force for the self-assembly of Au NPs within the pores. Thus, the membranes were left in the solution for 24 h and centrifuged at 2,000 g for 30 min. The membranes were removed from the solution and dried for 24 h at room temperature (RT). The pore filling of the membranes was improved by controlling different parameters such as AuNP size, surface ligand chemistry, centrifugation speed, and time. The sizes of substrates usually were tailored to ~2.3 x 2.3 mm².

Uv-Vis absorption spectroscopy

Absorbance measurements were carried out using a Cary Eclipse 60 Spectrometer. Quartz cuvettes (Hellma QS, Hellma, Germany) were used. The samples were prepared by diluting 50 times the previously functionalized particles. The Au NPs and Au NPs@PSSH concentrations were estimated with the absorbance at 450 nm as described by Haiss et al.²².

Morphological Characterization

Scanning electron microscopy (SEM) images were obtained using a Zeiss Sigma set-up operated at an accelerating voltage of 10 kV. To characterize the morphology and self-assembly distribution of the Au NPs in the pores of the pSi membranes, the previously impregnated substrates were directly deposited on a carbon tape. The cross-sectional images of the pSi-Au NPs hybrid platforms were performed by carefully cutting the membranes vertically with a glass cutter and depositing them directly on a carbon tape. High-resolution micrographs were obtained at a working distance of 2.7 mm and by using an InLens detector.

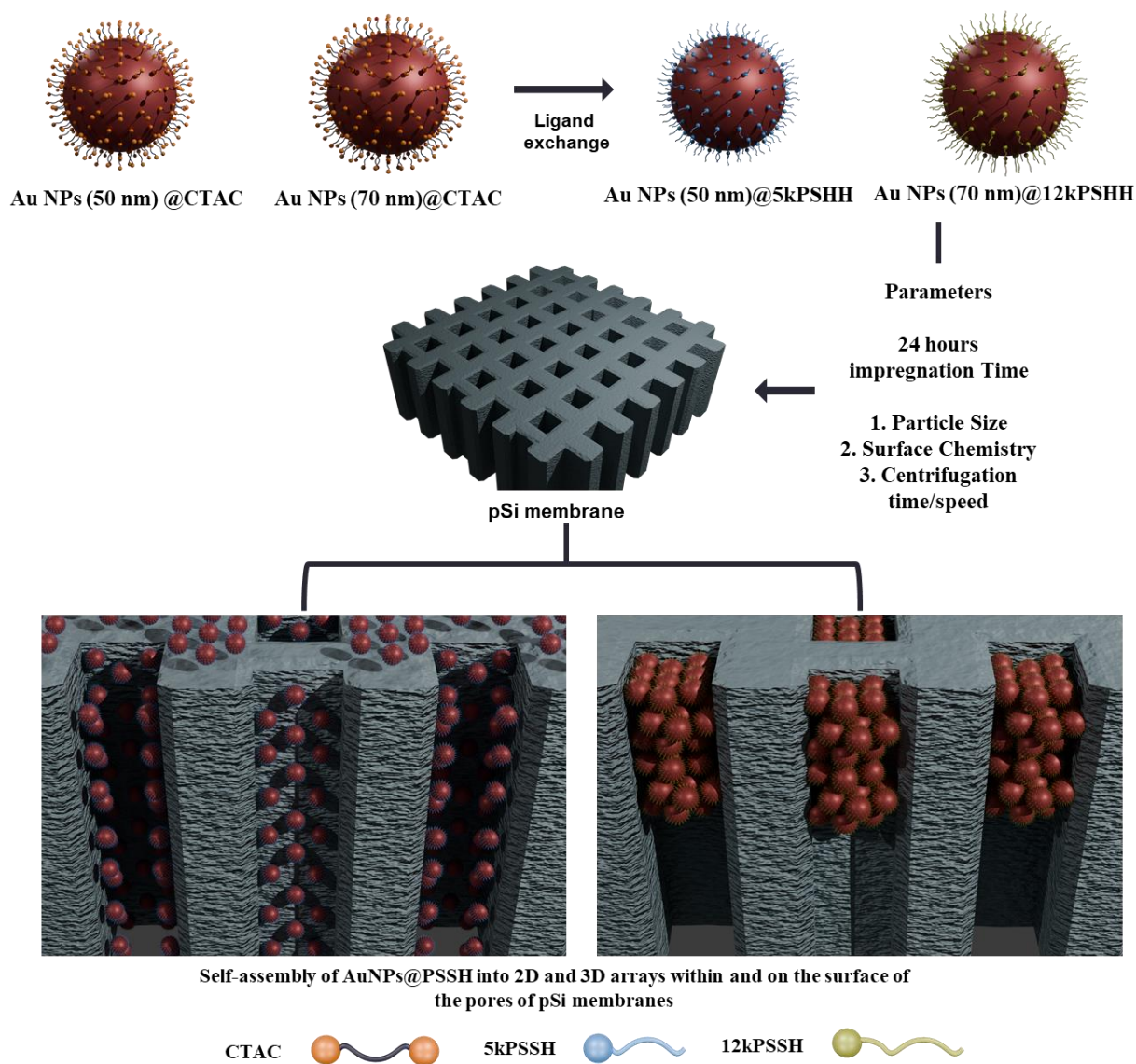
Transmission electron microscopy (TEM) micrographs of Au NPs@PSSH were performed on a JEOL JEM-1011 microscope with an operating voltage of 100kV. The TEM samples were prepared by dropping 8 μ L of PSSH-functionalized Au NPs onto a carbon-coated TEM grid. The particle sizes were manually calculated using the software Image J 1.53e from the TEM image.

Surface-enhanced Raman spectroscopy (SERS)

Raman spectroscopy was carried out using a Horiba Raman spectrometer with tunable excitation lasers for SERS measurements. A laser with a 785 nm wavelength was used as light source. The laser was focused with a 100x plan objective on the membrane surface. Wavenumbers ranging from 900 cm^{-1} to 1200 cm^{-1} were analyzed here. The spectra were recorded with a laser excitation power of 1600 μ W. To check the reproducibility, the SERS signals were collected from at least five different pores randomly distributed throughout each sample surface. All the experiments were performed at RT.

3.3 Results and Discussion

Scheme 3.1 shows a schematic illustration of the ideal process for self-assembling highly ordered Au NPS into two-dimensional (2D) and three-dimensional (3D) arrays within and on the pores of porous silicon membranes. By adjusting parameters such as particle size, surface chemistry as well as centrifugation speed and time, the self-assembly of Au NPs@PSSH within the pores of porous silicon (pSi) can be controlled



Scheme 3.1. An idealized schematic of the self-assembly of highly ordered Au NPs@PSSH into 2D and 3D arrays within and on the surface of the pores of pSi membranes.

The Au NPs used in this work were functionalized with thiol-terminated polystyrene (PSSH) molecules to help the stabilization of AuNPs and to promote their self-assembly¹⁰³. Transmission electron microscopy (TEM) shows the Au NPs@PSSH with core diameters of 50 nm and 70 nm, coated with 5kPSSH and 12kPSSH (**Figures 3.1a-d**). The particles look uniform and also exhibit a typical hexagonal close-packed array. The absorption spectra of these NPs are shown in **Figure 3.1f**. It is evident that there is a slight red shift of AuNPs@50nm and AuNPs@70nm after being coated with 5kPSSH and 12kPSSH ligands and transferred to toluene.

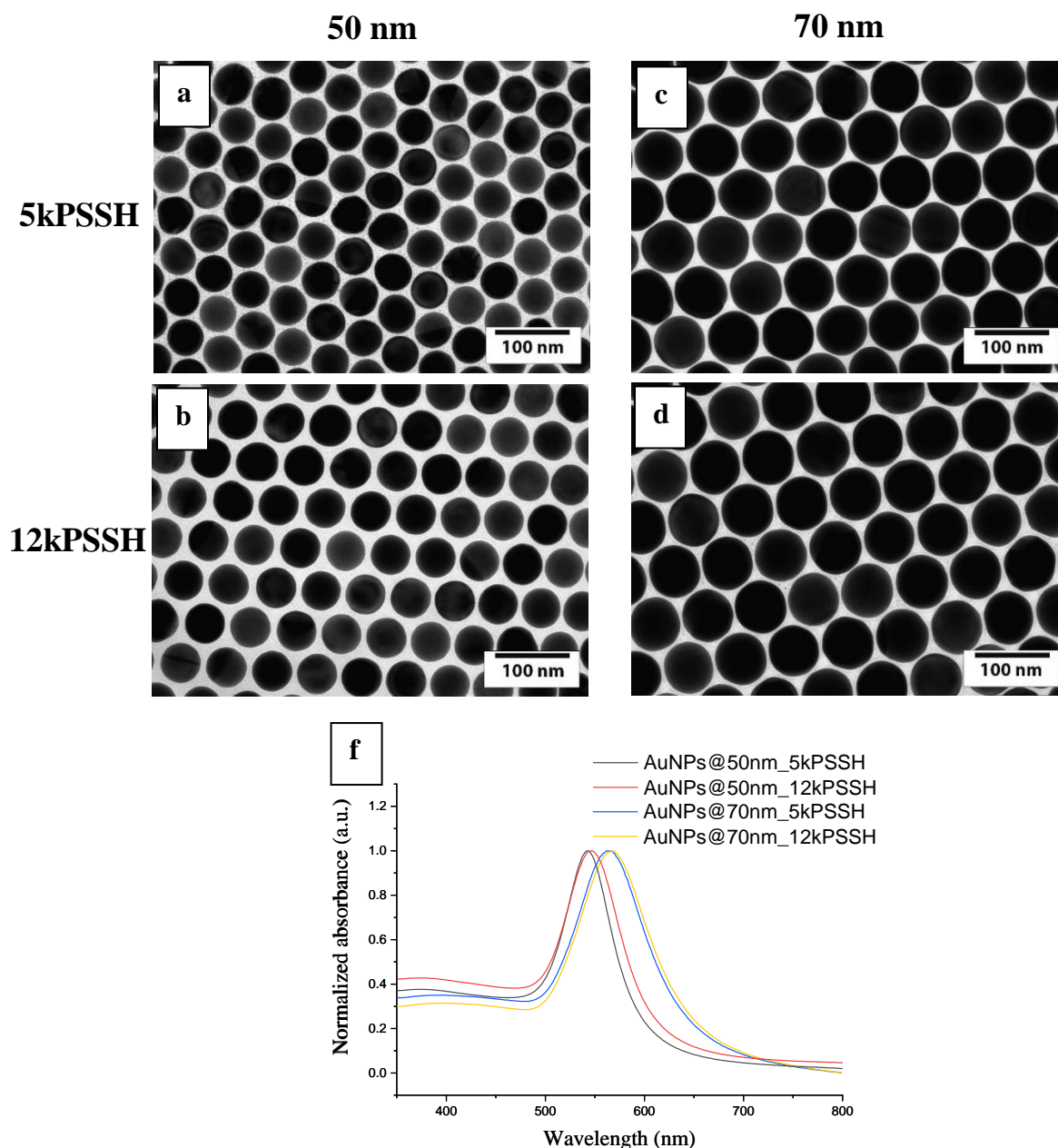


Figure 3.1. Transmission electron microscopy (TEM) images of self-assembled Au NPs@PSSH monolayers which were used as starting materials. Au NPs of different core diameters (50 and 70 nm) were coated with PSSH of different ligands (2k and 5kPSSH). Normalized absorbance spectra of Au NPs (50 nm and 70 nm) functionalize with 5KPSSH (dark and blue) and with 12KPSSH (red and yellow) in toluene.

Monocrystalline macroporous silicon membranes doped with phosphorus (n-type) were used as a hosting material to self-assemble highly ordered Au NPs@PSSH arrays. A high-resolution scanning electron microscopy (SEM) image of the pSi membranes depicts the characteristics of these membranes (**Figure 3.2a**). The pSi membranes display macropores arranged in a hexagonal structure with a pore diameter of 1 μm and a pore-to-pore distance of 1.5 μm . The membranes were carefully tailored to ~ 2.2 mm for the self-assembly experiments as shown in the photograph in **Figure 3,2b**.

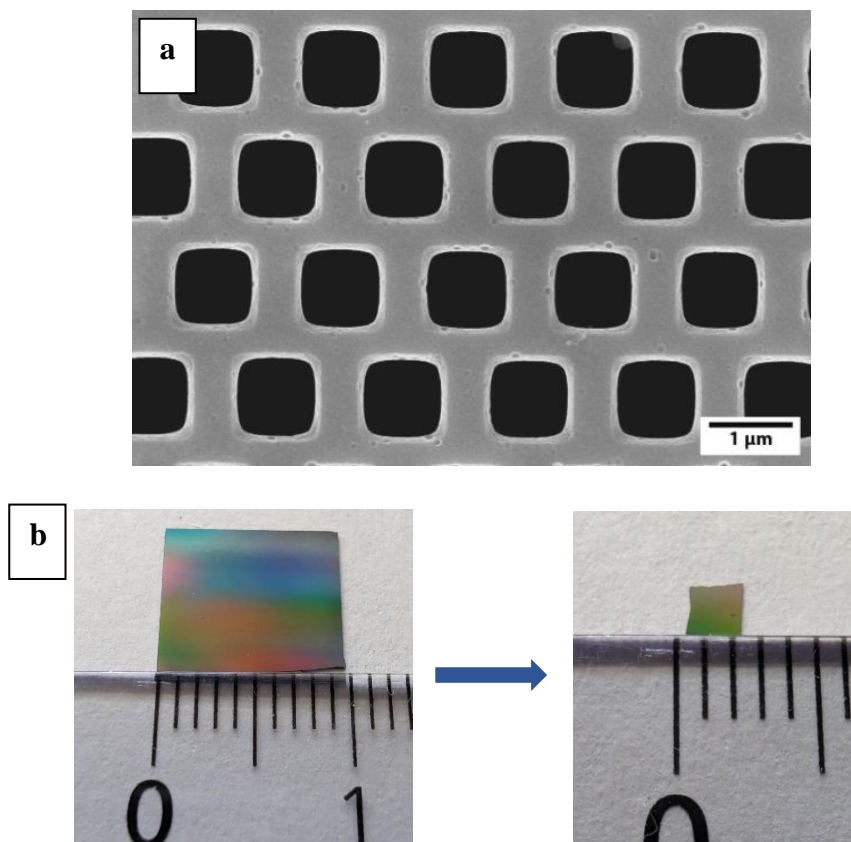


Figure 3.2. Scanning electron microscopy (SEM) image of pSi membrane which were used as starting materials. The photographs show the psi membranes before and after being tailored to a 2.3 x 2.3 mm² pSi membrane.

3.3.1 Morphology of the self-assembled Au NPs within the pores of porous silicon membranes

The self-assembly of the Au NPs@PSSH within the pores of pSi membranes was optimized by adjusting the size and surface chemistry of the Au NPs while keeping a constant particle concentration for all the experiments. The concentration parameters are displayed in **Table 3.2**. Initially, the pSi membranes were dipped in a solution that contained the Au NPs previously functionalized with PSSH. As the first combinations, Au NPs with core diameters of 50 and 70 nm were functionalized with 5kPSSH and 12kPSSH, respectively. As previously shown in Chapter 1, these particle size ranges can form large supercrystals with high uniformity and quality. The mixture was then left for 24 hours. The use of toluene as solvent shows promise in controlling and achieving large self-assembly of 2D and 3D crystals of Au NPs@PSSH^{103, 106}. Furthermore, studies have shown that toluene, along with 24 hours of impregnation time, aids in filling and leads to a more homogeneous deposition of Au NPs and FeCo NPs within the pores of pSi membranes¹⁵⁷. Finally, the addition of centrifugation at different times and speeds was proposed to improve the incorporation and self-assembly of the Au NPs@PSSH within the pores. This additional process could improve the infiltration and self-assembly of the Au NPs into the pores while preventing their agglomeration at the top of the surface.

High-resolution scanning electron microscopy (SEM) micrographs were examined to study the self-assembly of Au NPs (50 nm)@PSSH on the pores of pSi membranes. Centrifugation parameters were adjusted to 1,000 g for 30 min, 2,000 g for 30 min, and 2,000 g for 60 min. **Figures 3.3a, 3.3c, and 3.3e** show low-magnification SEM images of pSi membranes after interaction with Au NPs (50 nm)@PSSH. Large areas spanning hundreds of micrometers are decorated with NPs. High-magnification SEM images reveal the self-assembly arrangement of the Au NPs (50 nm)@PSSH on the surface of pSi membranes (**Figures 3.3b, 3.3d, and 3.3f**). Superior uniformity was observed under centrifugation conditions of 1,000 g for 30 min and 2,000 g for 30 min. On the other hand, the second particle size, Au NPs (70 nm)@12kPSSH, exhibited different self-assembly behavior under identical conditions (**Figure 3.4**). **Figures 3.4a, 3.4c, and 3.4e** present low-magnification SEM images of pSi after interaction with Au NPs@PSSH under the three centrifugation parameters. It is clear that NPs are incorporated inside pSi membrane pores in only one of the three centrifugation conditions. High-magnification SEM images demonstrate

improved organization of these NPs. For centrifugation conditions of 1,000 g for 30 min, and 2,000 g for 60 min, NPs are randomly dispersed on the surface and within the pores (Figures 4b and 4d). However, under the second centrifugation condition (2,000 g for 30 min), Au NPs (70 nm)@12kPSSH are incorporated within the pores of the pSi membranes (Figure 4f). These results strongly suggest that the centrifugation parameters play an important role in the self-assembly of Au NPs@PSSH in the pores of pSi membranes.

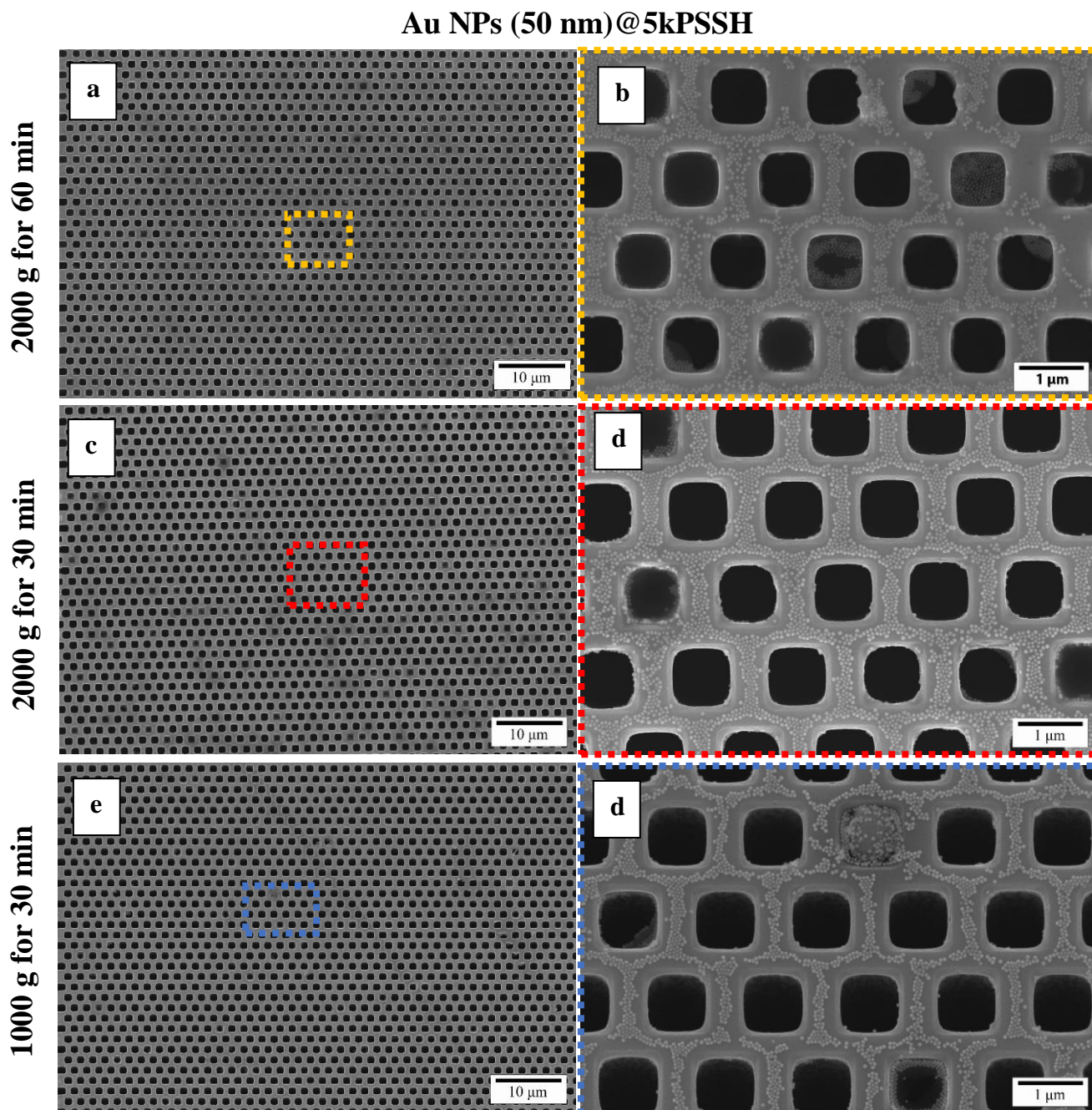


Figure 3.3. Scanning electron microscopy (SEM) images of porous silicon membranes after interaction with PSSH-functionalized Au NPs. Top view of porous silicon membranes after interacting with a) Au NPs (50 nm)@5kPSSH and b) Au NPs (70nm)@12kPSSH under several centrifugation parameters: 1,000 g for 30 min, 1,000 g for 30 min, and 1,000 g for 30 min.

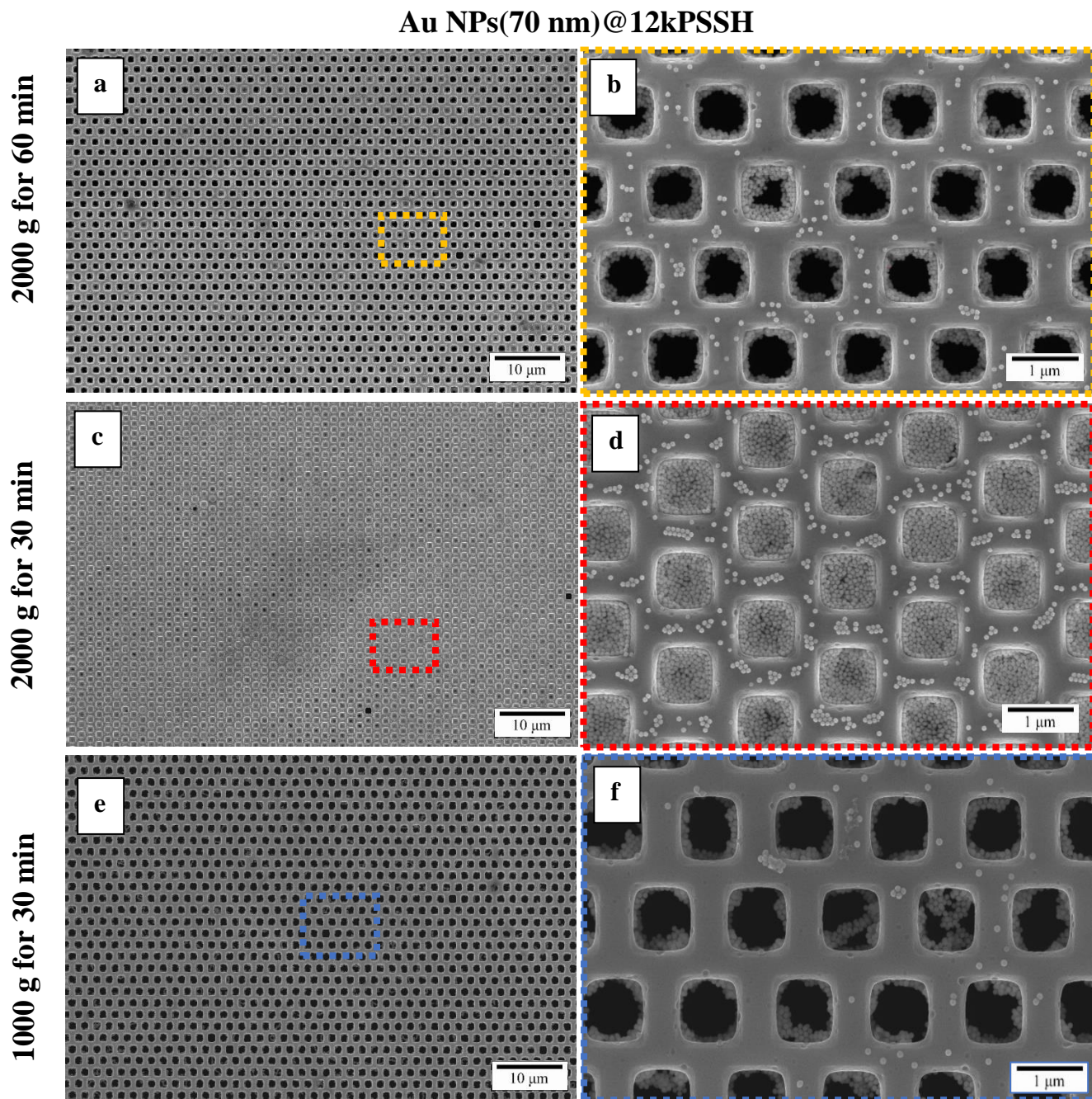


Figure 3.4. Scanning electron microscopy (SEM) images of porous silicon membranes after interaction with PSSH-functionalized Au NPs. Top view of porous silicon membranes after interacting with a) Au NPs

(50 nm)@5kPSSH and b) Au NPs (70nm)@12kPSSH under several centrifugation parameters: 1,000 g for 30 min, 1,000 g for 30 min, and 1,000 g for 30 min.

3.3.2 Arrangement of Au NPs within the pores of porous silicon membranes

To investigate the uniformity and the specific arrangement of the Au NPs@PSSH within the pores of the pSi membranes, high-resolution cross-sectional SEM images were analyzed. The cross-sectional SEM images of the hybrid system assembled using Au NPs (50 nm)@5kPSSH and Au NPs (70 nm)@12kPSSH revealed two distinct self-assembly configurations (**Figure 3.5**). Specifically, pSi-Au NPs (50 nm)@5kPSSH exhibited dense 2D arrays of Au NPs along the pSi membrane pore walls under only two of the three centrifugation parameter settings: 1,000 g for 30 min and 2,000 g for 30 min (**Figures 3.5c and 3.5e**), while the third one shows just randomly distributed Au NPs on the walls of the pores (**Figure 3.5a**). The high impregnation of the pores can be explained by improved NP flow through the pores due to the tuned centrifugal force, which effectively pushes the NPs against the pore walls. In contrast, Au NPs functionalized with 12kPSSH displayed 3D arrays, with self-assembly occurring near the pore surface and extending just a few micrometers into the pore opening membrane towards the center (**Figure 3.5a**). However, the 3D array was achieved just for one of the centrifugation parameters, 2000 g for 30 min, while for the next two centrifugation parameters just randomly NPs were found in the surface and pore walls of the pores (**Figure 3.5b and 3.5c**). This observation suggests that the 3D self-assembly process occurred predominantly within the pSi membrane pores, as illustrated in **Figure 3.5d**. Overall, the findings indicate that both the Au NP diameter and centrifugation parameters play crucial roles in the self-assembly process.

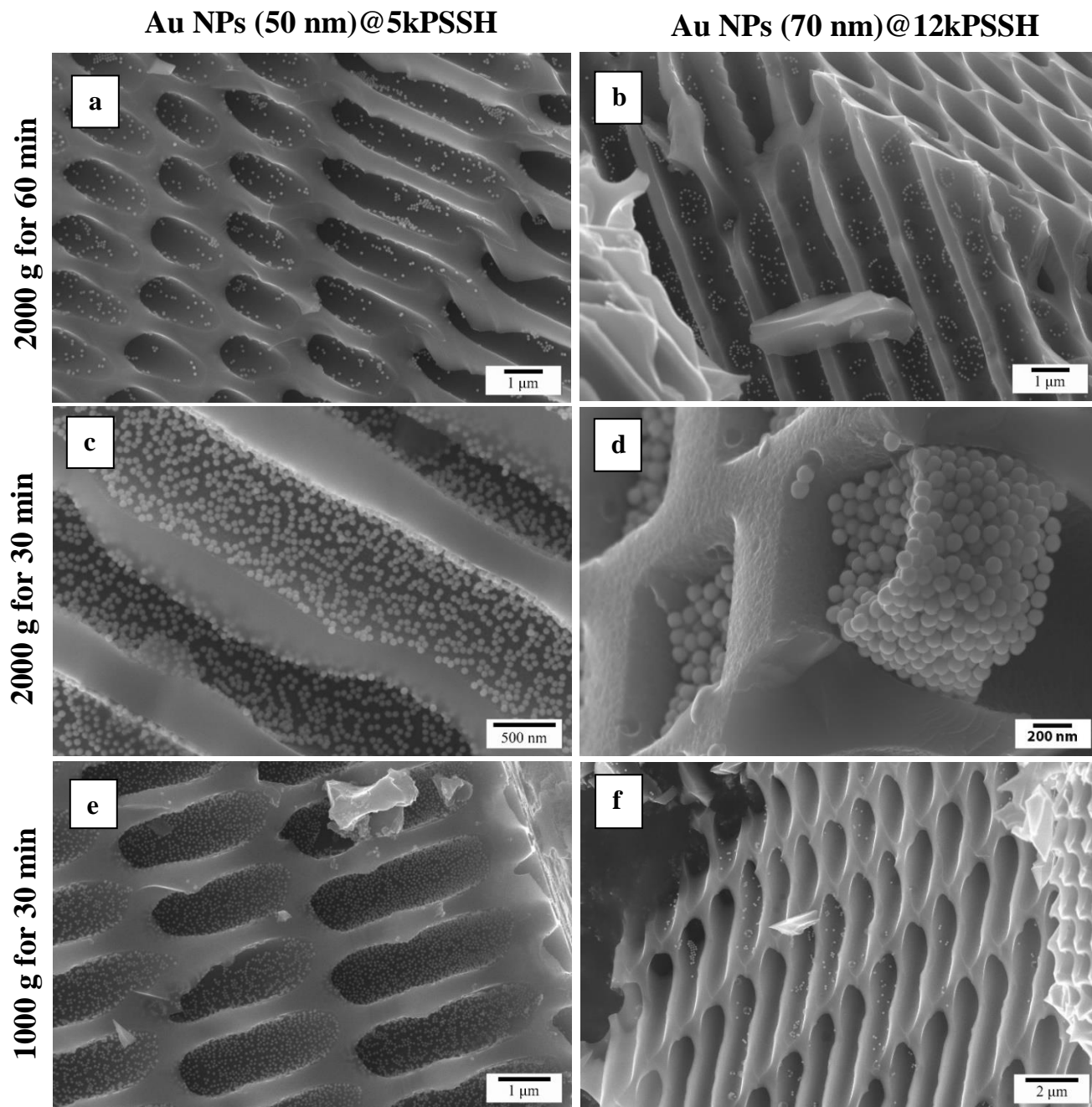


Figure 3.5. Cross-sectional SEM images of the porous membrane after interacting with Au NPs (50nm)@5kPSSH (a, c, and e) and (b, d, and f) Au NPs (70nm)@12kPSSH under several centrifugation parameters: 1,000 g for 30 min, 1,000 g for 30 min and 1,000 g for 30 min.

3.3.3 Surface coating effect

As discussed in Chapter I, the self-assembly behavior of Au NPs when forming crystals is greatly affected by the polymer ligand coating. In this context, modifying the PSSH length of the Au NPs could potentially lead to different arrangements within and on the surface of the pores of the pSi membranes. Thus, to study the effect of the PSSH chain length on the self-assembly of the Au NPs in the pores of pSi membranes, NPs with core diameters core 50nm and 70 nm were functionalized with 12kPSSH and 5kPSSH, respectively. All other parameters such as impregnation time, centrifugation speed, and time were kept constant. **Figures 3.6a, 3.6c, and 3.6e** show that coating Au NPs (50 nm) with 12kPSSH significantly altered the arrangement of NPs on the pSi membranes, eliminating the formation of 2D arrays within and on the surface of the pores. In contrast, Au NPs (70 nm) functionalized with 5kPSSH exhibited a behavior similar to that of Au NPs (50 nm)@5kPSSH, this under one of the three centrifugation conditions (1,000 g, 30 min). It is evident that there is a transition from a 3D to a 2D array (**Figure 3.6f**). However, in almost all the experiments, no well-ordered Au NPs were observed. These observations indicate that the coating ligand modifications significantly influence the self-assembly behavior of NPs and thus the interaction with the pSi membrane. This difference could be attributed to the enhanced stability of the Au NPs (50 nm) when coated with 12kPSSH, resulting in a preferential self-assembly between them instead of interacting with the walls of the pores. These results highlight the crucial role of the core diameter and surface chemistry of the NPs and the centrifugation parameters (speed and time) in determining their self-assembly within and on the surface of the pores of the pSi membranes.

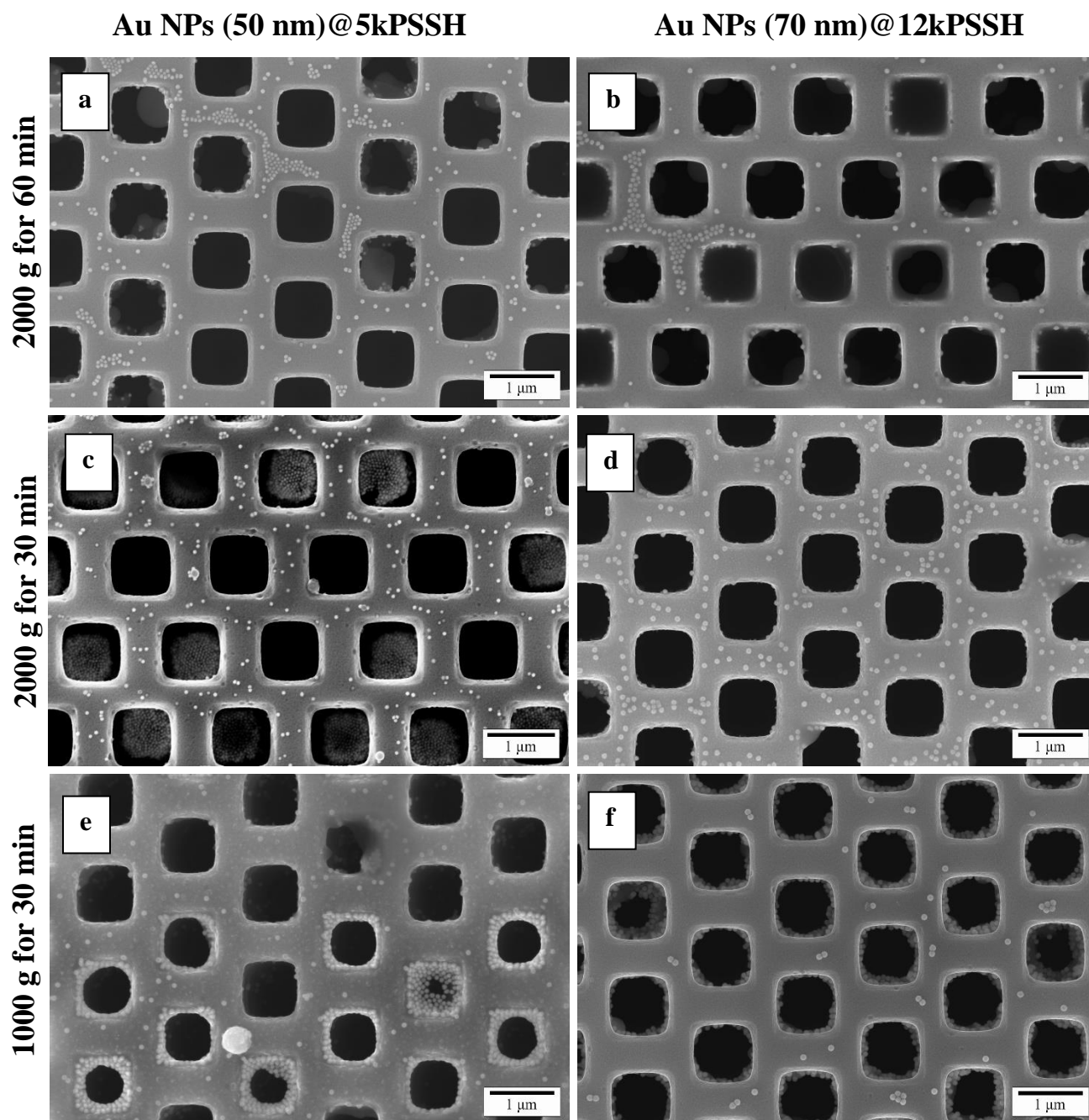


Figure 3.6. Scanning electron microscopy (SEM) images of porous silicon membranes after interaction with PSSH-functionalized AuNPs. Top view of porous silicon membranes after interacting with (a, c, and e) Au NPs (50 nm)@5kPSSH and (b, d, and f) Au NPs (70nm)@12kPSSH under several centrifugation parameters:1,000 g for 30 min, 1,000 g for 30 min and 1,000 g for 30 min.

3.3.4 Preliminary results of the impact of the temperature on the self-assembly behavior of Au NPs in the pores of porous silicon membranes

Among the various ways to improve the incorporation of NPs within and on the pores of pSi membranes, the use of a high temperature has shown good results in improving pore filling¹⁵⁷. Based on the obtained results, the two best hybrid configurations were selected to study the impact of temperature on the self-assembly process of the NPs within the pores of the pSi membranes. **Figure 3.7** shows SEM images of the two self-assembled Au NPs (50 nm)@5kPSSH and AuNPs (70 nm)@12kPSSH hybrid configurations in the pores of the pSi membranes at 100 °C. The first hybrid configuration, Au NPs (50 nm)@5kPSSH (2,000 xg, 30 min), showed long-covered areas with NPs, however, the order of the NPs was poor when compared without using temperature (**Figures 3.7a and 3.7b**). On the other hand, the second configuration, Au NPs (70 nm)@12kPSSH (2,000 xg, 30 min), results in a dramatic change from the original 3D configuration to a randomly disordered array over long areas (**Figures 3.7c and 3.7d**). These results could be explained by the collapse of the polymer ligand on the surface of the 70 nm NPs due to the temperature, which affects the global self-assembly of the NPs, resulting in NPs attached to the walls of the pores instead of interacting between them to form the 3D array. As previously mentioned, a similar behavior was observed when large Au NPs were coated with 5kPSSH. These results provide preliminary evidence of the impact of temperature on the incorporation of Au NPs into the pores of pSi membranes.

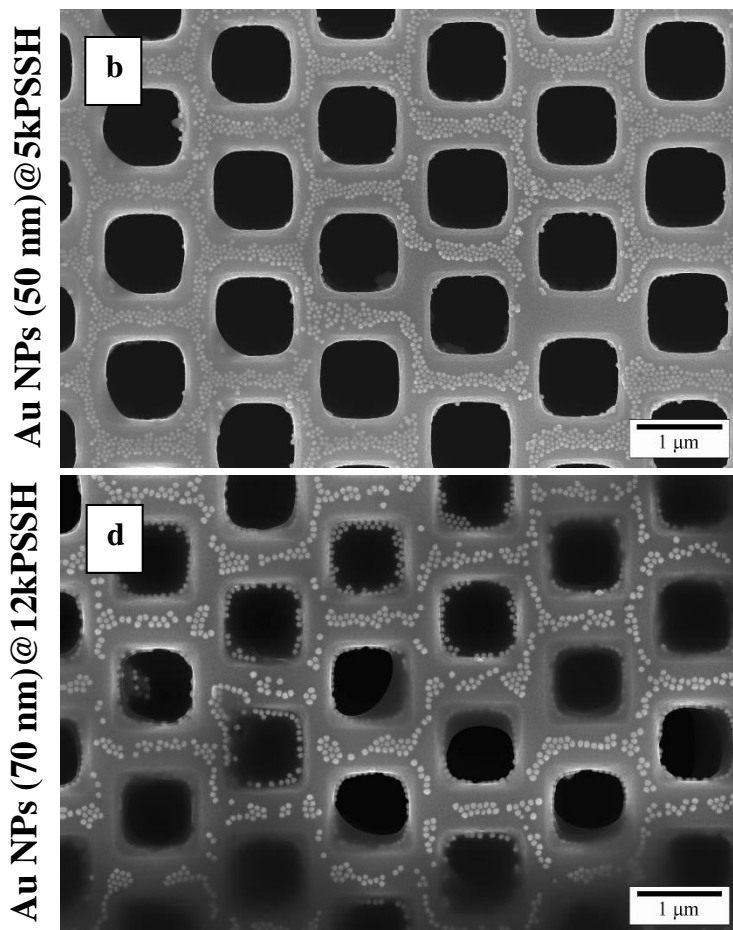


Figure 3.7. TOP view SEM images of the self-assembly of Au NPs (50 nm)@5kPSSH and Au NPs (70 nm)@12kPSSH in the pores of pSi membranes under 100 °C.

In general, the experimental findings demonstrate the generation of two different hybrid configurations of Au NPs@PSSH incorporated in pSi membranes. These configurations can be achieved by carefully controlling the core diameter and surface chemistry of the NPs, as well as the centrifugation parameters (speed and time). Notably, these results were consistently reproduced when experiments were repeated using different Au NPs@PSSH synthesis batches and conducted at room temperature, indicating the robustness of the protocol developed in this thesis.

Table 1 outlines the optimized experimental conditions used for the self-assembly of PSSH-functionalized Au NPs into 2D and 3D arrays within and on the surface of the pores of pSi membranes under ambient conditions. Overall, both pSi-Au NPs@PSSH hybrid systems exhibit uniformity and homogeneity across extended micrometer areas.

Table 3.3. Optimized parameters used for the self-assembly of Au NPs@PSSH on porous silicon membranes: Dimensionality of the array, immersion time t_{immers} , NP concentrations c_{NP} , and centrifugation parameters (speed a_{cent} and time t_{cent}). All samples were prepared at RT.					
Sample	array dimension	t_{immers} [h]	c_{NP} [nM]	a_{cent} [$\times g$]	t_{cent} [min]
Au NPs (50 nm)@5kPSSH	2D	24	~ 2.2	1,000 2,000	30
Au NPs (50 nm)@12kPSSH	2D	24	~ 2.2	2,000	30
Au NPs (70 nm)@5kPSSH	2D	24	~ 1.1	1,000	30
Au NPs (70 nm)@12kPSSH	3D	24	~ 1.1	2,000	30

3.3.5 Surface-enhanced Raman spectroscopy

In this chapter, two different hybrid configurations were achieved, each with large covered areas and with high homogeneity. This enabled easy transfer, manipulation, and characterization, ultimately opening a new door to study the collective properties of the two different Au NPs@PSSH arrays within the pores of pSi membranes. To demonstrate this, the hybrid system with 2D and 3D hybrid configurations was tested as a SERS substrate.

Microscopic images show the two hybrid configurations, one with the pSi-Au NPs (50 nm)@5kPSSH (**Figure 3.8a**) and the other with the pSi-Au NPs (70 nm)@12kPSSH arrangements (**Figure 3.8b**). As a probing molecule, we measured the PSSH ligands adsorbed on the surface of the Au NPs within the self-assembled arrays. **Figures 3.8a and 3.8b** showcase the SERS spectra obtained from several random pores for the two different hybrid configurations. Two SERS peaks can be observed, one is related to the C-C-C ring-bending mode of polystyrene at 1000 cm^{-1} , and the second to the hydrogen bending mode at 1029 cm^{-1} ,¹⁰⁸. Both strong signals can be explained by the hot spots generated in both configurations. For the first configuration, where the pSi-Au NPs (50 nm)@5kPSSH are within and on the surface of the pores of the pSi membranes, the large area provided by the pores allows for a high density of Au NPs. In contrast, the second hybrid configuration, where pSi-Au NPs (70 nm)@12kPSSH form 3D assemblies, allowed the formation of small 3D hot spots to generate a strong signal. In general, the enhanced scattering was uniform and exhibited minimal variation, indicating a consistent SERS response across a large area.

However, testing the sensitivity of the hybrid system will require the use of a probe molecule that allows a change in concentration to determine the maximum enhanced signal.

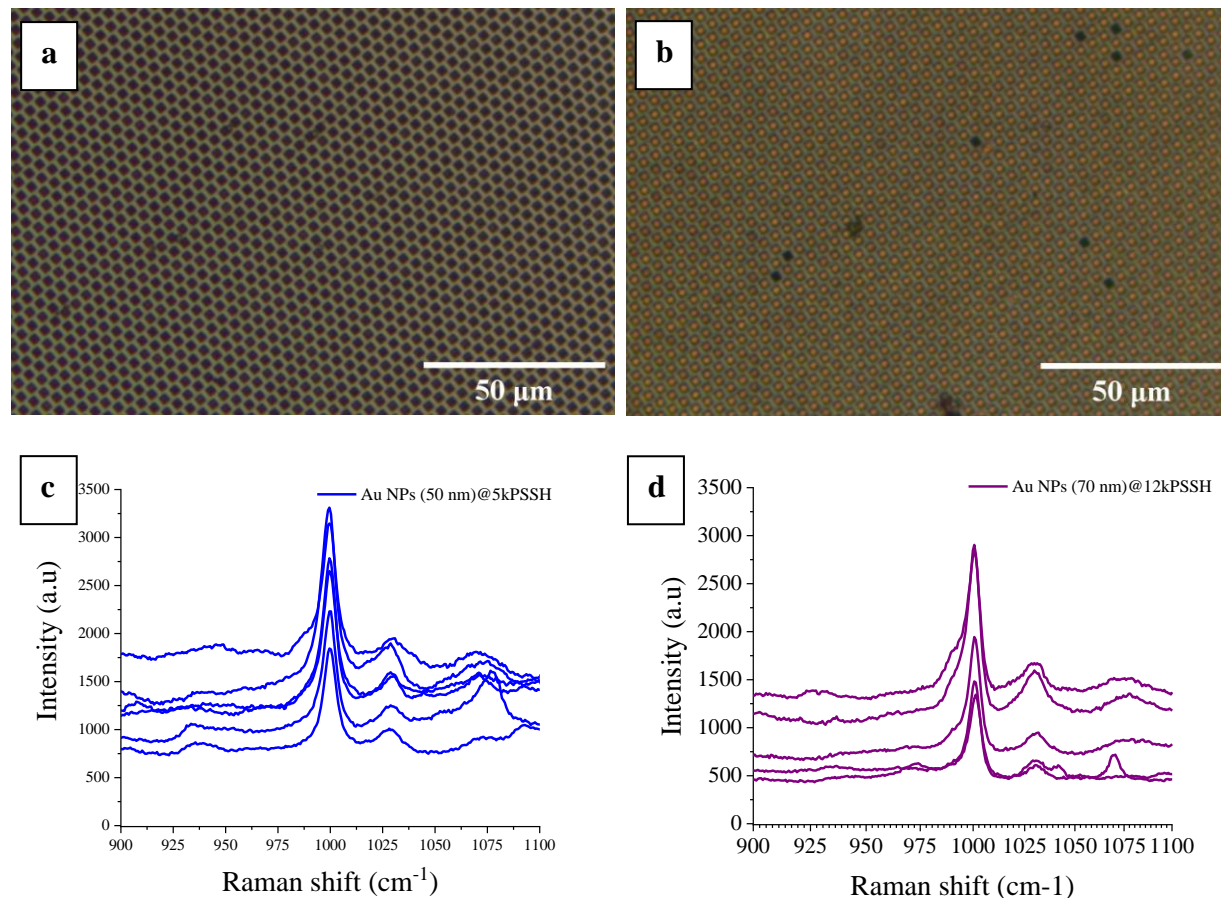


Figure 3.8. SERS spectra of the polystyrene ligand molecules in the two hybrid systems. Microscope images of the pSi-AuNPs@5kPSSH (b) and pSi-AuNPs@12kPSSH (c) hybrid configurations, and Raman spectra of the pSi-AuNPs@5kPSSH (b) and pSi-AuNPs@12kPSSH.

3.3.6 Conclusion

In this Chapter, we presented a straightforward method to control the self-assembly of Au NPs into 2D and 3D arrays within and on the pores of porous silicon membranes. The production of these two hybrid configurations can be adjusted in a very easy way by modifying the particle size, and surface chemistry of NPs as well as centrifugation speed and time parameters.

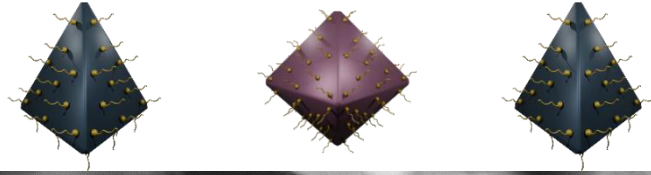
The method used here is simple and provides good reproducibility and precise control over the two configurations of the hybrid system. This could be useful in creating a SERS substrate due to the generation of many hot spots in the case of 3D arrays. On the other hand, the larger area achieved in the 2D self-assembly process could be used for catalysis because it offers good homogeneity and a large surface area, which is important for creating catalytic devices.

In the context of the SERS, the two different configurations were tested as SERS substrates by measuring the SERS spectra of polystyrene molecules in the system. The results highlight the uniformity in the signal in both hybrid systems. Thus, indicating their potential applications in photonics and surface-enhanced Raman spectroscopy. This work may open new avenues toward the design of more complex hybrid systems with increasing new collective plasmonic properties.

In future studies, it would be interesting to explore different pore diameters and thicknesses of the pSi membrane, as well as different solvents and temperatures that could have an impact on the self-assembly process. Additionally, a wide range of particle sizes and shapes could be considered, depending on the desired application.

CHAPTER IV

4 Self-assembly of 3D binary space-tessellating superstructures



4.1 Introduction

4.1.1 Self-assembly of Binary Superstructures

The self-assembly of colloidal nanoparticles (NPs) into two-dimensional (2D) and three-dimensional (3D) binary superstructures represents an important strategy for engineering new materials with unprecedented properties, for instance, photonic¹⁵⁸, quantum optics¹⁵⁹, magnetic¹⁶⁰, and thermal properties¹⁶¹. The combination of different sizes of the NPs in binary systems as well as their specific interactions has led to generating a lot of interesting structures that include CsCl, NaCl, CuAu, NaTl, AlB₂, MgZn₂, CuAu, Cs₆C₆₀^{162, 163}, and more complex as quasicrystal structures¹⁶⁴. These binary materials are of great interest for the development of diverse applications such as photonics, sensing, energy, and catalysis^{165, 69, 160}.

To date, most of the research studies have focused on forming 2D and 3D binary superstructures by arranging spherical particles of different sizes. In this context, the complexity of coassembling two polyhedral NPs with high orientational order explains the limited research on these binary structures. Furthermore, progress in colloidal chemistry now allows the production of uniform polyhedral NPs^{42, 44, 45}, and the formation of densely packed 2D and 3D structures using non-spherical NPs^{166, 167} or a mix of spherical and polyhedral NPs has gained attention in recent years^{168, 169}.

In recent years, just a few studies have been focused on the generation of binary 3D superstructures constructed from two different polyhedral NPs^{166, 170}. Recently, Zhao and colleagues have presented a library composed of 10 new binary superstructures¹⁷⁰. These superstructures can be synthesized by functionalizing the surface of polyhedral NPs with complementary DNA, which was previously modified with a short flexor ligand. This flexor has allowed the tunability of the system. Notably, among these structures, the combination of tetrahedrons with octahedrons can generate a binary honeycomb structure with an interesting tessellation structure.

4.1.2 Space-filling polyhedron

Space-filling polyhedron can be defined as a polyhedron that can be utilized to create a tessellation of space. Tessellation or tiling is the covering of a surface with one or more patterns or geometric spaces, called tiles, with no overlaps and no gaps. Thus, a space-filling polyhedron in three dimensions is a polyhedral that can tessellate space. For instance, the cube, rhombic dodecahedron, and truncated octahedron are polyhedrons that can tessellate.

A more complex tessellation, but still the simplest, can be formed if two or more polyhedrons are combined. For instance, the tetrahedral-octahedral honeycomb, also known as alternated cubic honeycomb, can be assembled by alternating regular octahedra and tetrahedra in a ratio of 1:2 (**Figure 1**).



Figure 4.1. Schematic illustration of the tetrahedral-octahedral honeycomb (TOH) structure.

These two polyhedral shapes can now be synthesized with high uniformity and in several sizes^{44, 45}. As a result, ordered assemblies of gold nanotetrahedra (Au NTd) and gold nanooctahedra (Au NOct) metallic NPs have been studied in recent years due to the emergence of interesting crystal structures^{171, 172, 173, 174, 175} and recently, new optical properties have been discovered^{176, 177, 178}. In this context, the self-assembly of binary plasmonic superstructures using these two polyhedral NPs as building blocks could lead to the generation of complex metamaterials that combine the individual plasmonic properties of each NP.

4.1.3 Forces involved in the self-assembly of 3D binary superstructures

Numerous mechanisms related to NPs properties such as size, surface chemistry, and composition, as well as self-assembly conditions such as solvent, and interaction with the desired substrate, must be carefully considered in order to optimize the formation of well-ordered 3D binary superstructures^{179, 180}. These parameters also play an important role in the creation of 2D and 3D superstructures^{181, 182}, as previously mentioned in Chapter I. However, particular focus is needed on the relationship between the complementarity of size and shape for the generation of binary 3D superstructures¹⁷⁰. Various key factors that influence the development of binary 3D superstructures can be summarized into colloidal NP stabilization, faceted building blocks, size ratio stoichiometry, and effective shape^{96, 175}. In order to avoid forming individual pure phases of each NP, a careful balance of these factors is necessary for achieving highly organized 3D binary superstructures¹⁸³.

In this final chapter, the self-assembly of 2D and 3D binary tessellating superstructures was achieved by using polystyrene ligands to stabilize the polyhedral NPs (Au NTd and Au NOct). The 3D binary superstructures were synthesized using the liquid-subphase method. These 3D structures display good uniformity and high ordered degree. The morphology and the internal crystal structure of the superstructures were elucidated through an extensive SEM analysis. The importance of the ligand coating and particle concentration was also investigated. Our results suggest that the ligand coating and particle concentration must be carefully controlled to achieve the desired 3D superstructures.

The combination of shape anisotropy and soft interactions provides tools to explore a larger structural diversity than the ones achieved with isotropic building blocks. In addition, due to their high order and good uniformity, as well as their highly densely packed structure, these plasmonic 3D superstructures are excellent candidates for plasmonic metamaterials.

Parts of this chapter are based on the ideas published or submitted in the manuscript:

1. Deep strong light-matter coupling in self-assembled 3D binary space-tessellating superstructures.

Juan J. Barrios Capuchino, Gabriela-García, Rahul Nag, Wolfgang J. Parak, Stephanie Reich, Cyrille Hamon, and Florian Schulz. *Manuscript*, 2024

4.2 Methods

Materials

Tetrachloroauric (III) acid ($\geq 99.99\%$ trace metal basis), silver nitrate (AgNO_3 , ($\geq 99.0\%$ trace metal basis), 3-butenic acid ($\geq 97.0\%$), trisodium citrate dihydrate ($\geq 99.99\%$), ascorbic acid (AA, $\geq 99.99\%$), sodium borohydride (NaBH_4 , $\geq 98\%$), cetyltrimethylammonium bromide (CTAB, $\geq 99.99\%$), and cetyltrimethylammonium chloride (CTAC, 25 wt% in water) were ordered from Sigma-Aldrich. Toluene ($\geq 99.95\%$), tetrahydrofuran ($\geq 99.5\%$), and ethanol (denat., 96%), were from VWR (USA), the respective purities are given in the brackets. Thiolated polystyrenes (PSSH, PSSH_{2k}: M_n : 2800 g mol⁻¹, PSSH_{5k}: M_n : 5300 g mol⁻¹, M_w = 5800 g mol⁻¹; PSSH_{12k}: M_n =5800 g mol⁻¹, M_w =12,400 g mol⁻¹) were purchased from Polymer Source (Canada). Ultrapure water (10.2 M Ω cm), Millipore) was used for all experiments. All reagents were used without any additional treatment. All the glassware used in the experiments was cleaned with fresh aqua regia and rinsed several times with MQ.

Synthesis of spherical and polyhedral Au NPs

Au NTd synthesis. Gold nanotetrahedra were synthesized using a seed-mediated growth method adapted from a previously reported method with minor modifications⁴⁴. In the first step, CTAC-capped Au NPs of 9 nm were prepared. Briefly, 9.9 mL of 0.7 mM HAuCl_4 was mixed with 5 mL of 200 mM cetyltrimethylammonium bromide (CTAB) in a 20 mL vial at 30 °C. Then, 0.6 mL of freshly prepared 10 mM NaBH_4 was quickly added under rapid stirring (900 rpm) for 3 min. The mixture was left undisturbed at 30° for 3 h. The newly synthesized Au NPs were purified via centrifugation twice at 9000 rpm for 90 min.

In the second step, the newly synthesized Au NPs were used as seeds for the synthesis of Au NTd. Typically, to synthesize 50 nm tetrahedra, 24.86 mL of MQ, 2.54 mL of 756 mM CTAC, 0.480 mL of 1 M KBr, and 4 mL of AA were mixed and stirred at 30 °C. Next, 0.117 mL of the seeds were added to the mixture with continuous stirring. With the help of a syringe pump, 12 mL of 2.5 mM HAuCl_4 was added to this mixture at a flow rate of 0.5 mL/h. Finally, the Au NTd were purified via centrifugation at 8500 rpm for 25 min and washed with 1 mM CTAC. Depletion-induced purification at 110 mM CTAC was used to separate the AuNTd from spherical or unwanted shaped by-products. The final product was re-dispersed in 2.5 mM CTAC.

Au NOct synthesis. Gold nanooctahedra were synthesized using a previously reported method⁴⁵. This method consists of using Au nanorods as seeds and their following controlled overgrowth into octahedral structures¹⁸⁴. Briefly, 0.045 mL of 50 mM HAuCl₄ was mixed with 4.7 mL of 100 mM CTAB in a 20 mL vial at 30 °C. Then, 0.3 mL of freshly prepared 10 mM NaBH₄ was quickly added under rapid stirring (900 rpm) for 5 min. The mixture was left undisturbed at 30° for 1 h. Next, 0.024 mL of the seed dispersion was added to 10 mL of a growth solution containing 0.1 mM CTAB, 0.5 mM, HAuCl₄, 0.08 mM AgNO₃, 10 mM HCL, and 0.8 mM of AA, and kept at 27 °C overnight. The resulting Au nanorods were purified via centrifugation twice at 8500 rpm for 25 min and redispersed in 10 mM CTAB solution to a final concentration of 2 mM in terms of Au⁰. To produce octahedral structures, 2.21 mL of 11.77 M 3-butenic acid was added to a 500 ml mixture solution constituted by 0.5 mM HAuCl₄ and 10 mM CTAB at 60 °C. When the change in color of the solution from orange to colorless indicated the reduction of Au⁺³ species to Au⁺, a certain amount of purified gold nanorods was added as seed. The mixture was kept at 60 °C for 6 h. The size of the AuNOct can be tuned by adjusting the volume of seeds. For achieving a 50 nm edge length, 6.5 mL of the rod seed solutions was added. Finally, the AuNPs were washed via centrifugation two times (3000 rpm, 30 min) and in the last washing step, re-dispersed in 2.5 mM CTAC.

The Au⁰ concentration of both polyhedral NPs was adjusted to 60 mM for further experiments.

Surface functionalization of polyhedral NPs

The polyhedral NPs were functionalized with different PSSH ligands and transferred to toluene following the procedure previously mentioned in Chapter I. Table 1 depicts the molar concentrations used for the self-assembly of binary 3D superstructures. The calculations for molar concentration for each particle used in this work for the binary self-assembly of complementary polyhedral NPs can be found in Appendix A.

Table 4.1 Molar concentration of polyhedral Au NPs used for the self-assembly of binary superstructures

Samples	Concentration of metallic gold, C _{Au} (M)	Concentration in NPs, C _{NP} (M)
Au NTd	0.00198934	9.15×10^{-13}
Au NOct	0.00310178	3.57×10^{-13}

Self-assembly of binary superstructures

Drop casting self-assembly

As-synthesized and functionalized polyhedral NPs dispersed in toluene were mixed with a concentration ratio of 1:2 (Oct : Tetra). Then, the mixture was carefully pipetted on a substrate (a carbon-coated TEM grid or a silicon substrate) and placed in a glass vial. The vial was tilted by 45° inside a low-pressure chamber. The supercrystals were assembled by evaporating relatively concentrated mixtures of polyhedral solutions at 45 °C under reduced pressure (~3.2 kPa). The sample was carefully removed for further TEM and SEM characterization.

Self-assembly air-liquid interfacial

The self-assembly of the binary structures took place in a liquid subphase using DEG. The polyhedral NPs were mixed at different concentration ratios (low and high concentration, **Table 1, Appendix 1**). The mixture was placed in an ultrasonic machine for 1 min and after carefully pipetted onto 100 µL of DEG in a Teflon well (inner diameter 0.5 cm, max. vol = 0.2mL). The well was covered with a glass circular slide in order to decrease the evaporation rate of toluene. The waiting time for binary superstructure generation was 48 hours after the toluene was completely evaporated. A gold film is clearly visible in this step. Finally, the sample was carefully transferred to a carbon-coated TEM grid for further TEM and SEM characterization.

Uv-Vis absorption spectroscopy

Absorbance measurements were carried out using a Cary Eclipse 60 Spectrometer. Quartz cuvettes (Hellma QS, Hellma, Germany) were used to measure the concentrations of polyhedral NPs after being functionalized with PSSH and transferred in toluene. The AuNTd@PSSH and AuNOct@PSSH concentrations were estimated with the absorbance at 400 nm as described by Scarabelli et al ¹⁸⁵.

Structural analysis

Scanning electron microscopy (SEM) images were obtained using a Zeiss Sigma (GEMINI) operated at an accelerating voltage of 3kV. To characterize the morphology and self-assembly distribution of superstructures, the previously collected films on carbon-coated grids were directly attached to a holder SEM clip. Side-view SEM images were obtained by attaching the sample to a

holder SEM clip at 45°. High-resolution SEM micrographs were obtained using the SE2 detector. The working distance was adjusted to a range between 2.5 mm and 3.9 mm.

Scanning transmission electron microscopy (STEM) images were obtained using a Hitachi setup operated at an accelerating voltage of 30 kV. To characterize the morphology and self-assembly distribution of 2D and 3D superstructures, the samples transferred to a carbon-coated grid were analyzed. High-resolution STEM micrographs were obtained using both SE and BFSTEM detectors. The working distance was adjusted to 8.5 mm.

Transmission electron microscopy (TEM) micrographs of AuNTd@PSSH and AuNOct@PSSH were performed on a JEOL JEM-1011 microscope with an operating voltage of 100kV. The TEM samples were prepared by dropping 10 μ L of polyhedral NPs solution onto a carbon-coated TEM grid. The particle sizes were calculated by using the software Image J 1.53e from the TEM image.

4.3 Results and Discussion

The polyhedral NPs used in this work were carefully synthesized to be complementary in size and shape. As a working basis, gold nanotetrahedra (Au NTd) and gold nanooctahedra (Au NOct) were synthesized and functionalized by ligand exchange in tetrahydrofuran (THF) with thiol-terminated polystyrene (PSSH) molecules to stabilize the NPs and promote the self-assembly of superstructures. A representative illustration of the ligand exchange is shown in **Figure 4.2a**. **Figure 4.2b** shows the absorbance spectra of the AuNTd and AuNOct after being functionalized with 5kPSSH and dispersed in toluene. Analysis of transmission electron microscopy (TEM) images shows the size of both polyhedral NPs: Au NTd (50 nm)@5kPSSH and Au NOct (50 nm)@5kPSSH, with edge length sizes of 50.997 ± 0.73 nm (**Figure 4.2c**) and 50.27 ± 0.03 nm (**Figure 4.2d**). The individual self-assembled polyhedral NPs exhibit hexagonally close-packed monolayers.

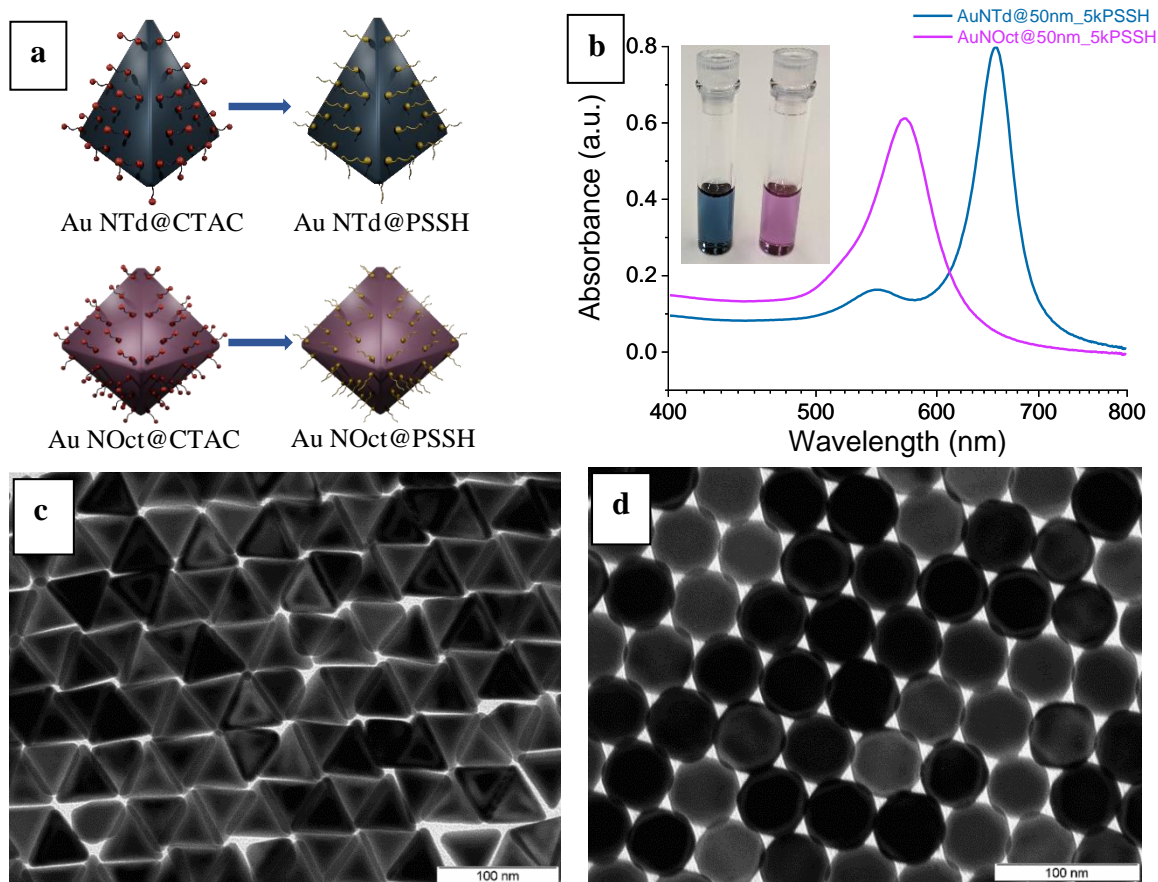
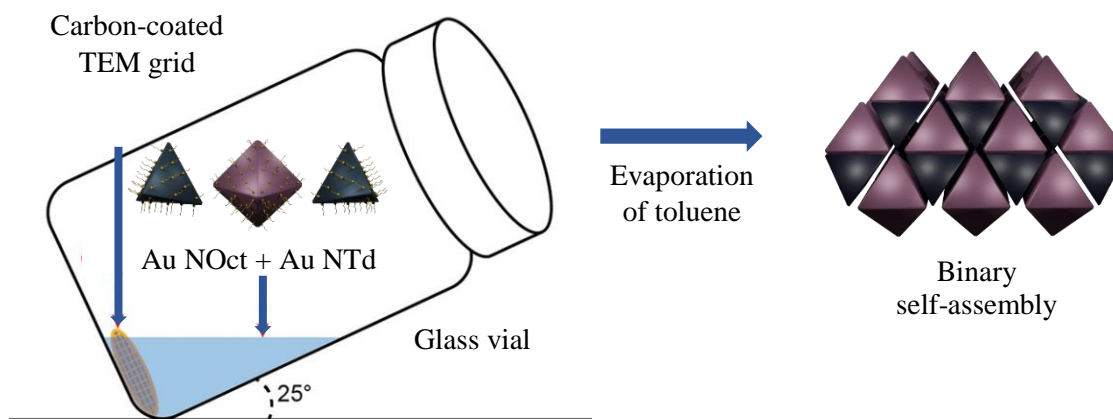


Figure 4.2. Synthesis and characterization of gold nanotetrahedra (Au NTd) and gold nanooctahedra (Au NOct) NPs. (a) Schematic illustration of the ligand polymer exchange of AuNTd and AuNOct NPs, (b) absorbance spectra of Au NTd and Au NOct functionalized with polystyrene (PSSH, 5k). The inset shows a photograph of Au NTd (left) and Au NOct (right) solutions functionalized with 5kPSSH and dispersed in toluene. TEM images of the (c) AuNTd50@5kPSSH and (d) AuNOct50@5kPSSH NPs,

4.3.1 Self-assembly of 2D binary supercrystals by using evaporation-based self-assembly

The binary supercrystals were first created using the evaporation-based self-assembly method. Briefly, the Au polyhedral NPs are carefully mixed and concentrated in a small volume, typically 50 μL . Separately, a carbon-coated TEM grid is placed on the surface of a silicon wafer, and both substrates are placed inside a glass vial tilted at 25° . Next, the mixture is carefully pipetted onto the surface of the substrates. The typical evaporation process takes 3 hours. The substrates are easily removed and prepared for characterization with SEM or TEM. **Scheme 1** shows a representative illustration of this process.



Scheme 4.1. Schematic illustration of the setup used for the self-assembly of binary superstructures of complementary PSSH-functionalized polyhedral NPs using the evaporation-based method.

Figure 4.3 shows scanning electron microscopy (SEM) micrographs of the formation of monolayers through the self-assembly of binary polyhedral NPs. **Figure 4.3a** shows low-magnification SEM images of monolayers with various crystal defects randomly dispersed on the

coated carbon TEM grid. Interestingly, a closer examination of high-magnification SEM images of different selected square areas reveals the generation of binary monolayers with a tetrahedral-octahedral honeycomb (TOH) structure (**Figures 4.3b and 4.3c**). However, the TOH motifs were small and only several nm² in size. In addition, the generation of small domains of pure Au NOct assemblies was observed. The polyhedral NPs molar concentration used in these experiments is presented in **Table 4.1**. These results suggest that the fast evaporation induced in the system is the main force in the self-assembly process since this method normally leads to the formation of monolayers^{164, 186, 163}. Reducing the evaporation rate has shown good results for generating 3D structures¹⁸⁷. Thus, the evaporation rate must be decreased to prevent rapid evaporation and aid binary 3D self-assembly.

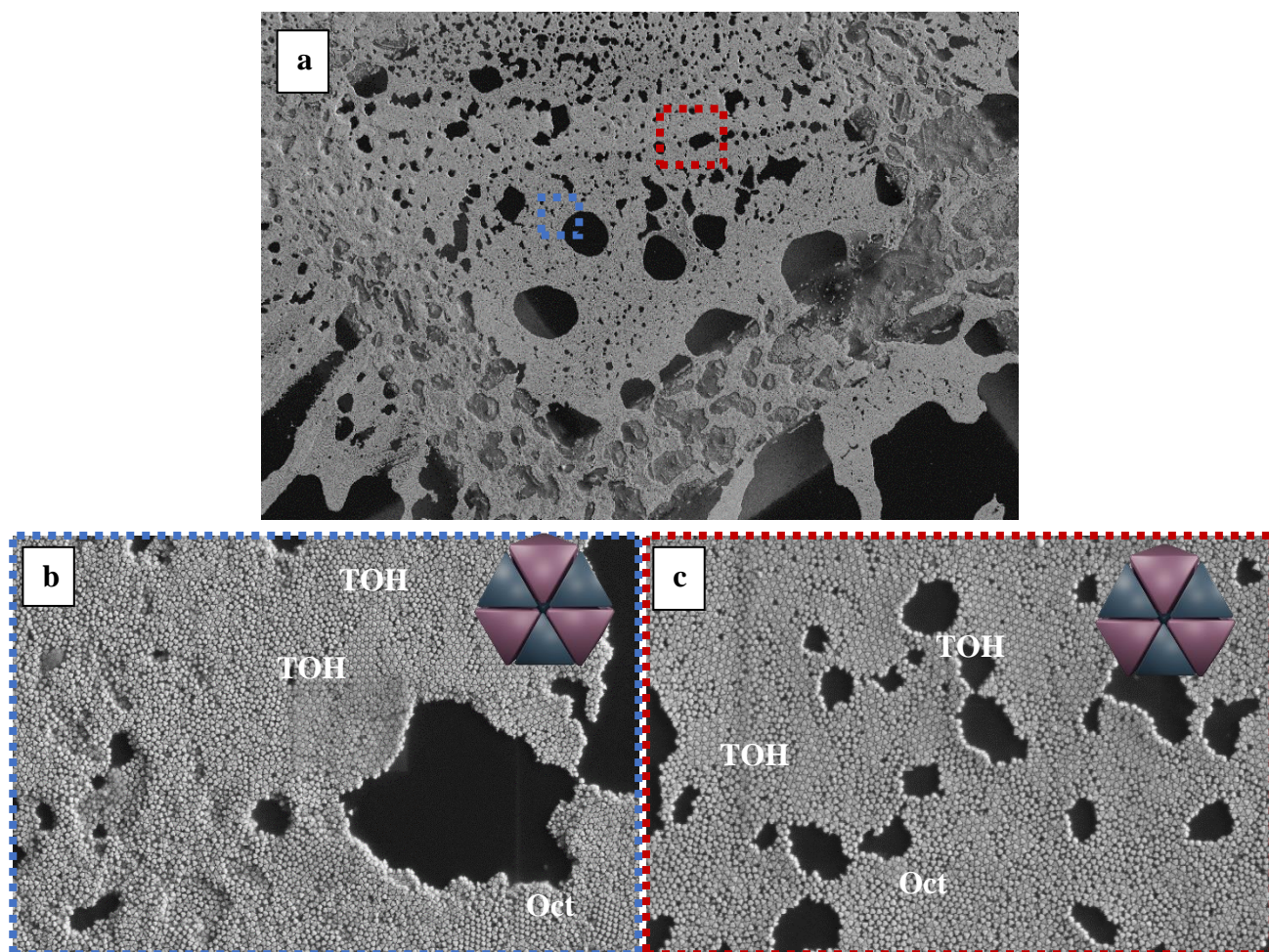


Figure 4.3. Self-assembly of binary superstructures using the evaporation-based self-assembly method. a) High-magnification scanning electron microscopy (SEM) images of self-assembled complementary PSSH-

functionalized Au NOct and Au NTd NPs. (b and c) Low-magnification SEM images of monolayers with small domains of the binary TOH structure. The insets show a model of the binary honeycomb structure.

4.3.2 Self-assembly of 2D and 3D binary superstructures by using air-liquid interfacial method

An alternative method for producing 2D and 3D superstructures involves the one carried out using the air-liquid subphase method. As mentioned in the Introduction, this method has shown promise in the generation of excellent structural order and highly densely packed superstructures. Thus, the use of this method was investigated for the self-assembly of 3D binary structures. The successful generation of 3D binary superstructures was achieved through the self-assembly of PSSH-functionalized Au NTd and Au NOct on a liquid subphase. A schematic of this process is illustrated in **Figure 4.4a**. Initially, the polyhedral NPs are mixed in a combination NP number ratio of 1:2 (Octahedral-tetrahedral). The mixture is then added to a liquid-liquid subphase using DEG in a Teflon well. The Teflon well is covered with a glass slide to reduce the evaporation rate of the toluene. Once the toluene has completely evaporated, a gold film appears (**Figure 4.4b**). The film is transferred to a desired substrate (silicon or TEM-coated grid). A photograph of the typical polyhedral mixture and the gold film formation is presented in **Figure 4.4b**.

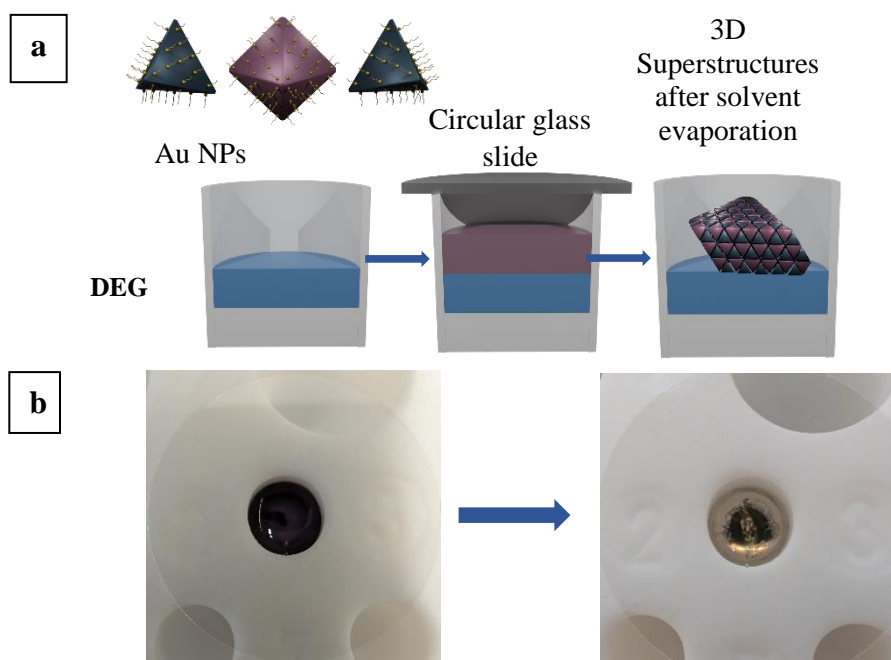


Figure 4.4. Schematic illustration of the self-assembly of binary 2D and 3D superstructures in an air-liquid subphase using DEG. Photographs of the mixed binary solution (left image) and the formed superstructures gold film after toluene evaporation (right image).

It is worth noting that the self-assembly of the binary superstructures was investigated using two different concentrations while maintaining the same number ratio of 1:2 (octahedral-tetrahedral) (refer to **Table 2, Appendix**). Transmission electron microscopy (TEM) and SEM micrographs were employed to examine the morphology of these self-assembled binary superstructures. TEM images of binary monolayer superstructures obtained after mixing the complementary NPs are shown in **Figures 4.5a** and **4.5b**. It can be observed that the binary TOH domains were just a few nm² in size and were surrounded by random mixtures of polyhedral NPs. Small domains of pure Au NOct (50 nm)@P5kPSSH assemblies were also observed, while pure Au NTd assemblies were not observed in these experiments.

SEM images at low magnification reveal the formation of 3D binary superstructures, which were spontaneously assembled at low (**Figures 4.5c**) and high concentrations (**Figures 4.5d**) and dispersed randomly on carbon-coated TEM grids. In both experiments, the generation of micrometer-sized superstructures was observed. However, the impact of the concentration is clearly visible in the uniformity of the superstructures. On the other hand, high-magnification SEM images of the self-assembled 3D binary superstructures indicate that high NP concentration resulted in binary structures approximately twice the size of those formed at low concentrations (**Figure 4.5e** and **Figure 4.5f**). Notably, the generation of the TOH binary structures was observed under both experimental conditions.

Furthermore, size distribution analysis of the 3D superstructures, analyzed from low-magnification SEM micrographs (**Figure A1, Appendix**), revealed sizes of $1.43 \pm 0.39 \mu\text{m}$ for low concentration and $2.98 \pm 0.5 \mu\text{m}$ for high concentration of NPs. The formation of the TOH crystal structure aligns with previous simulations, where hard tetrahedral and hard octahedral NPs were combined¹⁸³. These findings highlight the importance of polyhedral NP concentration in generating well-ordered 3D superstructures with high uniformity and homogeneity.

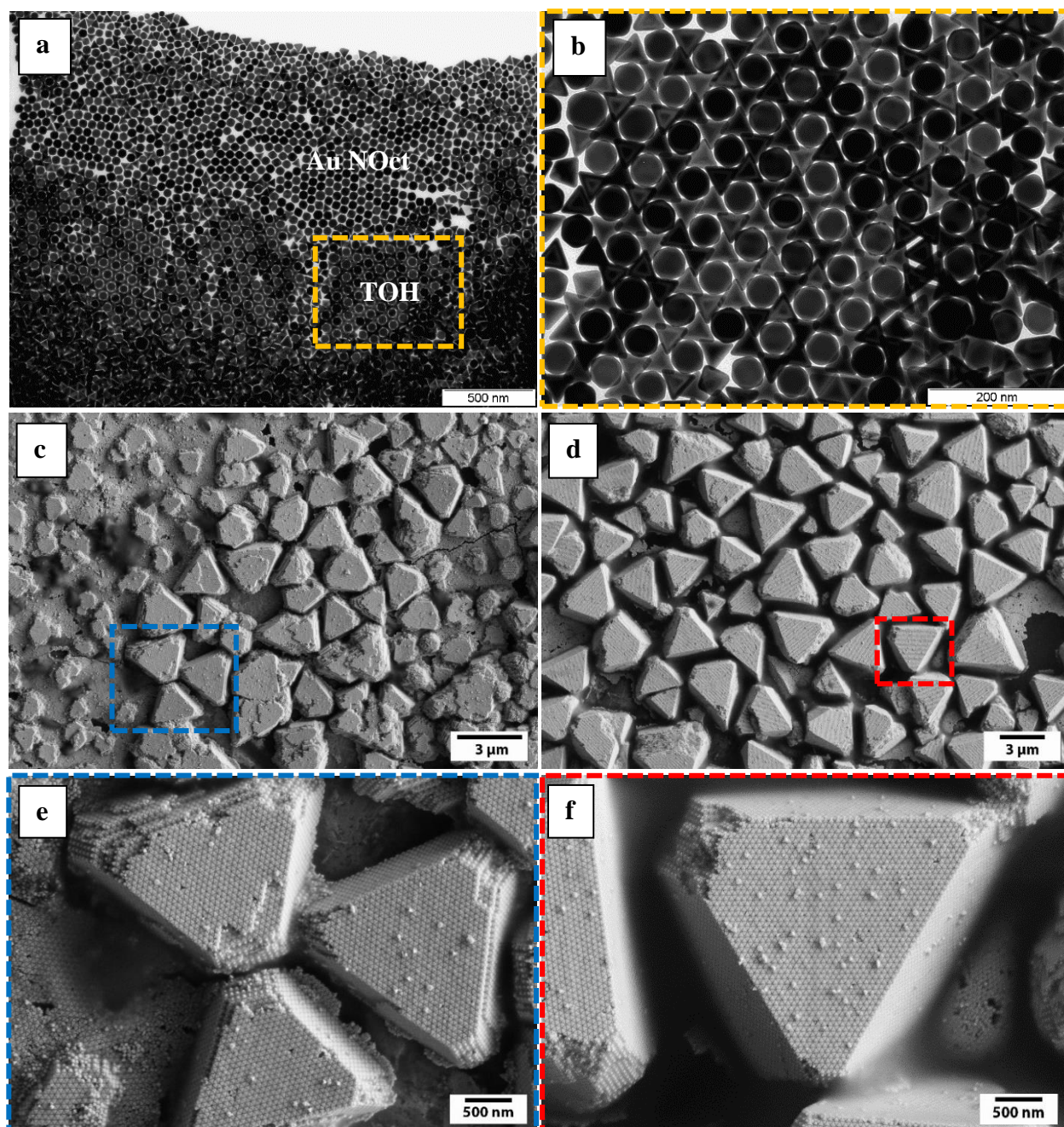


Figure 4.5. Self-assembly of 2D and 3D binary superstructures self-assembled from Au NTd (50 nm)@5kPSSH and Au NOct (50 nm)@5kPSSH with a number ratio of Td : Oct (2 : 1) by using the air-liquid subphase self-assembly method. (a) Low-magnification TEM image of 2D binary superstructures and (b) high magnification TEM image of the orange outlined area. Low-magnification SEM images of the 3D binary superstructures using (c) low and (c) high concentrations of polyhedral NPs. (e and f) High-resolution SEM images of the corresponding outlined squares displaying the characteristic prims-shaped superstructure.

Interestingly, a closer examination of the SEM images revealed the formation of large areas with different thicknesses when using high concentrations of NPs. Thus, to explore the morphology of these layers, scanning transmission electron microscopy (STEM) images were analyzed. **Figure 4.6a** reveals 2D monolayers across large areas, showcasing the coexistence of binary supercrystals and pure assemblies of Au NOct, while a different region shows the formation of different layers (**Figure 4.6c**). Notably, in both experiments, the coexistence of two different crystallization phases was observed. In previous simulation studies, the coexistence of three different crystallization phases was observed when combining hard tetrahedral and hard octahedral particles: binary, pure octahedral phase, and quasicrystal domains ¹⁸³. However, our experiments did not show the formation of quasicrystal domains composed of tetrahedral NPs.

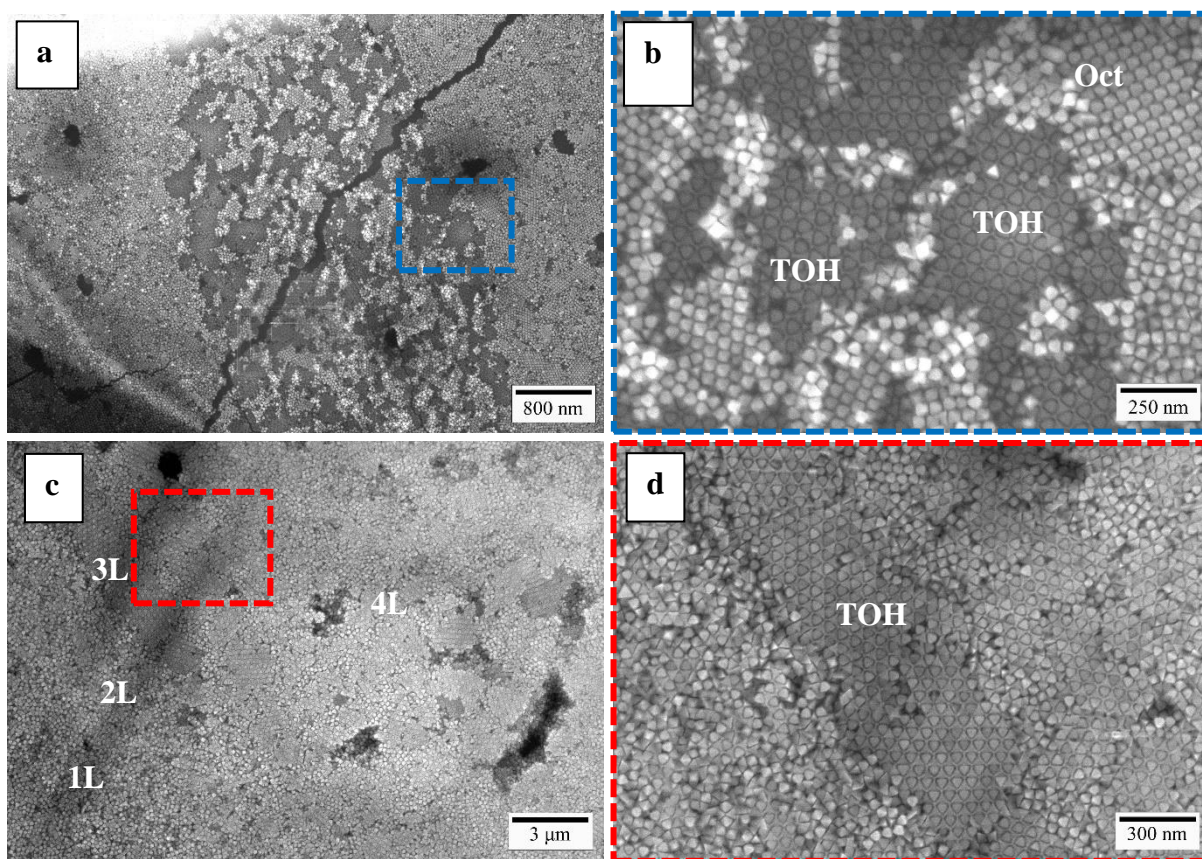


Figure 4.6. Scanning transmission electron microscopy (STEM) images of binary monolayers and multilayers. (a and c) Low-magnification STEM images of binary (a) monolayers and (c) multilayers are self-assembled from Au NTd (50 nm)@5kPSSH and Au NOct (50 nm)@5kPSSH NPs. (b and d) High-magnification STEM images of the corresponding outlined squares showing the binary TOH crystal structure.

4.3.3 Influence of Surface Ligand

As mentioned in Chapters I and II, the ligand coating may impact the self-assembly behavior of the superstructures. To evaluate this hypothesis, the Au NTd and Au NOct were functionalized with two additional polymer chain lengths, a shorter chain (2kPSSH) and a longer chain (12kPSSH). Under identical experimental conditions, NPs coated with 2kPSSH did not form any crystal structure at low concentrations (**Figure 4.7a**), while high concentrations resulted in the formation of small TOH and pure AuNOct domains (**Figure 4.7c and 4.7d**). Similarly, when polyhedral NPs were coated with 12kPSSH, comparable behavior was observed. Low-magnification SEM reveals large films comprising a mixture of these polyhedral NPs. High-magnification SEM images show that the polyhedral NPs are randomly mixed. These findings strongly suggest that PSSH plays a crucial role in generating long-ordered 3D binary superstructures. This is in agreement with previous results, for instance, Zhao et al, show that to form 3D binary complementary superstructures, the ligand attached to the polyhedral NPs has to be carefully controlled ¹⁷⁰.

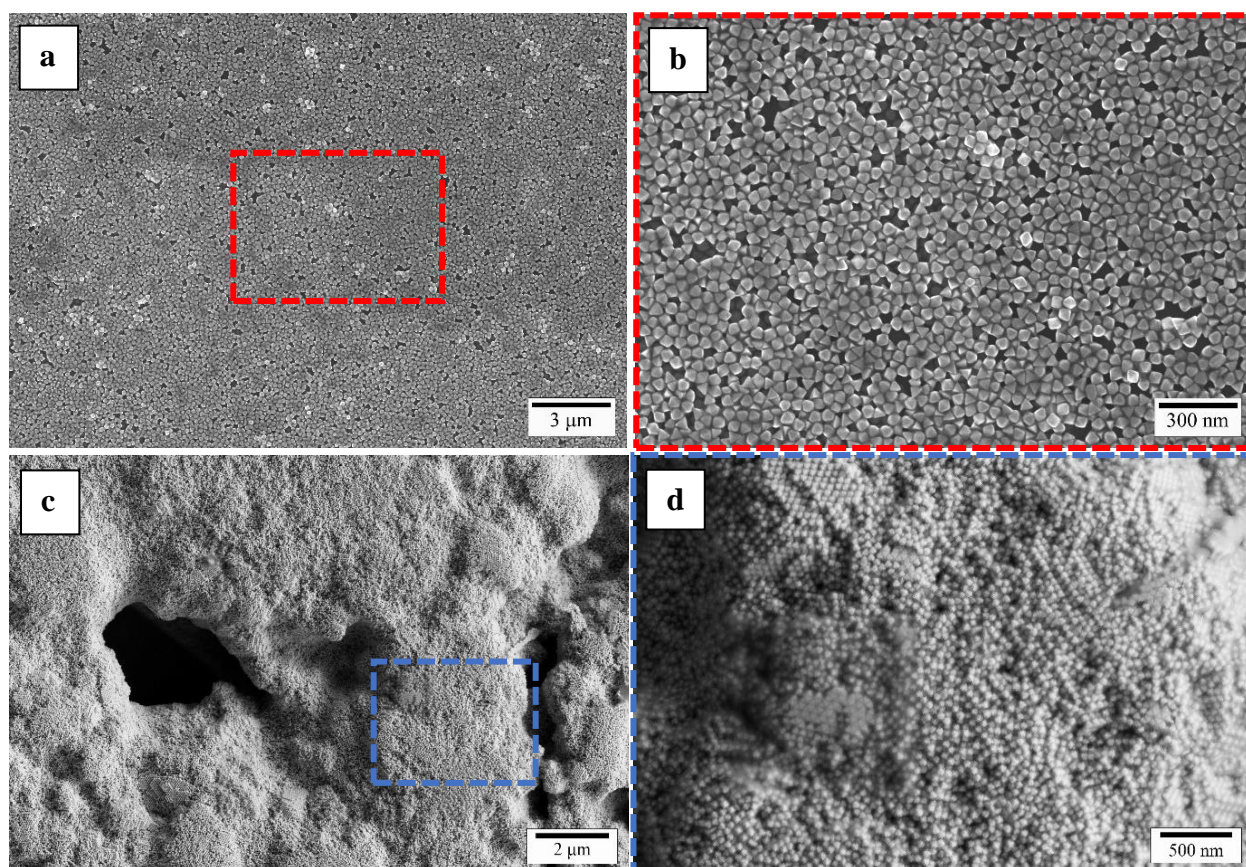


Figure 4.7. Electron microscopy images of binary polyhedral NPs. (a and c) STEM and SEM images of the binary supercrystals self-assembled from Au NTd (50 nm)@12kPSSH and Au NOct (50 nm)@12kPSSH at (a) low and (c) high concentration, respectively. (c and d) High-magnification STEM and SEM images of the corresponding outlined squares showing the binary TOH crystal structure.

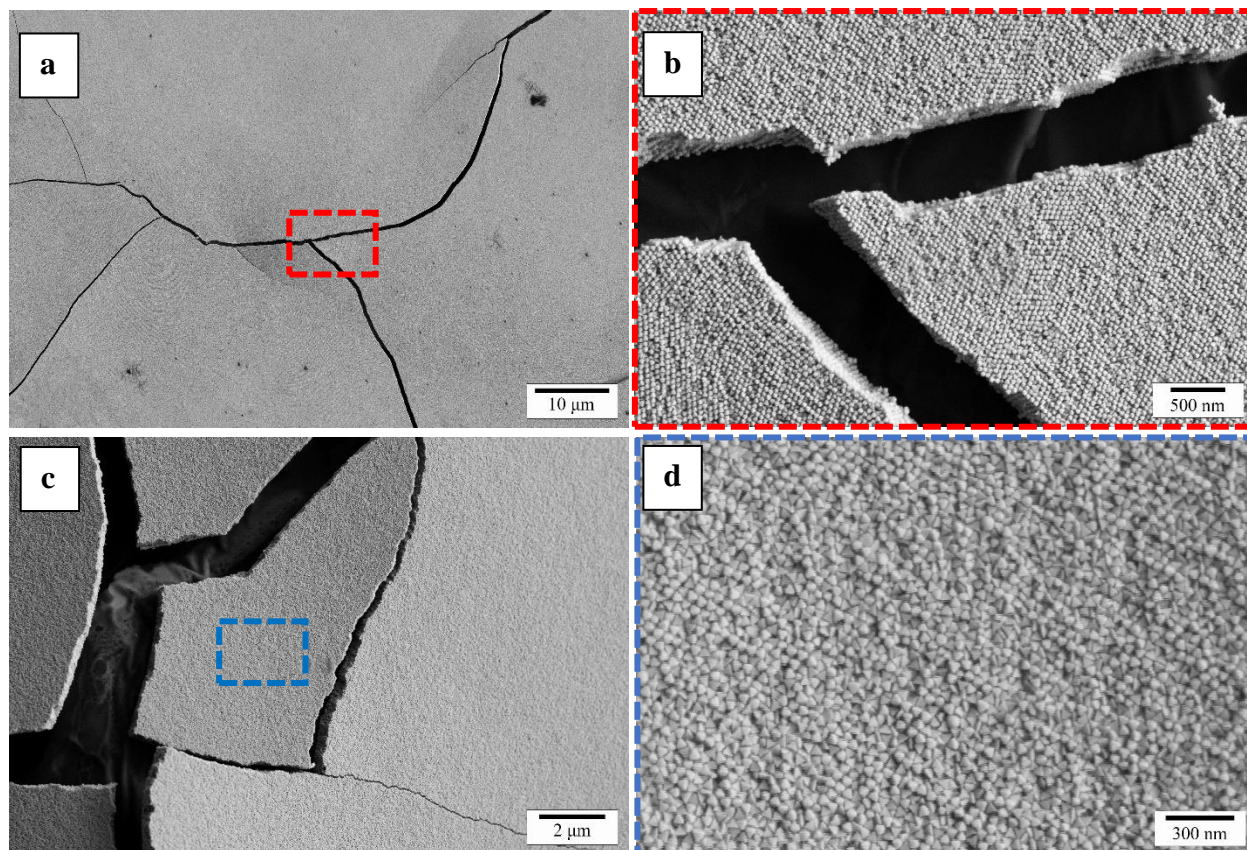


Figure 4.8. SEM images of binary polyhedral NPs. (a and c) Low-magnification SEM images of the binary supercrystals, self-assembled from Au NTd (50 nm)@12kPSSH and Au NOct (50 nm)@12kPSSH NPs at (a) low and (c) high concentration, respectively. (c and d) High-magnification SEM images of the corresponding outlined squares showing the binary TOH crystal structure.

4.3.4 Structural analysis of the 3D binary superstructure

To examine the three-dimensional structure and the internal packing symmetry of the 3D binary superstructure, high-resolution SEM images of defective areas, as well as top and side views of different superstructures, were analyzed. **Figure 4.9a** shows a top view of the 3D superstructure. **Figures 4.9b** and **4.9c** depict the typical TOH structures along all the 3D superstructures. The

uniformity, homogeneity, and crystallinity of the 3D binary superstructures are well observed across all the structures. The typical honeycomb structures can be observed in these images. SEM images of the edge view of the superstructures confirm the tetra-octa honeycomb (TOH) crystal structure

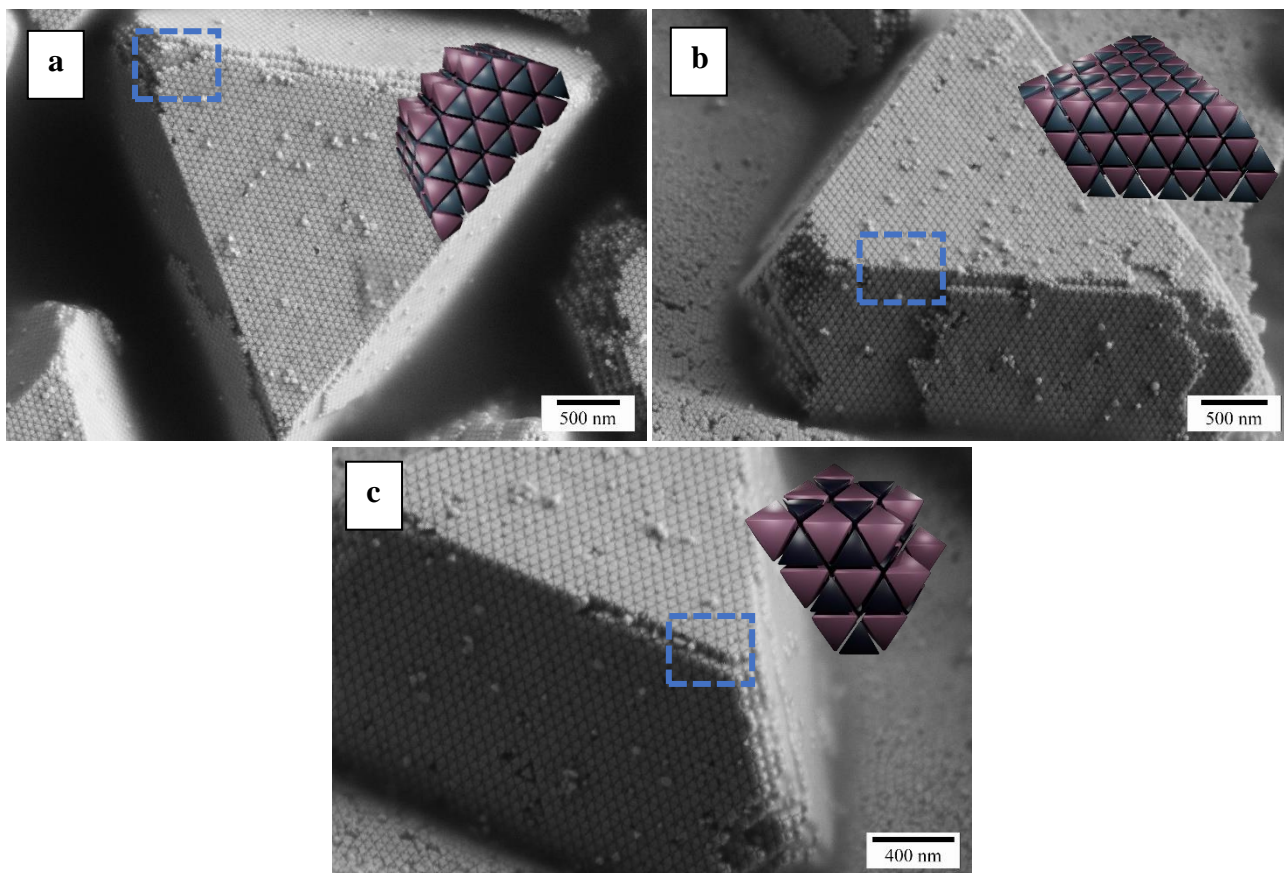


Figure 4.9. 3D binary superstructures self-assembled from Au NTd and Au NOct NPs with TOH crystal structure. (a-c) High-resolution SEM images of the top view (a), side view (b), and edge view (c) of the binary 3D TOH superstructure obtained by the self-assembly of Au NTd (50 nm)@5kPSSH and Au NOct (50 nm)@5kPSSH at high concentration. The insets show schematic models of the 3D superstructures at different angles made from Au NTd (blue) and Au NOct (violet).

4.4 Conclusion

In summary, this chapter presented the self-assembly of 3D binary tessellating superstructures. The self-assembly occurs when two complementary polyhedral NPs, Au NOct, and AuNTd, both functionalized with different PSSH, are mixed in a combination ratio of 1:2. The air-liquid subphase method was employed to achieve the 3D binary superstructures. Furthermore, it was observed that the self-assembly of the binary system is strongly influenced by the ligand coating and the concentration of the polyhedral NPs. Extensive SEM analysis demonstrated that the resulting 3D binary crystals exhibit highly uniform, homogeneous, and reach micrometer sizes.

In this context, we propose that even more complex superstructures could be assembled using a similar approach, or by altering the shape-complementary polyhedral NPs, composition, or surface modifications. To the best of our knowledge, the successful 3D binary superstructure achieved here, as well as its micrometer size, are among the largest reported to date for these structures. These findings suggest that these binary systems are suitable and could be valuable for future plasmonic applications and fundamental studies of the self-assembly process of more complex binary systems.

4.5 Appendix

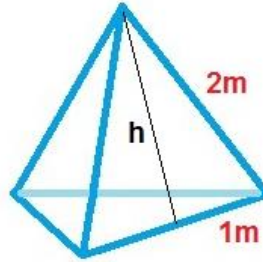
Determination of the concentration of polyhedral NPs

The packing fraction can be determined as follows:

$$\tau = \frac{2V_{tetra} + V_{octa}}{V_{unit\ cell}}$$

The edge length of each polyhedral particle was calculated from TEM images.

The volume of a tetrahedron can be determined as follows:



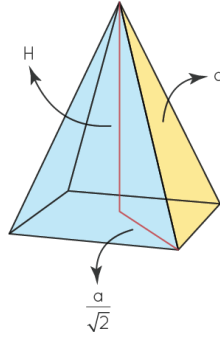
Given that the regular tetrahedron has an edge length of a . The surface area of a regular tetrahedron “ a ” is four times the area of an equilateral triangle.

$$A = 4 \times \left(\frac{\sqrt{3}}{4} a^2 \right) = a^2 \sqrt{3}$$

The height of a regular tetrahedron is $\frac{\sqrt{6}}{3} a$. The volume of a regular tetrahedron can be calculated using the same method as other pyramids, which is one-third of the base area multiplied by its height. Since the base is an equilateral triangle, the formula becomes:

$$V = \frac{1}{3} \times \left(\frac{\sqrt{3}}{4} a^2 \right) \times \frac{\sqrt{6}}{3} a = \frac{a^3}{6\sqrt{2}}$$

The volume of an octahedron can be determined as follows:



The surface area A of a regular octahedron can be found by summing the areas of all eight equilateral triangles, while its volume V is twice the volume of a square pyramid with edge length a .

$$A = 2\sqrt{3}a^2$$
$$V = \frac{1}{3}\sqrt{2}a^3$$

The mass of the gold can be determined as:

$$m_{AU} = C_{AU} \times V_{sol} \times M_{AU}$$

Where C_{AU} is the mass gold concentration, V_{sol} , is the volume of the solution and M_{AU} , is the molar mass of the gold.

The mass of the tetrahedral and octahedral (m_{NP}) can be calculated as:

$$m_{NP} = \rho \times V_{NP}$$

Where ρ is the bulk density of gold and V_{NP} , is the volume of one tetrahedron and one octahedron determined from TEM image analysis.

Then, we can estimate the concentration of nanoparticles in the dispersion as follows:

$$C_{NP} = \frac{m_{AU}}{m_{NP} \times N_A}$$

Where N_A , is the Avogadro number.

The molar concentration for each particle used in this work is summarized in the following table:

Table 2

Table A1 Molar concentration of polyhedral NPs used for the self-assembly of 2D and 3D binary superstructures			
Nanoparticles	Concentration of metallic gold, C_{Au} (M)	Low concentration in NPs, C_{NP} (M)	High concentration in NPs, C_{NP} (M)
Tetrahedron	0.00198934	9.15×10^{-13}	18.30×10^{-13}
Octahedron	0.00310178	3.57×10^{-13}	7.14×10^{-13}

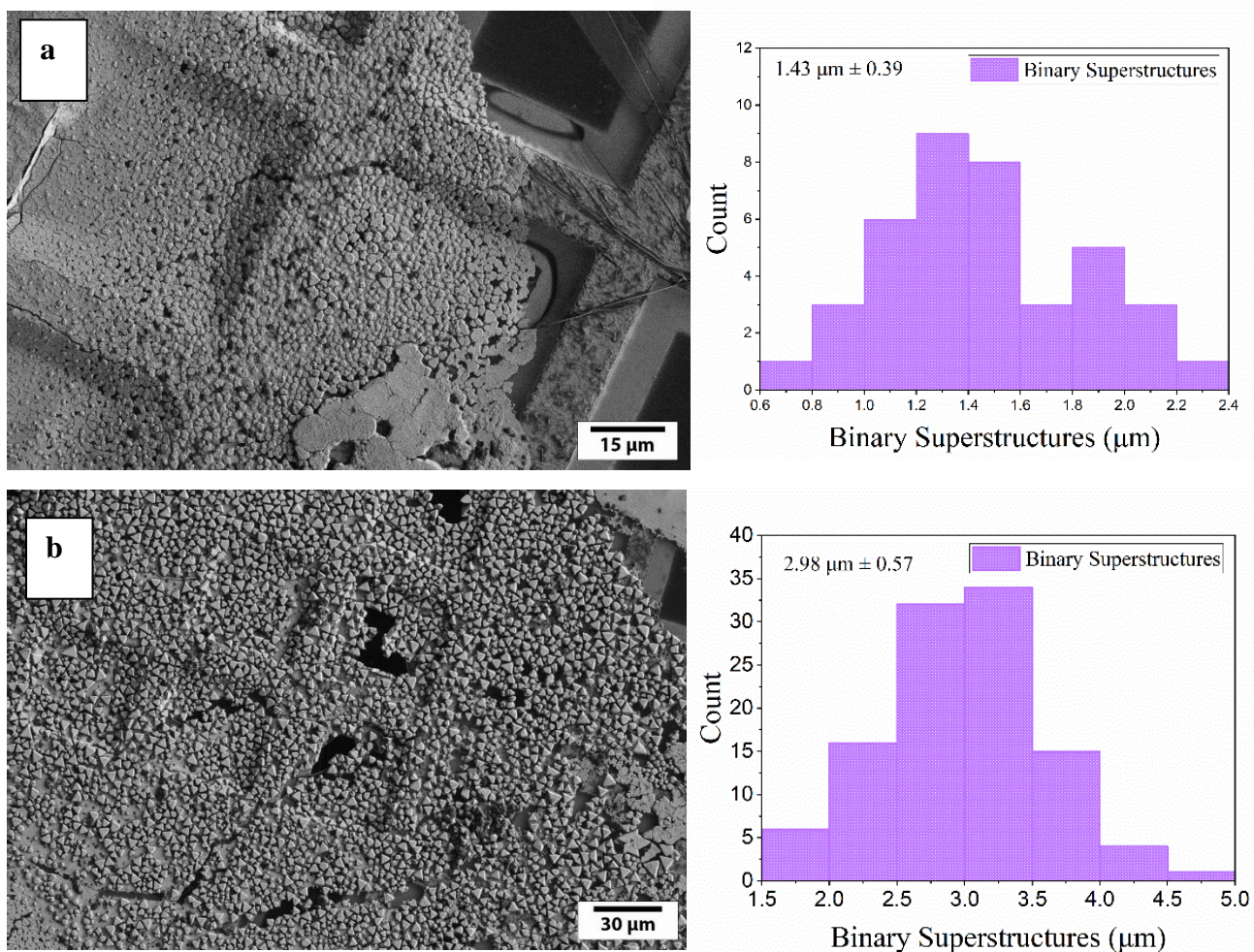


Figure A1. Low magnification SEM images of large areas with randomly self-assembled 3D binary superstructures, which are self-assembled from AuNTd@5kPSSH and AuNOct@5kPSSH at low and high concentrations. The inset shows a statistical histogram of corresponding superstructure sizes.

CHAPTER IV

5 Conclusions and Future Directions

The fabrication of plasmonic supercrystals with defined optical properties has led to a huge improvement in various research fields such as catalysis, light-matter coupling, and surface-enhanced Raman spectroscopy. Particularly, in the field of light-matter coupling, fine control over the supercrystals such as length, thickness, uniformity, and homogeneity, as well as crystal structure, is still a research field. In this context, this thesis contributes to the understanding of the self-assembly of Au NPs into supercrystals. In this conclusion, the limitations and future studies specific to each experimental project are discussed. The thesis ends with concluding remarks concerning the future directions of the research topics discussed in this work.

In the first chapter, the optimization parameters for synthesizing high-quality 2D and 3D AuNP supercrystals self-assembled from Au NPs@PSSH with core diameters sizes ranging from 25 nm to 120 nm were investigated. TEM and SEM methods were used to characterize the shape, morphology, and length of the Au NP supercrystals. Thus, it was demonstrated that precise control over the quality of the individual Au NPs as well as the concentration of the particles is crucial to achieving reproducible and high-quality supercrystals. The use of a high concentration of Au NPs with core diameters below 70 nm results in supercrystals with two different growth modes: layered and island growth modes. Interestingly, by modifying the polymer ligand on particles with a diameter of 70 nm, it was possible to change the crystal structure from hexagonal-close packed to cubic-close packed. These findings expand the knowledge of the synthesis of long-range supercrystals with high uniformity and homogeneity. These supercrystals can find applications in photonics, catalysis, or as a SERS substrate.

For future work, introducing more parameters such as temperature, controlled vacuum, or the in-situ tracking of the growing process of supercrystals could add new insights into the fundamental laws that govern the self-assembly of AuNP supercrystals. In addition, it could be interesting to use the latest optimized parameters for studying the different growth modes or the phase transitions modes (hexagonal-close packed and cubic-close packed) in the supercrystals along with X-ray correlation spectroscopy (XPCS) or small-angle X-ray scattering (SAX). Another interesting

technique to consider alongside these could be the use of liquid cell transmission electron microscopy (LQTEM). This technique can be used to understand the dynamics that govern the self-assembly of Au NP into supercrystals in real time.

In the second chapter of the thesis, the incorporation of highly ordered Au NPs into the pores of porous silicon membranes was studied. By varying particle diameter, surface chemistry, as well as centrifugation parameters such as speed and time, 2D and 3D well-ordered and long-range arrays were incorporated within the pores of porous silicon membranes. The obtained large-scale hybrid systems in combination with a high degree of high order and periodicity, allow the concentration of Au NPs into hot spots. In this regard, the two hybrid systems were tested as a SERS substrate by measuring the PSSH molecules that coated the Au NPs in the 2D and 3D arrays. The results show good uniformity and reproducibility. The use of a host matrix for the self-assembly of Au NPs results in a promising way of translating this hybrid system to technological applications while preserving the self-assembled properties of Au NPs. Thus, the self-assembly approach using porous silicon membranes as a host material has considerable potential to form the basis for a wide range of functional hybrid materials.

For future work, it could be motivating to study the effect of more particle concentrations, broader particle sizes, and shapes, or the use of different solvents. Additionally, the use of different pore diameters, pore thicknesses, or porous silicon matrixes could lead to achieving new self-assembly configurations or more pore filling. Also, due to the high uniformity of the Au NPs in the second hybrid configuration (3D array), it could be interesting to measure the optical properties, since the particles are tightly confined, they could lead to the generation of plasmon-polaritons modes.









Finally, the third chapter of the thesis involved the self-assembly of 3D binary tessellating superstructures with the same shapes but different radii, as well as different shapes. For the building blocks, spherical AuNPs and tetrahedral and octahedral NPs were chosen. SEM and TEM methods were used for the characterization of these binary systems. Based on the experimental results, an important discovery was the influence of the particle concentration and the polymer ligand length of polyhedral NPs in achieving the desired binary superstructure. The self-assembly method used here, the air-liquid subphase, allows the easy transfer and manipulation of these binary systems. The obtained large-scale 3D binary superstructures in combination with uniformity and homogeneity as well as a high degree of periodic order and densely packed

structures could be used for studying light-matter coupling. Thus, it could lead to applications in optical metamaterials and surface-enhanced spectroscopies. These results can also be extended to more complex binary systems depending on the desired applications.

In the future, it could be interesting to use the same approach used for the formation of the 3D binary TOH honeycomb superstructures but in order to generate more tessellated structures or new 3D binary combinations with more polyhedral shapes. For example, introducing additional parameters such as temperature, controlled vacuum, or added pressure may lead to an increase in packing density or different crystal structure, thereby enhancing the light-matter coupling. Finally, the use of SAXS and WAXS as well as liquid cell TEM, could help to understand the dynamics that govern the self-assembly of these binary superstructures

In summary, it is clear, that the self-assembly of Au NPs into highly ordered superstructures is still an enormous research field with many challenges to overcome in order to develop new materials with intriguing properties. Controlling the self-assembly of these diverse structures could lead to new materials with unique optical properties as well as applications in diverse fields such as catalysis, photonics, and the generation of new metamaterials.

List of Hazardous Substances

Table A2 List of chemical and GHS classifications			
Substance	Signal word	GHS-symbols	Hazard statements
Ascorbic acid	---	----	-----
Chloroauric acid	Danger		302, 314, 317, 373, 411
Cetyltrimethylammonium bromide	Danger		302, 315, 318, 335, 373, 410
Cetyltrimethylammonium chloride	Danger		302, 311, 314, 410
Diethylene glycol	Danger		302, 373
Ethanol	Danger		
Polystyrene	---	----	-----
Sodium borohydride	Danger		260, 301, 314
Tetrahydrofuran	Danger		225, 361d, 304, 373, 315, 336
Toluene	Danger		225, 361d, 304, 373, 315, 336

References

1. Pradhan, N. *et al.* Facets of nanotechnology as seen in food processing, packaging, and preservation industry. *BioMed Research International* vol. (2015).
2. Bayda, S., Adeel, M., Tuccinardi, T., Cordani, M. & Rizzolio, F. The history of nanoscience and nanotechnology: From chemical-physical applications to nanomedicine. *Molecules* vol. 25(2020).
3. Biswas, A. *et al.* Advances in top-down and bottom-up surface nanofabrication: Techniques, applications & future prospects. *Advances in Colloid and Interface Science* vol. 170 2–27 (2012).
4. Chai, Z., Childress, A. & Busnaina, A. A. Directed Assembly of Nanomaterials for Making Nanoscale Devices and Structures: Mechanisms and Applications. *ACS Nano* vol. 16 17641–17686 (2022).
5. Tahir, U., Shim, Y. B., Kamran, M. A., Kim, D.-I. & Jeong, M. Y. Nanofabrication Techniques: Challenges and Future Prospects. *J Nanosci Nanotechnol* **21**, 4981–5013 (2021).
6. Londe, G., Han, A. & Cho, H. J. *MEMS for Nanotechnology: Top-down Perspective*. Functional Nanostructures. vol. 107-167 (2018)
7. Fabrizio, E. Di *et al.* *Top-down and Bottom-up Nanofabrication for Multipurpose Applications*. MRS Online Proceedings Library. vol. 921 (2006).
8. Iqbal, P., Preece, J. A. & Mendes, P. M. Nanotechnology: The “Top-Down” and “Bottom-Up” Approaches. in *Supramolecular Chemistry*, Wiley. (2012).
9. Nagarajan, R. *Nanoparticles: Building Blocks for Nanotechnology*. <https://pubs.acs.org/sharingguidelines>.
10. Baig, N., Kammakakam, I., Falath, W. & Kammakakam, I. Nanomaterials: A review of synthesis methods, properties, recent progress, and challenges. *Materials Advances* vol. 2 1821–1871 (2021).
11. Alex, S. & Tiwari, A. Functionalized gold nanoparticles: Synthesis, properties and applications-A review. *J Nanosci Nanotechnol* **15**, 1869–1894 (2015).
12. Huang, X. & El-Sayed, M. A. Gold nanoparticles: Optical properties and implementations in cancer diagnosis and photothermal therapy. *Journal of Advanced Research* vol. 1 13–28 (2010).
13. Fan, J., Cheng, Y. & Sun, M. Functionalized Gold Nanoparticles: Synthesis, Properties and Biomedical Applications. *Chemical Record* vol. 20 1474–1504 (2020).
14. Sarfraz, N. & Khan, I. Plasmonic Gold Nanoparticles (AuNPs): Properties, Synthesis and their Advanced Energy, Environmental and Biomedical Applications. *Chemistry - An Asian Journal* vol. 16 720–742 (2021).
15. Hassan, H. *et al.* Gold nanomaterials – The golden approach from synthesis to applications. *Materials Science for Energy Technologies* vol. 5 375–390 (2022).

-
16. Sharifi, M. *et al.* Plasmonic gold nanoparticles: Optical manipulation, imaging, drug delivery and therapy. *Journal of Controlled Release* vols 311–312 170–189 (2019).
 17. Scarabelli, L., Coronado-Puchau, M., Giner-Casares, J. J., Langer, J. & Liz-Marzán, L. M. Monodisperse gold nanotriangles: Size control, large-scale self-assembly, and performance in surface-enhanced raman scattering. *ACS Nano* **8**, 5833–5842 (2014).
 18. Jain, P. K., Lee, K. S., El-Sayed, I. & El-Sayed, M. Calculated Absorption and Scattering Properties of Gold Nanoparticles of Different Size, Shape, and Composition: Applications in Biological Imaging and Biomedicine. *J Phys Chem B* **110**, 7238–7248 (2006).
 19. Petryayeva, E. & Krull, U. J. Localized surface plasmon resonance: Nanostructures, bioassays and biosensing-A review. *Analytica Chimica Acta* vol. 706 8–24 (2011).
 20. Herizchi, R., Abbasi, E., Milani, M. & Akbarzadeh, A. Current methods for synthesis of gold nanoparticles. *Artif Cells Nanomed Biotechnol* **44**, 596–602 (2016).
 21. Hammami, I., Alabdallah, N. M., jomaa, A. Al & kamoun, M. Gold nanoparticles: Synthesis properties and applications. *Journal of King Saud University - Science* vol. 33 (2021).
 22. Haiss, W., Thanh, N. T. K., Aveyard, J. & Fernig, D. G. Determination of size and concentration of gold nanoparticles from UV-Vis spectra. *Anal Chem* **79**, 4215–4221 (2007).
 23. López-Muñoz, G. A., Pescador-Rojas, J. A., Ortega-Lopez, J., Salazar, J. S. & Abraham Balderas-López, J. Thermal diffusivity measurement of spherical gold nanofluids of different sizes/concentrations. *Nanoscale Res Lett* **7**, (2012).
 24. Zhao, J. *et al.* Methods for describing the electromagnetic properties of silver and gold nanoparticles. *Acc Chem Res* **41**, 1710–1720 (2008).
 25. Lu, X., Rycenga, M., Skrabalak, S. E., Wiley, B. & Xia, Y. Chemical synthesis of novel plasmonic nanoparticles. *Annual Review of Physical Chemistry* vol. 60 167–192 (2009).
 26. Campbell, D. J., Xia, Y. & Belbruno, J. J. *Plasmons: Why Should We Care? In the Classroom* www.JCE.DivCHED.org • vol. 84 www.JCE.DivCHED.org (2007).
 27. Chen, Y. & Ming, H. Review of surface plasmon resonance and localized surface plasmon resonance sensor? *Photonic Sensors* vol. 2 37–49 (2012).
 28. Willets, K. A. & Van Duyne, R. P. Localized surface plasmon resonance spectroscopy and sensing. *Annu Rev Phys Chem* **58**, 267–297 (2007).
 29. Yu, R., Liz-Marzán, L. M. & García De Abajo, F. J. Universal analytical modeling of plasmonic nanoparticles. *Chemical Society Reviews* vol. 46 6710–6724 (2017).
 30. Zeng, S. *et al.* Size dependence of Au NP-enhanced surface plasmon resonance based on differential phase measurement. *Sens Actuators B Chem* **176**, 1128–1133 (2013).
 31. Jain, P. K. & El-Sayed, M. A. Plasmonic coupling in noble metal nanostructures. *Chem Phys Lett* **487**, 153–164 (2010).

-
32. Tan, S. J., Campolongo, M. J., Luo, D. & Cheng, W. Building plasmonic nanostructures with DNA. *Nature Nanotechnology* vol. 6 268–276 (2011).
 33. Kelly, K. L., Coronado, E., Zhao, L. L. & Schatz, G. C. The optical properties of metal nanoparticles: The influence of size, shape, and dielectric environment. *Journal of Physical Chemistry B* **107**, 668–677 (2003).
 34. Dasri, T. & Chingsungnoen, A. Surface plasmon resonance enhanced light absorption and wavelength tuneable in gold-coated iron oxide spherical nanoparticle. *J Magn Magn Mater* **456**, 368–371 (2018).
 35. Chen, J. *et al.* Dielectric waveguide-enhanced localized surface plasmon resonance refractive index sensing. *Opt Mater Express* **8**, 342 (2018).
 36. Reguera, J., Langer, J., Jiménez De Aberasturi, D. & Liz-Marzán, L. M. Anisotropic metal nanoparticles for surface enhanced Raman scattering. *Chemical Society Reviews* vol. 46 3866–3885 (2017).
 37. Schulz, F., Vossmeier, T., Bastús, N. G. & Weller, H. Effect of the spacer structure on the stability of gold nanoparticles functionalized with monodentate thiolated poly(ethylene glycol) ligands. *Langmuir* **29**, 9897–9908 (2013).
 38. Zhao, P., Li, N. & Astruc, D. State of the art in gold nanoparticle synthesis. *Coordination Chemistry Reviews* vol. 257 638–665 (2013).
 39. Xia, Y., Gilroy, K. D., Peng, H. & Xia, X. Keimvermitteltes Wachstum kolloidaler Metallnanokristalle. *Angewandte Chemie* **129**, 60–98 (2017).
 40. Zheng, Y., Zhong, X., Li, Z. & Xia, Y. Successive, seed-mediated growth for the synthesis of single-crystal gold nanospheres with uniform diameters controlled in the range of 5–150 nm. *Particle and Particle Systems Characterization* **31**, 266–273 (2014).
 41. Xia, Y., Gilroy, K. D., Peng, H. & Xia, X. Keimvermitteltes Wachstum kolloidaler Metallnanokristalle. *Angewandte Chemie* **129**, 60–98 (2017).
 42. Scarabelli, L., Sánchez-Iglesias, A., Pérez-Juste, J. & Liz-Marzán, L. M. A ‘Tips and Tricks’ Practical Guide to the Synthesis of Gold Nanorods. *Journal of Physical Chemistry Letters* **6**, 4270–4279 (2015).
 43. Senthil Kumar, P., Pastoriza-Santos, I., Rodríguez-González, B., Javier García De Abajo, F. & Liz-Marzán, L. M. High-yield synthesis and optical response of gold nanostars. *Nanotechnology* **19**, (2008).
 44. Zheng, Y. *et al.* Seed-mediated synthesis of gold tetrahedra in high purity and with tunable, well-controlled sizes. *Chem Asian J* **9**, 2635–2640 (2014).
 45. García-Lojo, D. *et al.* Integrating Plasmonic Supercrystals in Microfluidics for Ultrasensitive, Label-Free, and Selective Surface-Enhanced Raman Spectroscopy Detection. *ACS Appl Mater Interfaces* **12**, 46557–46564 (2020).

-
46. Lu, X., Rycenga, M., Skrabalak, S. E., Wiley, B. & Xia, Y. Chemical synthesis of novel plasmonic nanoparticles. *Annual Review of Physical Chemistry* vol. 60 167–192 (2009).
 47. Mehere, A. & Chaure, N. B. Precisely controlled shape and size of gold nanostructures by seed-mediated reduction reaction method. *Appl Phys A Mater Sci Process* **126**, (2020).
 48. Niidome, Y., Haine, A. T. & Niidome, T. Anisotropic gold-based nanoparticles: Preparation, properties, and applications. *Chemistry Letters* vol. 45 488–498 (2016).
 49. Mahato, K. *et al.* Gold nanoparticle surface engineering strategies and their applications in biomedicine and diagnostics. *3 Biotech* vol. 9 (2019).
 50. Ahmad, F. *et al.* Unique Properties of Surface-Functionalized Nanoparticles for Bio-Application: Functionalization Mechanisms and Importance in Application. *Nanomaterials* vol. 12 (2022).
 51. Young, K. L. *et al.* Using DNA to design plasmonic metamaterials with tunable optical properties. *Advanced Materials* **26**, 653–659 (2014).
 52. Whitesides, G. M. & Grzybowski, B. Self-assembly at all scales. *Science* vol. 295 2418–2421 (2002).
 53. *Nanoparticles Building Blocks for Nanotechnology*. (Springer US, Boston, MA, 2004). doi:10.1007/978-1-4419-9042-6.
 54. Wang, C., Siu, C., Zhang, J. & Fang, J. Understanding the forces acting in self-assembly and the implications for constructing three-dimensional (3D) supercrystals. *Nano Res* **8**, 2445–2466 (2015).
 55. Park, J. *et al.* Ultra-large-scale syntheses of monodisperse nanocrystals. *Nat Mater* **3**, 891–895 (2004).
 56. Grzelczak, M., Pérez-Juste, J., Mulvaney, P. & Liz-Marzán, L. M. Shape control in gold nanoparticle synthesis. *Chem Soc Rev* **37**, 1783–1791 (2008).
 57. Zhuang, T. T. *et al.* Regioselective magnetization in semiconducting nanorods. *Nature Nanotechnology* vol. 15 192–197 (2020).
 58. Dey, S. *et al.* DNA origami. *Nature Reviews Methods Primers* vol. 1 (2021).
 59. Gong, J., Li, G. & Tang, Z. Self-assembly of noble metal nanocrystals: Fabrication, optical property, and application. *Nano Today* vol. 7 564–585 (2012).
 60. Ming, T. *et al.* Ordered gold nanostructure assemblies formed by droplet evaporation. *Angewandte Chemie - International Edition* **47**, 9685–9690 (2008).
 61. Apte, A. *et al.* Self-assembled vertically aligned gold nanorod superlattices for ultra-high sensitive detection of molecules. *Nano Res* **8**, 907–919 (2015).
 62. Talapin, D. V. *et al.* Quasicrystalline order in self-assembled binary nanoparticle superlattices. *Nature* **461**, 964–967 (2009).

-
63. Redl, F. X., Cho, K. S., Murray, C. B. & O'Brien, S. Three-dimensional binary superlattices of magnetic nanocrystals and semiconductor quantum dots. *Nature* **423**, 968–971 (2003).
 64. Shevchenko, E. V., Talapin, D. V., O'Brien, S. & Murray, C. B. Polymorphism in AB₁₃ nanoparticle superlattices: An example of semiconductor-metal metamaterials. *J Am Chem Soc* **127**, 8741–8747 (2005).
 65. Dong, A., Chen, J., Vora, P. M., Kikkawa, J. M. & Murray, C. B. Binary nanocrystal superlattice membranes self-assembled at the liquid-air interface. *Nature* **466**, 474–477 (2010).
 66. Dong, A. *et al.* Multiscale periodic assembly of striped nanocrystal superlattice films on a liquid surface. *Nano Lett* **11**, 841–846 (2011).
 67. Dong, A., Ye, X., Chen, J. & Murray, C. B. Two-dimensional binary and ternary nanocrystal superlattices: The case of monolayers and bilayers. *Nano Lett* **11**, 1804–1809 (2011).
 68. Paik, T., Ko, D. K., Gordon, T. R., Doan-Nguyen, V. & Murray, C. B. Studies of liquid crystalline self-assembly of GdF₃ nanoplates by in-plane, out-of-plane SAXS. *ACS Nano* **5**, 8322–8330 (2011).
 69. Kang, Y. *et al.* Engineering catalytic contacts and thermal stability: Gold/iron oxide binary nanocrystal superlattices for CO oxidation. *J Am Chem Soc* **135**, 1499–1505 (2013).
 70. Paik, T. & Murray, C. B. Shape-directed binary assembly of anisotropic nanoplates: A nanocrystal puzzle with shape-complementary building blocks. *Nano Lett* **13**, 2952–2956 (2013).
 71. Halley, J. D. & Winkler, D. A. Consistent concepts of self-organization and self-assembly. *Complexity* vol. 14 10–17 Preprint at <https://doi.org/10.1002/cplx.20235> (2008).
 72. Van Anders, G., Klotsa, D., Ahmed, N. K., Engel, M. & Glotzer, S. C. Understanding shape entropy through local dense packing. *Proc Natl Acad Sci U S A* **111**, E4812–E4821 (2014).
 73. Damasceno, P. F., Engel, M. & Glotzer, S. C. Predictive self-assembly of polyhedra into complex structures. *Science (1979)* **337**, 453–457 (2012).
 74. Si, K. J., Chen, Y., Shi, Q. & Cheng, W. Nanoparticle Superlattices: The Roles of Soft Ligands. *Advanced Science* vol. 5 (2018).
 75. Grzybowski, B. A. Charged nanoparticles crystallizing and controlling crystallization: From coatings to nanoparticle surfactants to chemical amplifiers. *CrystEngComm* vol. 16 9368–9380 (2014).
 76. Qin, X., Wang, T. & Jiang, L. *Surface Engineering of Nanoparticles for Triggering Collective Properties of Supercrystals*. <https://academic.oup.com/nsr/article/4/5/672/4762248> (2017).
 77. Sánchez-Iglesias, A. *et al.* Hydrophobic interactions modulate self-assembly of nanoparticles. *ACS Nano* **6**, 11059–11065 (2012).
 78. Gandra, N., Abbas, A., Tian, L. & Singamaneni, S. Plasmonic planet-satellite analogues: Hierarchical self-assembly of gold nanostructures. *Nano Lett* **12**, 2645–2651 (2012).

-
79. Xu, Z., Wang, L., Fang, F., Fu, Y. & Yin, Z. A Review on Colloidal Self-Assembly and their Applications. *Curr Nanosci* **12**, 725–746 (2016).
 80. Courty, A., Richardi, J., Albouy, P. A. & Pileni, M. P. How to control the crystalline structure of supracrystals of 5-nm silver nanocrystals. *Chemistry of Materials* **23**, 4186–4192 (2011).
 81. Goubet, N., Richardi, J., Albouy, P. A. & Pileni, M. P. How to predict the growth mechanism of supracrystals from gold nanocrystals. *Journal of Physical Chemistry Letters* **2**, 417–422 (2011).
 82. Wang, Z., Ai, B., Möhwald, H. & Zhang, G. Colloidal Lithography Meets Plasmonic Nanochemistry. *Advanced Optical Materials* vol. 6 (2018).
 83. Coropceanu, I. *et al.* Self-assembly of nanocrystals into strongly electronically coupled all-inorganic supercrystals. *Science (1979)* **375**, 1422–1426 (2022).
 84. Hanske, C. *et al.* Solvent-Assisted Self-Assembly of Gold Nanorods into Hierarchically Organized Plasmonic Mesostuctures. *ACS Appl Mater Interfaces* **11**, 11763–11771 (2019).
 85. Wendy Gu, X. *et al.* Tolerance to structural disorder and tunable mechanical behavior in self-Assembled superlattices of polymer-grafted nanocrystals. *Proc Natl Acad Sci U S A* **114**, 2836–2841 (2017).
 86. Tam, E. *et al.* Mechanical properties of face-centered cubic supercrystals of nanocrystals. *Nano Lett* **10**, 2363–2367 (2010).
 87. Gu, X. W. Mechanical Properties of Architected Nanomaterials Made from Organic–Inorganic Nanocrystals. *JOM* vol. 70 2205–2217 (2018).
 88. Ng, K. C. *et al.* Free-standing plasmonic-nanorod superlattice sheets. *ACS Nano* **6**, 925–934 (2012).
 89. Lee, Y. H. *et al.* Nanoscale surface chemistry directs the tunable assembly of silver octahedra into three two-dimensional plasmonic superlattices. *Nat Commun* **6**, (2015).
 90. Tao, A., Sinsersuksakul, P. & Yang, P. Tunable plasmonic lattices of silver nanocrystals. *Nat Nanotechnol* **2**, 435–440 (2007).
 91. Sun, L., Lin, H., Kohlstedt, K. L., Schatz, G. C. & Mirkin, C. A. Design principles for photonic crystals based on plasmonic nanoparticle superlattices. *Proc Natl Acad Sci U S A* **115**, 7242–7247 (2018).
 92. Yazdani, N. *et al.* Nanocrystal superlattices as phonon-engineered solids and acoustic metamaterials. *Nat Commun* **10**, (2019).
 93. Deori, K., Gupta, D., Saha, B. & Deka, S. Design of 3-dimensionally self-assembled CeO₂ nanocube as a breakthrough catalyst for efficient alkylarene oxidation in water. *ACS Catal* **4**, 3169–3179 (2014).
 94. Herran, M. *et al.* Plasmonic bimetallic two-dimensional supercrystals for H₂ generation. *Nat Catal* **6**, 1205–1214 (2023).

-
95. Borah, R., Karthick Raj, A. G., Minja, A. C. & Verbruggen, S. W. A Review on Self-Assembly of Colloidal Nanoparticles into Clusters, Patterns, and Films: Emerging Synthesis Techniques and Applications. *Small Methods* vol. 7 (2023).
 96. Chen, P. Z., Pollit, L., Jones, L. & Gu, F. X. Functional Two- and Three-Dimensional Architectures of Immobilized Metal Nanoparticles. *Chem* vol. 4 2301–2328 (2018).
 97. Nie, Z., Petukhova, A. & Kumacheva, E. Properties and emerging applications of self-assembled structures made from inorganic nanoparticles. *Nature Nanotechnology* vol. 5 15–25 (2010).
 98. García-Lojo, D. *et al.* Plasmonic Supercrystals. *Acc Chem Res* **52**, 1855–1864 (2019).
 99. Yang, G., Hu, L., Keiper, T. D., Xiong, P. & Hallinan, D. T. Gold Nanoparticle Monolayers with Tunable Optical and Electrical Properties. *Langmuir* **32**, 4022–4033 (2016).
 100. Wang, H. *et al.* Gold nanoparticle superlattice monolayer with tunable interparticle gap for surface-enhanced Raman spectroscopy. *Nanoscale* **11**, 13917–13923 (2019).
 101. Green, A. M. *et al.* Structural Order and Plasmonic Response of Nanoparticle Monolayers. *ACS Photonics* **11**, 1280–1292 (2024).
 102. Macfarlane, R. J., O'Brien, M. N., Petrosko, S. H. & Mirkin, C. A. Nucleic acid-modified nanostructures as programmable atom equivalents: forging a new 'table of elements'. *Angewandte Chemie - International Edition* vol. 52 5688–5698 (2013).
 103. Schulz, F. *et al.* Structural order in plasmonic superlattices. *Nat Commun* **11**, (2020).
 104. Bian, K. *et al.* Formation of self-assembled gold nanoparticle supercrystals with facet-dependent surface plasmonic coupling. *Nat Commun* **9**, (2018).
 105. Kim, H. J. *et al.* Effect of Polymer Chain Length on the Superlattice Assembly of Functionalized Gold Nanoparticles. *Langmuir* **37**, 10143–10149 (2021).
 106. Schulz, F. & Lange, H. Optimizing Interparticle Gaps in Large-Scale Gold Nanoparticle Supercrystals for Flexible Light-Matter Coupling. *Adv Opt Mater* **10**, (2022).
 107. Mueller, N. S. *et al.* Deep strong light–matter coupling in plasmonic nanoparticle crystals. *Nature* **583**, 780–784 (2020).
 108. Mueller, N. S. *et al.* Surface-Enhanced Raman Scattering and Surface-Enhanced Infrared Absorption by Plasmon Polaritons in Three-Dimensional Nanoparticle Supercrystals. *ACS Nano* **15**, 5523–5533 (2021).
 109. Xia, J., Horst, N., Guo, H. & Travesset, A. Superlattices of Nanocrystals with Polystyrene Ligands: From the Colloidal to Polymer Limit. *Macromolecules* **52**, 8056–8066 (2019).
 110. Van Der Stam, W. *et al.* Self-assembly of colloidal hexagonal bipyramid- and bipyramid-shaped ZnS nanocrystals into two-dimensional superstructures. *Nano Lett* **14**, 1032–1037 (2014).
 111. Ye, X. *et al.* Structural diversity in binary superlattices self-assembled from polymer-grafted nanocrystals. *Nat Commun* **6**, (2015).

-
112. Mueller, N. S. *et al.* Dark Interlayer Plasmons in Colloidal Gold Nanoparticle Bi- and Few-Layers. *ACS Photonics* **5**, 3962–3969 (2018).
 113. Bishop, K. J. M., Wilmer, C. E., Soh, S. & Grzybowski, B. A. Nanoscale forces and their uses in self-assembly. *Small* vol. 5 1600–1630 (2009).
 114. Law, J., Chen, H., Wang, Y., Yu, J. & Sun, Y. *Gravity-Resisting Colloidal Collectives*. <https://www.science.org> (2022).
 115. Mishra, D. *et al.* Growth modes of nanoparticle superlattice thin films. *Nanotechnology* **25**, (2014).
 116. Schulz, F. *et al.* Plasmonic Supercrystals with a Layered Structure Studied by a Combined TEM-SAXS-XCCA Approach. *Adv Mater Interfaces* **7**, (2020).
 117. Zhong, Y., Allen, V. R., Chen, J., Wang, Y. & Ye, X. Multistep Crystallization of Dynamic Nanoparticle Superlattices in Nonaqueous Solutions. *J Am Chem Soc* **144**, 14915–14922 (2022).
 118. Lee, J. *et al.* Mechanistic Understanding of the Growth Kinetics and Dynamics of Nanoparticle Superlattices by Coupling Interparticle Forces from Real-Time Measurements. *ACS Nano* **12**, 12778–12787 (2018).
 119. Schulz, F., Lokteva, I., Parak, W. J. & Lehmkuhler, F. Recent Notable Approaches to Study Self-Assembly of Nanoparticles with X-Ray Scattering and Electron Microscopy. *Particle and Particle Systems Characterization* vol. 38 (2021).
 120. Bian, K. *et al.* Shape-anisotropy driven symmetry transformations in nanocrystal superlattice polymorphs. *ACS Nano* **5**, 2815–2823 (2011).
 121. Bian, K., Li, R. & Fan, H. Controlled Self-Assembly and Tuning of Large PbS Nanoparticle Supercrystals. *Chemistry of Materials* **30**, 6788–6793 (2018).
 122. Yee, D. W., Lee, M. S., An, J. & Macfarlane, R. J. Reversible Diffusionless Phase Transitions in 3D Nanoparticle Superlattices. *J Am Chem Soc* **145**, 6051–6056 (2023).
 123. Canham, L. T. Silicon quantum wire array fabrication by electrochemical and chemical dissolution of wafers. *Appl Phys Lett* **57**, 1046–1048 (1990).
 124. Lehmann, Volker. *The Electrochemistry of Silicon : Instrumentation, Science, Materials and Applications*. (Wiley-VCH, 2002).
 125. Zhang, X. G. Morphology and Formation Mechanisms of Porous Silicon. *J Electrochem Soc* **151**, C69 (2004).
 126. Harraz, F. A., Sakka, T. & Ogata, Y. H. A comparative electrochemical study of iron deposition onto n- and p-type porous silicon prepared from lightly doped substrates. *Electrochim Acta* **50**, 5340–5348 (2005).
 127. Hernández-Montelongo, J. *et al.* Nanostructured porous silicon: The winding road from photonics to cell scaffolds - A review. *Frontiers in Bioengineering and Biotechnology* vol. 3 (2015).

-
128. Zhang, X. G. Mechanism of Pore Formation on n-Type Silicon. *J Electrochem Soc* **138**, 3750–3756 (1991).
 129. Koker, L. & Kolasinski, K. W. Photoelectrochemical etching of Si and porous Si in aqueous HF. *Physical Chemistry Chemical Physics* **2**, 277–281 (2000).
 130. Volovlikova, O., Gavrilov, S. & Lazarenko, P. Influence of illumination on porous silicon formed by photo-assisted etching of p-Type si with a different doping level. *Micromachines (Basel)* **11**, (2020).
 131. Radzali, R. *et al.* *Properties of Porous Silicon by Two-Step Alternating Current Photo-Assisted Electrochemical Etching (ACPEC) Technique under Different Applied Current Density for MSM Photodetector Device Application*. vol. 14.
 132. Gelloz, B., Fuwa, H., Kondoh, E. & Jin, L. (Invited) Photo-Assisted Etching of Porous Silicon Nanostructures in Hydrofluoric Acid Using Monochromatic Light . *ECS Trans* **86**, 71–81 (2018).
 133. Radzali, R. *et al.* The effect of etching duration on structural properties of porous Si fabricated by a new two-steps alternating current photo-assisted electrochemical etching (ACPEC) technique for MSM photodetector. in *AIP Conference Proceedings* vol. 1875 (American Institute of Physics Inc., 2017).
 134. Canham, L. Tunable properties of porous silicon. in *Handbook of Porous Silicon* 201–206 (Springer International Publishing, 2014). doi:10.1007/978-3-319-05744-6_19.
 135. Harraz, F. A., Sakka, T. & Ogata, Y. H. *Immersion Plating of Copper Using (CF 3 SO 3) 2 Cu onto Porous Silicon from Organic Solutions*. *Electrochimica Acta* vol. 46 www.elsevier.nl/locate/electacta (2001).
 136. Trifonov, T., Rodríguez, A., Marsal, L. F., Pallarès, J. & Alcubilla, R. Macroporous silicon: A versatile material for 3D structure fabrication. *Sens Actuators A Phys* **141**, 662–669 (2008).
 137. Gabouze, N. & Ozanam, F. Macroporous Silicon. in *Handbook of Porous Silicon* 1–11 (Springer International Publishing, 2014). doi:10.1007/978-3-319-04508-5_10-1.
 138. Hernández-Montelongo, J. *et al.* Nanostructured porous silicon: The winding road from photonics to cell scaffolds - A review. *Frontiers in Bioengineering and Biotechnology* vol. 3 Preprint at <https://doi.org/10.3389/fbioe.2015.00060> (2015).
 139. Kumeria, T., McInnes, S. J. P., Maher, S. & Santos, A. Porous silicon for drug delivery applications and theranostics: recent advances, critical review and perspectives. *Expert Opinion on Drug Delivery* vol. 14 1407–1422 Preprint at <https://doi.org/10.1080/17425247.2017.1317245> (2017).
 140. Levitsky, I. A. Porous silicon structures as optical gas sensors. *Sensors (Switzerland)* vol. 15 19968–19991 Preprint at <https://doi.org/10.3390/s150819968> (2015).
 141. Agafilushkina, S. N. *et al.* Raman signal enhancement tunable by gold-covered porous silicon films with different morphology. *Sensors (Switzerland)* **20**, 1–11 (2020).

-
142. Wali, L. A., Hasan, K. K. & Alwan, A. M. Rapid and Highly Efficient Detection of Ultra-low Concentration of Penicillin G by Gold Nanoparticles/Porous Silicon SERS Active Substrate. *Spectrochim Acta A Mol Biomol Spectrosc* **206**, 31–36 (2019).
 143. Abbas, H. K., Safari, E. & Alwan, A. M. Improved the performance of trimetallic plasmonics SERS sensors by controlling the metals ratio. *Journal of Materials Science: Materials in Electronics* **35**, (2024).
 144. Bandarenka, H. *et al.* Nanostructured metal films formed onto porous silicon template. *Journal of Nano Research* **39**, 235–255 (2016).
 145. De La Mora, M. B., Bornacelli, J., Nava, R., Zanella, R. & Reyes-Esqueda, J. A. Porous silicon photoluminescence modification by colloidal gold nanoparticles: Plasmonic, surface and porosity roles. *J Lumin* **146**, 247–255 (2014).
 146. Dheyab, A. B., Wali, L. A., Alwan, A. M. & Naseef, I. A. Perfect incorporation of AuNPs on the p-n-porous silicon for highly-efficient solar cells. *Optik (Stuttg)* **198**, (2019).
 147. Halas, N. J., Lal, S., Chang, W. S., Link, S. & Nordlander, P. Plasmons in strongly coupled metallic nanostructures. *Chemical Reviews* vol. 111 3913–3961 (2011).
 148. Langer, J. *et al.* Present and future of surface-enhanced Raman scattering. *ACS Nano* vol. 14 28–117 (2020).
 149. Han, X. X., Rodriguez, R. S., Haynes, C. L., Ozaki, Y. & Zhao, B. Surface-enhanced Raman spectroscopy. *Nature Reviews Methods Primers* vol. 1 (2021).
 150. Solís, D. M., Taboada, J. M., Obelleiro, F., Liz-Marzán, L. M. & García De Abajo, F. J. Optimization of Nanoparticle-Based SERS Substrates through Large-Scale Realistic Simulations. *ACS Photonics* **4**, 329–337 (2017).
 151. Wang, X., Huang, S. C., Hu, S., Yan, S. & Ren, B. Fundamental understanding and applications of plasmon-enhanced Raman spectroscopy. *Nature Reviews Physics* vol. 2 253–271 (2020).
 152. Song, C., Yang, B., Yang, Y. & Wang, L. SERS-based mercury ion detections: Principles, strategies and recent advances. *Science China Chemistry* vol. 59 16–29 (2016).
 153. Lin, E. C., Fang, J., Park, S. C., Johnson, F. W. & Jacobs, H. O. Effective localized collection and identification of airborne species through electrodynamic precipitation and SERS-based detection. *Nat Commun* **4**, (2013).
 154. Kim, W. *et al.* Paper-Based Surface-Enhanced Raman Spectroscopy for Diagnosing Prenatal Diseases in Women. *ACS Nano* **12**, 7100–7108 (2018).
 155. Cui, H., Li, S., Deng, S., Chen, H. & Wang, C. Flexible, Transparent, and Free-Standing Silicon Nanowire SERS Platform for in Situ Food Inspection. *ACS Sens* **2**, 386–393 (2017).
 156. Zeng, Y., Ren, J. Q., Shen, A. G. & Hu, J. M. Splicing Nanoparticles-Based ‘click’ SERS Could Aid Multiplex Liquid Biopsy and Accurate Cellular Imaging. *J Am Chem Soc* **140**, 10649–10652 (2018).

-
157. Lepasant, M. *et al.* Impregnation of high-magnetization FeCo nanoparticles in mesoporous silicon: An experimental approach. *Front Chem* **6**, (2018).
 158. Ye, X., Chen, J., Diroll, B. T. & Murray, C. B. Tunable plasmonic coupling in self-assembled binary nanocrystal superlattices studied by correlated optical microspectrophotometry and electron microscopy. *Nano Lett* **13**, 1291–1297 (2013).
 159. Cherniukh, I. *et al.* Perovskite-type superlattices from lead halide perovskite nanocubes. *Nature* **593**, 535–542 (2021).
 160. Yang, Y. *et al.* Scalable Assembly of Crystalline Binary Nanocrystal Superparticles and Their Enhanced Magnetic and Electrochemical Properties. *J Am Chem Soc* **140**, 15038–15047 (2018).
 161. Huang, Y., Wu, C., Chen, J. & Tang, J. Colloidal Self-Assembly: From Passive to Active Systems. *Angewandte Chemie - International Edition* vol. 63 Preprint at <https://doi.org/10.1002/anie.202313885> (2024).
 162. Shevchenko, E. V., Talapin, D. V., Kotov, N. A., O'Brien, S. & Murray, C. B. Structural diversity in binary nanoparticle superlattices. *Nature* **439**, 55–59 (2006).
 163. Boles, M. A. & Talapin, D. V. Many-Body Effects in Nanocrystal Superlattices: Departure from Sphere Packing Explains Stability of Binary Phases. *J Am Chem Soc* **137**, 4494–4502 (2015).
 164. Talapin, D. V. *et al.* Quasicrystalline order in self-assembled binary nanoparticle superlattices. *Nature* **461**, 964–967 (2009).
 165. Deng, K. *et al.* Binary Nanoparticle Superlattices for Plasmonically Modulating Upconversion Luminescence. *Small* **16**, (2020).
 166. O'Brien, M. N., Jones, M. R., Lee, B. & Mirkin, C. A. Anisotropic nanoparticle complementarity in DNA-mediated co-crystallization. *Nat Mater* **14**, 833–839 (2015).
 167. Pietrobon, B., McEachran, M. & Kitaev, V. Synthesis of size-controlled faceted pentagonal silver nanorods with tunable plasmonic properties and self-assembly of these nanorods. *ACS Nano* **3**, 21–26 (2009).
 168. Meng, L. *et al.* Coassembly of Complementary Polyhedral Metal-Organic Framework Particles into Binary Ordered Superstructures. *J Am Chem Soc* **146**, 21225–21230 (2024).
 169. Yue, X., Li, J., Yan, N. & Jiang, W. Entropically Driven Fabrication of Binary Superlattices Assembled from Polymer-Tethered Nanocubes and Nanospheres. *Small* **19**, (2023).
 170. Zhou, W. *et al.* *Space-Tiled Colloidal Crystals from DNA-Forced Shape-Complementary Polyhedra Pairing*. <https://www.science.org>.
 171. Wang, Y. *et al.* Structural Diversity in Dimension-Controlled Assemblies of Tetrahedral Gold Nanocrystals. *J Am Chem Soc* **144**, 13538–13546 (2022).
 172. Wang, Y. *et al.* Controlled Self-Assembly of Gold Nanotetrahedra into Quasicrystals and Complex Periodic Supracrystals. *J Am Chem Soc* **145**, 17902–17911 (2023).

-
173. Quan, Z. & Fang, J. Superlattices with non-spherical building blocks. *Nano Today* vol. 5 390–411 Preprint at <https://doi.org/10.1016/j.nantod.2010.08.011> (2010).
 174. Schneider, J., Nagaoka, Y., Fan, H. & Chen, O. Chemical and architectural intricacy from nanoscale tetrahedra and their analogues. *MRS Bull* **49**, 319–329 (2024).
 175. Zhou, W., Li, Y., Partridge, B. E. & Mirkin, C. A. Engineering Anisotropy into Organized Nanoscale Matter. *Chemical Reviews* (2024).
 176. Chandler, B. M. *et al.* Coherent Phonon Dynamics in Plasmonic Gold Tetrahedral Nanoparticle Ensembles. *J Phys Chem Lett* **15**, 9686–9691 (2024).
 177. Qiu, Y. *et al.* Symmetry-controllable assembly of Au nanooctahedron superlattice membranes for SERS. *Chemical Communications* **60**, 9218–9221 (2024).
 178. Lee, Y. H. *et al.* Nanoscale surface chemistry directs the tunable assembly of silver octahedra into three two-dimensional plasmonic superlattices. *Nat Commun* **6**, (2015).
 179. Brunner, J. *et al.* Self-Assembled Magnetite Mesocrystalline Films: Toward Structural Evolution from 2D to 3D Superlattices. *Adv Mater Interfaces* **4**, (2017).
 180. Huang, X. *et al.* Understanding Fe₃O₄ Nanocube Assembly with Reconstruction of a Consistent Superlattice Phase Diagram. *J Am Chem Soc* **141**, 3198–3206 (2019).
 181. Boles, M. A., Engel, M. & Talapin, D. V. Self-assembly of colloidal nanocrystals: From intricate structures to functional materials. *Chemical Reviews* vol. 116 11220–11289 (2016).
 182. Deng, K., Luo, Z., Tan, L. & Quan, Z. Self-assembly of anisotropic nanoparticles into functional superstructures. *Chemical Society Reviews* vol. 49 6002–6038 (2020).
 183. Cadotte, A. T., Dshemuchadse, J., Damasceno, P. F., Newman, R. S. & Glotzer, S. C. Self-assembly of a space-tessellating structure in the binary system of hard tetrahedra and octahedra. *Soft Matter* **12**, 7073–7078 (2016).
 184. Gómez-Graña, S. *et al.* Gold Nanooctahedra with Tunable Size and Microfluidic-Induced 3D Assembly for Highly Uniform SERS-Active Supercrystals. *Chemistry of Materials* **27**, 8310–8317 (2015).
 185. Scarabelli, L., Sánchez-Iglesias, A., Pérez-Juste, J. & Liz-Marzán, L. M. A ‘Tips and Tricks’ Practical Guide to the Synthesis of Gold Nanorods. *Journal of Physical Chemistry Letters* **6**, 4270–4279 (2015).
 186. Yu, Y., Bosoy, C. A., Smilgies, D. M. & Korgel, B. A. Self-assembly and thermal stability of binary superlattices of gold and silicon nanocrystals. *Journal of Physical Chemistry Letters* **4**, 3677–3682 (2013).
 187. Lu, C., Akey, A. J., Dahlman, C. J., Zhang, D. & Herman, I. P. Resolving the growth of 3D colloidal nanoparticle superlattices by real-time small-angle X-ray scattering. *J Am Chem Soc* **134**, 18732–18738 (2012).

Acknowledgments

I would like to acknowledge all the colleagues with whom I have had the opportunity to work during these amazing years. Thank you so much for sharing your scientific experience during this great scientific journey.

Especially, I would to express my gratitude to:

Prof. Dr. Wolfgang Parak for allowing me to be part of this amazing group. I remember those days in Mexico when I sent you that email requesting an opportunity to be part of your team and when I received the answer, it was an incredible day for me. Thank you so much for all the support during the PhD, for allowing me to participate in different projects, and for encouraging me always to support young students (internships, high school, undergraduate, master, and PhD students). Taken together, all have made a huge impact on my professional career and my personal life. 4 years later in Germany, I can say that this was one of the most important decisions I made.

I would also like to give my sincerest thanks to my co-supervisor, Florian Schulz. I do not have any words to describe how grateful I am to you. I started my PhD lab work under your guidance and after almost 4 years, you still support me in each experiment, teach me, and always share your knowledge with me. Thanks for trusting me with several projects since I was able to meet incredible people and have amazing ideas. Thanks a lot, because you share with me your passion for the self-assembly of nanoparticles, a new tiny but amazing world. Now, I would like to go deeper into this incredible field.

I would like to express my gratitude to Robert Frömter for his assistance, guidance, and support with electron scanning microscopy throughout my PhD journey. I am truly thankful to you for always being available to help me. Thank you for maintaining the microscope in excellent condition at all times. It has now become my favorite characterization technique.

I would like to express my gratitude to the National Council for Science and Technology (CONACYT) of Mexico for funding my PhD. I am truly committed to the Mexican people and I am dedicated to contributing towards building a better future for Mexico.

I would like to express my gratitude to all my colleagues in the Parak group for maintaining an excellent working environment. I have wonderful memories of the parties and meetings we had

over the last few years. I want to thank Saad, Ben, Miao, Marvin, Ferdinand, Xin, Yuxuan, Sarodi, María, Hessam, Jili, Chenxi, Nills, Jette, Zahra, Samira, and everyone else for everything. I also want to extend my thanks to my master's students Zahra and Samira, who not only helped me explore new avenues in my PhD but also entrusted me with their master's project.

I would like to express my gratitude to all the collaborators I had the privilege to work with during my PhD. I am thankful to Prof. Patrick Huber from the Technical University of Hamburg and Prof. Stephanie Reich from Berlin University for their valuable contributions and insightful discussions related to this thesis and other collaborative projects. I am also grateful to Gabriela García from Berlin for her exceptional support in conducting the optical characterization of my supercrystals. Special thanks to Dr. Xingchen Ye for allowing me to learn about the synthesis of anisotropic nanoparticles from his group at Indiana Bloomington University. I gained invaluable knowledge during this internship. I would also like to thank the MIN Graduate School and Parak Group for their support during this research internship.

In addition, I believe that the technicians, Marten, Gerwin, and Yang, play a crucial role in our research group. I am extremely grateful for their outstanding support throughout this journey. They have always been available to resolve any issues in the labs and have ensured a smooth workflow by managing chemical supplies and equipment. Thank you all so much.

I want to express my gratitude to my parents, Martha and Juan, and my siblings, Luis and Berenice, for their unwavering support and encouragement throughout my journey. Despite being thousands of miles away, you always sent me the positive energy I needed to reach this milestone in my professional career.

Finally, and most importantly, I would like to express my deepest gratitude to my wife for her help and support during this incredible journey. Thank you for always being by my side through every adventure, for constantly motivating me, and for being ever ready to embark on a new project. In simple words, I couldn't have made this journey without you.

Before I forget ...

VIVA MÉXICO!

Declaration on oath

I hereby declare and affirm that this doctoral dissertation is my own work and that I have not used any aids and sources other than those indicated.

If electronic resources based on generative artificial intelligence (gAI) were used in the course of writing this dissertation, I confirm that my own work was the main and value-adding contribution and that complete documentation of all resources used is available in accordance with good scientific practice. I am responsible for any erroneous or distorted content, incorrect references, violations of data protection and copyright law or plagiarism that may have been generated by the gAI.

15-11-2024

Date



Signature of the doctoral candidate

This page is intentionally left blank